Università degli Studi di Roma "La Sapienza"
Facoltà di Ingegneria
Dottorato in elettromagnetismo applicato e scienze elettrofisiche

Tesi di Dottorato

Beam-Wall interaction in the LHC liner

Candidato
Andrea Mostacci

Docente Guida:
Prof. L. Palumbo

Correlatore:
Dr. F. Ruggiero

Anni Accademici 1997/00

Contents

Introduction

Motivation and goals

The Large Hadron Collider (LHC) is a circular collider under construction at the European Organisation for the Nuclear Research (CERN), in the area close to Geneva. It will be installed in the 27 km long underground tunnel, that has been housing the Large Electron-Positron collider (LEP) until November 2000. In the LHC, two counter-rotating proton beams, each with a 7 TeV energy, will collide, in order to study the interactions of the constituents of the hadronic matter at the TeV level of energy.

To bend, focus and properly guide the proton beams, very large magnetic fields are required (about 8 Tesla in the main dipoles), that are only achievable by using superconducting technology. Stability requirements for the beam motion impose stringent constraints to the quality of the magnetic field of the LHC magnets: the field perturbations must be controlled with a precision of 10^{-5}–10^{-4} units with respect to the main field component.

The design of the magnets (especially of the main dipoles) is an extremely difficult challenge; the operational temperature is around 2 K and thus any possible source of power loss (resulting on heating of the dipole components) has to be carefully kept under control. Obviously the main power source in a particle accelerator is the beam itself, especially in the LHC which will be filled with approximately 3000 high intensity bunches (of about 10^{11} protons each).

Another big challenge in the LHC is the low vacuum pressure necessary to circulate the beam without particle losses. The high vacuum has to be reached at cryogenic temperatures and this carries a number of major technological problems in obtaining and measuring it (the usual vacuum measurement techniques don't work at such low temperatures).

The minimisation of the power losses inside the magnets and the high vacuum issues result in a non conventional design of the beam pipe. The aim of this thesis is to discuss the effect of such a design on the particle beam stability and energy losses, by carefully estimating the interaction between the beam and its surroundings.

Our results are meant to be useful at the present stage of the LHC design and thus an analytical approach (with numerical and experimental validations) has been pursued whenever possible.

In this section we briefly review the actual shape of the LHC beam pipe, identifying the three (new) possible mechanisms of beam-wall interaction which will be discussed in details in the following chapters.

LHC beam pipe and the beam screen

The LHC beam pipe will be located inside the magnet cold bore which has a diameter of 49 mm [1]; the cold bore is the outer (cylindrical) pipe shown in Fig. 0.1 and the beam is supposed to travel on the axis of the structure. Between the beam and the cold bore and along most of the 27 km, there is the so called "beam screen" or "liner" (the slotted inner pipe in Fig. 0.1). Its main purpose is to shield the cold bore from the (incoherent) synchrotron radiation which would heat it, preventing the correct operations of the magnets. The amount of power deposited (without the liner) is estimated around 3.6 kW for a single beam [2]. The beam screen is independently cooled to 5–20 K by small cooling tubes (which are the "capillars" of 3.7 mm diameter located on the flat part of the beam screen in Fig. 0.1) in which superfluid He is flowing. Obviously the beam screen reduces the physical aperture available to the beam and its thickness should be as small as possible.

At those temperatures the low vacuum pressure is not obtained by conventional vacuum pumps, but through the cryo-pumping effect: the residual molecules whenever they arrive on the cold bore, stick to it (because of its low temperature). This has the obvious implication that the residual gas is not removed but it is simply kept away from the beam path. This means that any temperature change of the cold bore (e.g. during a quench) will result in a pressure rise since the molecules are not absorbed anymore on the cold bore surface. This is a second reason why the synchrotron radiation should not fall directly on the cold bore: it would cause gas desorption (practically sputtering the molecules sticked on the bore).

Figure 0.1: LHC beam pipe.

The beam screen is made of stainless steel in order to resist to mechanical stresses. In fact any abrupt variation of the magnetic field (e.g. during a quench) will induce strong Focault currents which, combined with the high field, could drastically deform the pipe if it were made of a "softer" material. In order to reduce the resistive wall effects (extremely relevant in a stainless steel pipe) a 50 μm copper layer is foreseen (see Fig. 0.1). Nevertheless, the main limitation to the LHC bunch intensity comes from resistive wall effects and those have been already extensively studied [2], thus they will not be covered in the present thesis.

To allow an efficient cryo-pumping, the beam screen has to be perforated and the ratio between the slotted and the total beam screen surface is fixed by the vacuum requirements to 4.4 %. The "pumping slots" are drilled in the two flat sides of the beam screen (see Fig. 0.1). The slots interrupt the electrical continuity of the beam pipe and thus they may induce beam energy losses and instability; moreover they couple the inner region (where the beam is travelling) to the outer "coaxial" region (between the screen and the cold bore). The distribution of the holes has to be as uniform as possible to ensure a uniform vacuum quality. The slots are drilled on a 1 mm thick wall and they are typically 1.5 mm wide and 8 mm long.

The synchrotron radiation hitting the beam screen surface may induce other undesirable side effects. In particular, for photo-electric effect, it can extract electrons from the metal surface. These electrons, accelerated by the high intensity (proton) bunches, may be subject to avalanche multiplication, resulting in an "electron cloud" extremely dangerous for the beam screen heating and the beam stability. High energy electrons can themselves induce gas desorption on the beam screen and the observed electron cloud effects in existing machines are always accompanied by a vacuum pressure rise. To reduce the photo-electric emission one way is to force the light to fall normally to the metal surface (which drastically reduces the probability of electron extraction); this can be achieved by creating an artificial saw-tooth roughness in the "illuminated" region of the beam screen [3]. A beneficial side effect of such a roughness is also to reduce the surface reflectivity so that only the first impacts can efficiently generate photoelectrons, with little acceleration by the beam electric field.

To actually build the beam screen, the copper layer will be "colaminated" on stainless steel sheets. Then the holes are drilled and the corrugation is obtained by a proper roughness of the press used in the colamination process. Eventually this perforated rough sheet is folded and welded in one side to get the actual beam screen in Fig. 0.1. The welding can not be coated by copper (or higher conducting materials) and thus this may have consequences on the beam energy losses.

Outline of the thesis

The present thesis aims at studying the beam-wall interaction due to the pumping slots, the artificial rough surface and the welding strips trying to enlighten the relevant parameters in order to give reliable estimates of the consequences on the key parameters of the LHC design. The thesis is organised as follows.

Chapter 1 discusses the effect of the pumping holes, in particular studying the interaction between the beam and the synchronous field that can be excited in the coaxial region (assuming cylindrical cross section). The interference effects among equispaced holes and the effect of the ohmic losses in the coaxial region (stainless steel) are addressed. The main result is to estimate analytically the power lost by the beam (which is practically not affected by the foreseen partial randomisation of the hole spacing) and to identify the parameters mostly affecting the losses in the present LHC design (namely the hole width and the wall thickness).

Chapter 2 investigates the interaction between a point charge and a rectangular pipe with periodic (rectangular) corrugation. Surface synchronous waves can be excited and analytical expressions for relevant parameters (such as synchronism frequency and longitudinal electric field) are discussed, in a parameter range interesting for the LHC (corrugation much smaller than the wavelengths and the typical geometrical length). This problem is now extremely relevant also for linear machines (such as free electron lasers) where ultra-short bunches interact with the roughness due to surface treatments; our result allows easily (worst case) estimations also for the bunch energy spread, which is relevant for those machines.

Chapter 3 deals with the propagation of a beam in a metallic (circular) beam pipe whose conductivity varies azimuthally. The interesting problem is the distribution of the currents on the beam pipe in such a geometry. Actually if the current substantially avoided the badly conducting region, the losses due to the welding strips in the LHC beam screen might be negligible, while currents constant with the azimuth result in a substantial amount of power loss. Computing the fields excited by an ultrarelativistic particle, the currents behaviour with the azimuth can be found and our semianalitycal estimates are in agreement with numerical simulations and experimental bench measurements.

Chapter 1

Energy lost by a particle beam in a lossy coaxial liner with many holes

1.1 Introduction

Several papers have been devoted to the interaction between a particle beam and the pumping holes, usually described in terms of coupling impedance and loss factor. In particular we are interested in the structure sketched in Fig. 1: the holes couple the vacuum chamber (a circular wave-guide) to the external ante-chamber (a coaxial wave-guide).

The problem has been solved by means of the modified Bethe's diffraction theory for a single hole in [4] and for N holes in [5], if they are small with respect to the wavelength λ. Recently this theory has been further modified to estimate analytically the effects of a long narrow slot [6]. Some measurements were also performed on a LHC vacuum chamber prototype [7] (i.e. coaxial chamber with many holes) to estimate the power lost by the beam because of these holes and the results were explained with a simplified model. The original Bethe's diffraction theory [8] has been used to study the effect of a single hole [9] in the beam pipe as well as many holes [10], for a pipe wall of infinite thickness so that there is no coupling with any external structure. Other techniques often used are the field matching method [11] and a variational approach [12]. A local impedance boundary condition of the Leontovich type, can be used to describe perforated pipe walls; in [13], analytical estimates, based on reciprocity formulas, are obtained for the quantities relevant to beam dynamics (namely longitudinal and transverse coupling impedance) for heterogeneous beam pipes with complex geometry, including partially perforated walls.

In this chapter we review previous results in the case of many holes, but including also the effect of field attenuation in the coaxial region. This case has not yet been studied in the framework of the modified Bethe theory and it is interesting in the project of future machines such as LHC. A possible attenuation source is the ohmic loss in the walls of the coaxial, but some other could be foreseen as well (as for instance proper attenuators). We will focus mainly on the first case, but our theory can be easily extended to other ones.

The modified Bethe's theory states that each hole is equivalent to magnetic and electric dipoles whose moments are proportional through appropriate hole polarizabilities to the fields propagating both in the beam pipe and in the coaxial region.

We consider a single relativistic charge travelling along the z-axis and start by studying the problem in a frequency range below all possible cut-offs, i.e. including only the TEM field propagating in the coaxial. Its amplitude depends on the dipole moments (that are the source of that field); we can derive a linear inhomogeneous system whose unknowns are the dipole moments and whose forcing term is the field of the charge. Once the system has been solved, we can express the field in each point of the structure in terms of the dipole moments; in particular we can compute the z-component of the electric field on the axis and then the longitudinal coupling impedance [14, 15]. The loss factor follows easily: for example with a Gaussian bunch we can apply Eq. (1.39) in the case of N holes obtaining Eq. (1.40). The results are in good agreement with MAFIA simulations [4, 5].

A further extension in frequency is possible including more modes, both in the circular and in the coaxial waveguide, although this is not necessary for long bunches (as in hadron machines), since the frequencies excited are usually below all possible cut-offs.

This chapter is organised as follows: we first study the ideal structure of a pipe with thin wall ($b_1 = b_2 = b$), then we briefly discuss the effect of wall thickness, how it can be taken into account and we make some comparisons with existing estimates.

In Sec. 1.2 a formula for the coupling impedance valid for any spacing between the holes and for any attenuation source in the coaxial is derived. Since it has been demonstrated [5] that the loss factor is not considerably influenced by the randomisation of the position of the holes, we focus on equally spaced holes (one hole per cross section): the goal is to give and discuss simplified formulae useful for the following calculations. Sec. 1.3 applies those results to the loss factor: we arrive at an analytical formula both when there are no losses in the coaxial and when we treat the ohmic ones. Still in the ideal case of thin wall, we discuss in Sec. 1.4 the power lost per unit length in the coaxial region. We also recall how to account for many holes on a cross section. Sec. 1.5 specifies how to modify the previous results for holes in a thick wall. A comparison with [7] is done in Sec. 1.6, confirming our results. Throughout the chapter, all the examples are done using LHC nominal parameters; in Sec. 1.7 we summarise the results most relevant for the project.

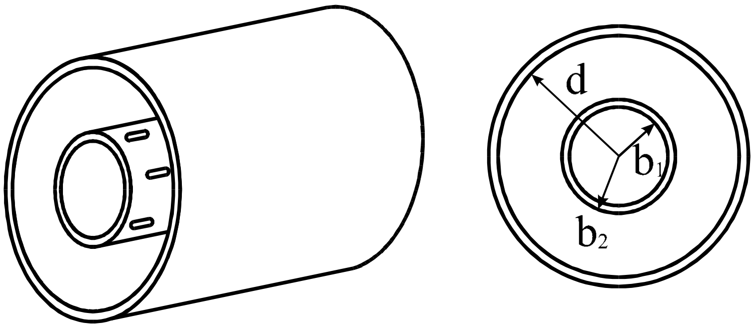

Figure 1.1: Relevant geometries.

1.1.1 Outline of the general theory

The general theory adopted in these calculations is described in [4, 5]; for convenience, we summarise its main features at frequencies below the beam pipe cut-off considering only scattered TEM-type fields, in the case of N holes.

We will use cylindrical coordinates, with z being the longitudinal coordinate, r and φ the radial and the azimuthal ones. The subscript "0" on a field means that it is a source field (charge field), while the fields with subscript "s" are the scattered ones propagating in coaxial region.

Bethe's diffraction theory [17] states that each hole is equivalent to an electric and a magnetic dipole whose moments are given by

$$\begin{aligned} M_\varphi(z_i) &= \alpha_m \left[H_{0\varphi}(z_i) - H_{s\varphi}(z_i) \right], \\ P_r(z_i) &= \varepsilon \alpha_e \left[E_{0r}(z_i) - E_{sr}(z_i) \right], \end{aligned} \qquad i = 1, \ldots, N \tag{1.1}$$

where α_m and α_e are the polarizabilities of the hole and $H_{s\varphi}$, E_{sr} is the scattered field calculated at the centre of the hole with longitudinal coordinate z_i. The primary field,

[1] This behaviour of α with the frequency is only valid for non-anomalous ohmic losses; we report it in this table only for reader's convenience.

Caption	Symbol	Numerical Value
wave number	$k_0 = \omega/c$	
attenuation constant[1]	$\alpha(\omega) = a\sqrt{\omega}$	
device length	L_d	14 m $\div$ 27 km
number of holes	N	870 $\div$ 1.7 10^6
number of holes per cross section	N_b	1$\div$8
bunch charge	Q	16 nC
bunch length	σ	7.5 cm
bunch cut-off	f_c	640 MHz
bunch spacing	S_b	7.5 m
coaxial walls resistivity (stainless steel)	ρ	7.1×10^{-7} Ωm
inner pipe radius	b_1	1.9 cm
outer pipe radius	$b_2 = b_1 + T$	2 cm
cold bore radius	d	2.45 cm
wall thickness	T	1 mm
hole spacing	D	1.6 cm
hole width	W	1.5 mm
hole length	L	8 mm
hole area	$A = \pi W^2/4 + W(L - W)$	11 mm^2
covered surface	f	4.4 %
radius of circular holes	$R = W/2$	0.75 mm

Table 1.1: List of symbols used throughout the chapter. Plots and examples refer to the LHC numerical values reported in the third column, unless otherwise specified.

generated by an ultra-relativistic point charge q, travelling along the axis of a perfectly conducting beam pipe of radius b, is ($k_0 = \omega/c$)

$$H_{0\varphi}(z_i) = \frac{q}{2\pi b}e^{-jk_0 z_i}, \;\; E_{0r}(z_i) = Z_0\frac{q}{2\pi b}e^{-jk_0 z_i}. \tag{1.2}$$

In [5], the TEM-type scattered fields are supposed to have the same phase velocity as the charge. We remove this hypothesis allowing for a complex propagation constant of the form

$$k_c = k_0 - j\alpha, \tag{1.3}$$

where α is the attenuation constant. Both k_0 and α are given functions of the frequency ω with dimensions of [m^{-1}]. If the attenuation constant is a real quantity, the field will be exponentially damped along the propagation direction (z-axis); the source of this attenuation fixes the ω-dependence of α. On the other hand, a purely imaginary α takes into account a slowing down of the TEM fields in the external coaxial region; that could be, for example, the effect of a long series of uniformly spaced holes acting as the periodic perturbation of boundary conditions in any slow-wave device.

In general the scattered fields can be expressed as a superposition of modes. The coefficients of the modal expansion are determined through the Lorentz reciprocity principle [17]; they are linear functions of the equivalent dipole moments of the apertures which can be obtained solving a $2N \times 2N$ linear system.

Once the equivalent dipole moments have been determined, we can calculate the longitudinal coupling impedance, using the result [5]

$$Z(\omega) = j\frac{\omega Z_0}{2\pi q b}\sum_{i=1}^{N}\left[\frac{M_\varphi(z_i)}{c} + P_r(z_i)\right]e^{jk_0 z_i}. \tag{1.4}$$

The longitudinal coupling impedance is the Green function of the problem; the loss factor depends on its real part, since [14]

$$k(\sigma) = \frac{1}{\pi}\int_0^\infty Z_{RE}\,(\omega)\,e^{-\left(\frac{\omega\,\sigma}{c}\right)^2}d\omega,$$

for a Gaussian bunch of length σ.

The previous quantities are important for the LHC beam dynamics. On the other hand, since the bunch will excite the TEM mode in the coaxial region, this will dissipate some power on the walls of the coaxial (stainless steel) causing heating of the cold bore. This is an essential parameter in the project of the machine; to estimate it, we introduce the dissipated power per unit length P, expressed in terms of the loss factor as

$$P = \frac{c\,Q^2\,k\,(\sigma)}{S_b\,L_d},$$

where Q is the bunch charge, S_b the bunch separation, L_d the device length and $k\,(\sigma)$ is the loss factor due to the N holes in the device.

1.2 Longitudinal coupling impedance

Each hole in the beam pipe is a source of electromagnetic field propagating in the coaxial region and can be characterised by equivalent dipole moments (electric and magnetic); Eq. (1.4) gives the longitudinal coupling impedance in terms of these moments. Here we derive analytical results for the coupling impedance when an attenuation source is present in the coaxial region; the numerical examples we give, are all done using LHC nominal parameters and the attenuation source is the ohmic loss on the walls of the coaxial region (see Fig. 1.1).

Having derived the coupling impedance for general spacing between the holes (Sec. 1.2.1), we then specify our treatment to uniformly spaced holes (Sec. 1.2.2). In the latter case, we give and comment a general formula focusing on the physical meaning of each term and showing the importance of the interference effects due to the TEM mode propagating in the coaxial structure; an approximate formula (valid in the nominal case of LHC) is also derived and discussed. In Sec. 1.2.3 we make remarks on the effect of the TEM field propagating in the same direction of the bunch, comparing with the complete case (i.e. including also the field propagating in the opposite direction).

1.2.1 General derivation

From dipole moments ...

The dipole moments obey a linear system whose forcing term depends on the field of the bunch over each hole. After having derived formally this system, we obtain a first order solution: we first give an analytical expression for M_φ and P_r, then we check their agreement with the already studied case of no attenuation in the coaxial; eventually we try to clarify the physical meaning of each term of the dipole moments formula.

To find the expression for the dipole moments on each hole, we replace in their definition (Eqs. (1.1)) the scattered field. A TEM field radiated by a hole centred in $z = z_i$ can be written as

$$\begin{aligned} E_{sr}\left(z, z_i\right) &= c_{0i} e_{0r} e^{-jk_c(z-z_i)} \theta\left(z - z_i\right) + d_{0i} e_{0r} e^{jk_c(z-z_i)} \theta\left(-z + z_i\right), \\ H_{s\varphi}\left(z, z_i\right) &= c_{0i} h_{0\varphi} e^{-jk_c(z-z_i)} \theta\left(z - z_i\right) - d_{0i} h_{0\varphi} e^{jk_c(z-z_i)} \theta\left(-z + z_i\right), \end{aligned} \tag{1.5}$$

where k_c is the propagation constant, $\theta(z)$ the Heaviside function

$$\theta(z) = \begin{cases} 1 & \text{for } z > 0 \\ 0 & \text{for } z < 0 \end{cases}$$

and $e_{0r}, h_{0\varphi}$ are the normalised modal functions for the TEM mode

$$e_{0r} = \sqrt{\frac{Z_0}{2\pi}} \frac{1}{\sqrt{\ln\left(d/b\right)}} \frac{1}{r}, \quad h_{0\varphi} = \frac{1}{Z_0} e_{0r}. \tag{1.6}$$

The coefficients c_{0i} and d_{0i} depend on the source field and they are

$$
\begin{aligned}
c_{0i} &= \frac{j\omega}{2}\left[\mu h_{0\varphi} M_\varphi(z_i) + e_{0r} P_r(z_i)\right], \\
d_{0i} &= -\frac{j\omega}{2}\left[\mu h_{0\varphi} M_\varphi(z_i) - e_{0r} P_r(z_i)\right],
\end{aligned}
\tag{1.7}
$$

according to Lorentz reciprocity principle (see for instance [5]). The scattered field $E_{sr}, H_{s\varphi}$ in a generic hole, centred in z_i, appearing in Eq. (1.1) is the sum of the field scattered by each hole, thus

$$
\begin{aligned}
E_{sr}(z_i) &= e_{0r}\left[\sum_{k=1}^{i-1} c_{0k} e^{-jk_c(z_i-z_k)} + \frac{c_{0i}+d_{0i}}{2} + \sum_{k=i+1}^{N} d_{0k} e^{jk_c(z_i-z_k)}\right], \\
H_{s\varphi}(z_i) &= h_{0\varphi}\left[\sum_{k=1}^{i-1} c_{0k} e^{-jk_c(z_i-z_k)} + \frac{c_{0i}+d_{0i}}{2} - \sum_{k=i+1}^{N} d_{0k} e^{jk_c(z_i-z_k)}\right];
\end{aligned}
\tag{1.8}
$$

it depends, through c_{0i} and d_{0i}, on the dipole moments themselves. Replacing Eq. (1.7) in Eq. (1.8) one obtains

$$
\begin{aligned}
M_\varphi(z_i) = \alpha_m \Bigg[& H_{0\varphi}(z_i) - j\frac{\omega}{2}\mu h_{0\varphi}^2 \sum_{h=1}^{N} M_\varphi(z_h) e^{-jk_c|z_h-z_i|} + \\
& + j\frac{\omega}{2} h_{0\varphi} e_{0r} \sum_{h=1}^{N} P_r(z_h)\, sgn(h-i) e^{-jk_c|z_h-z_i|}\Bigg], \\
P_r(z_i) = \varepsilon\alpha_e \Bigg[& E_{0r}(z_i) - j\frac{\omega}{2} e_{0r}^2 \sum_{h=1}^{N} P_r(z_h) e^{-jk_c|z_h-z_i|} + \\
& + j\frac{\omega}{2}\mu h_{0\varphi} e_{0r} \sum_{h=1}^{N} M_\varphi(z_h)\, sgn(h-i) e^{-jk_c|z_h-z_i|}\Bigg].
\end{aligned}
\tag{1.9}
$$

Equations (1.9) are an inhomogeneous $2N \times 2N$ linear system whose unknowns are the dipole moments M_φ and P_r. Using the first order iterative solution discussed in [5], i.e. substituting in the right-hand side of Eqs. (1.9) the approximate values (that is the zero order solution)

$$
M_\varphi^{(0)}(z) = \alpha_m H_{0\varphi}(z) \quad \text{and} \quad P_r^{(0)}(z) = \varepsilon\alpha_e E_{0r}(z), \tag{1.10}
$$

we get (see Appendix A.1)

$$
\begin{aligned}
M_\varphi(z_i) &\simeq \alpha_m H_{0\varphi}(z_i)\left\{1 - j\frac{k_0}{4\pi b^2 \ln(d/b)}\left[\alpha_m + (\alpha_e+\alpha_m) F_i\, e^{-\alpha z_i} + (\alpha_m - \alpha_e) B_i\right]\right\}, \\
P_r(z_i) &\simeq \varepsilon\alpha_e E_{0r}(z_i)\left\{1 - j\frac{k_0}{4\pi b^2 \ln(d/b)}\left[\alpha_e + (\alpha_e+\alpha_m) F_i\, e^{-\alpha z_i} - (\alpha_m - \alpha_e) B_i\right]\right\},
\end{aligned}
\tag{1.11}
$$

where

$$F_k = \sum_{w=1}^{k-1} e^{\alpha z_w} \quad \text{and} \quad B_k = \sum_{w=1}^{N-k} e^{-(j2k_0+\alpha)(z_{w+k}-z_k)}.$$

We remind that each hole is identified by the position of its centre (z_k) with respect to the first hole ($z_1 = 0$). In spite of their apparent complexity, Eqs. (1.11) allow us to treat directly any kind of spacing between the holes.

In the limit of low attenuation ($\alpha(\omega)\, z_k \to 0 \quad \forall\, \omega \, \text{and} \, k = 1, \ldots, N$), we find that

$$F_k \to k-1 \quad \text{and} \quad B_k = \sum_{w=1}^{N-k} e^{-j2k_0(z_{w+k}-z_k)}, \tag{1.12}$$

leading to the results already given in [5].

Before going on, we may clarify the physics behind Eqs. (1.11). Rewriting only the equation for $M_\varphi\,(z_h)$ with no attenuation, yields

$$\begin{aligned} M_\varphi(z_h) \simeq \alpha_m H_{0\varphi}(z_h) \Bigg\{ 1 - j\frac{k_0}{4\pi b^2 \ln{(d/b)}} \Bigg[& \alpha_m + (\alpha_e + \alpha_m)\,(h-1) + \\ & + (\alpha_m - \alpha_e) \sum_{w=1}^{N-h} e^{-j2k_0(z_{w+h}-z_h)} \Bigg] \Bigg\}. \end{aligned} \tag{1.13}$$

In the square brackets we recognise three terms, with the following meaning:

term $\propto \alpha_m$**:** it is the effect of the hole on itself and it is present even with a single hole ($h = N = 1$).

term $\propto (\alpha_m + \alpha_e)$**:** it is the effect of the preceding holes; the h-th hole has $h-1$ preceding holes which are interacting with it by means of a forward propagating TEM wave. Since the charge field and the TEM wave are synchronous, there is no phase factor in this term.

term $\propto (\alpha_m - \alpha_e)$**:** this is the effect of the following holes interacting with the h-th hole through the backward propagating TEM wave. Since charge field and the TEM wave have the same phase velocity but they are going in opposite direction, the phase factor turns out to be twice the phase shift due to propagation from the hole in z_{w+h} to the one in z_h.

The distinction between "following" and "preceding" holes doesn't contradict the causality principle since we are reasoning in the fictitious Fourier space, that is considering sine waves going from time $t = +\infty$ to $t = -\infty$ at frequency ω. Moreover we notice that the forward and the backward propagating waves have different weights depending on the values of the polarizabilities (α_m, α_e have opposite signs). For circular holes $|\alpha_m|$ and $|\alpha_e|$ are different by a factor 2, while for long slots they can be very similar (slot length much larger than its width). Thus we expect that for rounded-end slots the contribution of backward propagating waves is more relevant than for circular holes. We will use this fact later. The same reasoning can be performed for $P_r(z_i)$; attenuation doesn't change substantially those arguments.

... to impedance.

We now use the previous results for the dipole moments to find the coupling impedance as a function of the position of each hole. Eventually we briefly discuss the limit of very low and very high attenuation.

Using the expressions (1.11) in Eqs. (1.4), we obtain the following relations for the imaginary part Z_{IM} and the real part Z_{RE} of the longitudinal coupling impedance

$$Z_{IM}(\omega) = Z_0 \frac{\omega}{4\pi^2 b^2 c} \left\{ N \left(\alpha_m + \alpha_e\right) + \right.$$
$$\left. - \frac{\omega}{4\pi b^2 \ln\left(d/b\right) c} \left(\alpha_m - \alpha_e\right)^2 \sum_{h=1}^{N-1} \sum_{w=1}^{N-h} e^{-\alpha(z_{w+h} - z_h)} \sin\left[2\frac{\omega}{c}\left(z_{w+h} - z_h\right)\right] \right\} \tag{1.14}$$

and

$$Z_{RE}(\omega) = Z_0 \frac{\omega^2}{16\pi^3 b^4 \ln\left(d/b\right) c^2} \left\{ N\left(\alpha_m^2 + \alpha_e^2\right) + \left(\alpha_m + \alpha_e\right)^2 \sum_{h=1}^{N} F_h e^{-\alpha z_h} + \right.$$
$$\left. + \left(\alpha_m - \alpha_e\right)^2 \sum_{h=1}^{N-1} \sum_{w=1}^{N-h} e^{-\alpha(z_{w+h} - z_h)} \cos\left[2\frac{\omega}{c}\left(z_{w+h} - z_h\right)\right] \right\}. \tag{1.15}$$

It is worth noting that Z_{IM} has a dominant term independent of the position of the holes and equal to N times the impedance of a single hole. The attenuation doesn't play an important role in this case. Its effect is more remarkable on the real part Z_{RE} since the latter strongly depends on the spacing among the holes, as already shown in [5].

In the limit of low attenuation ($\alpha(\omega)\, z_k \to 0 \quad \forall\, \omega$ and $k = 1, \ldots, N$),

$$\sum_{h=1}^{N} F_h e^{-\alpha z_h} \to \frac{N}{2}(N-1) \quad \text{and} \quad \sum_{h=1}^{N} B_h \to \sum_{h=1}^{N-1} \sum_{w=1}^{N-h} e^{-j2k_0(z_{w+h} - z_h)}; \tag{1.16}$$

those lead to the known expression for the coupling impedance when there are no losses in the coaxial region [5].

On the contrary, if the losses are such that the field scattered by one hole doesn't reach the others (namely $\alpha(\omega) \to \infty$) there is no effective interference between them and we expect also the real part of the impedance to be N times the impedance of a single hole; in this limit, indeed,

$$Z_{RE}(\omega) \to Z_0 \frac{\omega^2}{16\pi^3 b^4 \ln(d/b) c^2} N\left(\alpha_m^2 + \alpha_e^2\right). \tag{1.17}$$

Thus, increasing the attenuation in the coaxial reduces the coupling impedance until this last term becomes dominating.

1.2.2 Uniformly spaced holes

We now deal with uniformly spaced holes; after having derived the complete expression for the longitudinal coupling impedance, we will discuss some simplifications in order to arrive to a more clear and easy-to-treat formula and then we conclude by introducing approximations useful in the following analytical studies of loss factor and power loss per unit length.

Denoting by D the (uniform) distance between two consecutive holes,

$$z_h = (h-1)D \quad \text{and} \quad z_{w+h} - z_h = wD;$$

we can rewrite Eq. (1.15) as

$$\begin{aligned} Z_{RE}(\omega) = Z_0 \frac{\omega^2}{16\pi^3 b^4 \ln(d/b) c^2} & \left[N\left(\alpha_m^2 + \alpha_e^2\right) + \right. \\ \left. + (\alpha_m + \alpha_e)^2 F(D, N, \alpha) + (\alpha_m - \alpha_e)^2 B(D, N, \alpha, \omega)\right] \end{aligned} \tag{1.18}$$

where

$$F(D, N, \alpha) = \sum_{h=1}^{N} \sum_{k=1}^{h-1} e^{\alpha(z_k - z_h)} = \sum_{h=1}^{N} \sum_{k=1}^{h-1} e^{\alpha(k-h)D} \tag{1.19}$$

and

$$B(D, N, \alpha, \omega) = \sum_{h=1}^{N-1} (N-h) e^{-\alpha h D} \cos\left(2h\frac{\omega}{c}D\right). \tag{1.20}$$

It is again straightforward to give to those terms their physical meaning: the first one ($\propto N\left(\alpha_m^2+\alpha_e^2\right)$) is the contribution of non interacting holes, while the term weighted by $F\left(D,N,\alpha\right)$ ($B\left(D,N,\alpha,\omega\right)$) is due to the forward (backward) propagating TEM wave.

In the limit of low attenuation ($\alpha DN \to 0$),

$$F\left(D,N,\alpha\right) \to \frac{N}{2}(N-1) \quad \text{and} \quad B\left(D,N,\alpha,\omega\right) \to \frac{1}{2}\left[\frac{\sin\left(N\omega D/c\right)}{\sin\left(\omega D/c\right)}\right]^2 - \frac{N}{2};$$

the latter is obtained from the limit of Eq. (1.20) using the following Eq. (1.25). Thus inserting those in Eq. (1.18), we find for the coupling impedance

$$Z_{RE}(\omega) = Z_0\frac{\omega^2}{32\pi^3 b^4 \ln\left(d/b\right)c^2}\left\{N^2\left(\alpha_m+\alpha_e\right)^2 + \left(\alpha_m-\alpha_e\right)^2\left[\frac{\sin\left(N\omega D/c\right)}{\sin\left(\omega D/c\right)}\right]^2\right\}, \quad (1.21)$$

as already reported in [5].

We now give explicit expressions for Eqs. (1.19-1.20) (Sec. 1.2.2 - 1.2.2) and then look for an approximate coupling impedance (Sec. 1.2.2).

Simplification of the term accounting for forward waves

Performing the sums that define $F(D,N,\alpha)$, we get

$$F(D,N,\alpha) = \frac{\left(e^{-\alpha DN}-1\right)e^{\alpha D} + N\left(e^{\alpha D}-1\right)}{\left(e^{\alpha D}-1\right)^2}. \quad (1.22)$$

As we would expect, when $\alpha D \to \infty$, $F(D,N,\alpha) \to 0$, while in the limit of low attenuation we find, coherently with Eq. (1.16),

$$F(D,N,\alpha) \to \frac{N}{2}(N-1) \quad \text{for} \quad \alpha DN \to 0. \quad (1.23)$$

If the spacing of the pumping holes is small compared to the inverse of the attenuation constant (namely $\alpha D \ll 1$), Eq. (1.22) yields

$$F(D,N,\alpha) \simeq \frac{N}{\alpha D} + \frac{e^{-\alpha DN}-1}{(\alpha D)^2}; \quad (1.24)$$

this is the case, for instance, of the LHC in which that relation holds for all the frequencies in the bunch spectrum. Anyway we should notice that Eq. (1.23) is not exactly fulfilled since

$$\frac{N}{\alpha D} + \frac{e^{-\alpha DN}-1}{(\alpha D)^2} \to \frac{N^2}{2} \quad \text{for} \quad \alpha D \to 0;$$

nevertheless since we are usually dealing with a large number of holes ($N \gg 1$), the error introduced using Eq. (1.24) is negligible.

Simplification of the term accounting for backward waves

$$B\left(D,N,\alpha,k_0\right)=\sum_{h=1}^{N-1}(N-h)e^{-\alpha Dh}\cos\left(2hk_0D\right),\quad \text{with}\quad k_0=\frac{\omega}{c}.$$

The direct numeric evaluation of this term is very time consuming, at least for the numbers N of interest (for the 14 m long LHC dipole, N is around 900). We now present two different methods to set a more easy-to-treat expression giving complementary results.

Before going through the first derivation, we recall the following relations:

$$\sum_{h=1}^{N-1}(N-h)\cos\left(2hx\right)=\frac{1}{2}\left[\frac{\sin^2\left(Nx\right)}{\sin^2 x}-N\right],\tag{1.25}$$

$$\sum_{h=1}^{N-1}(N-h)\sin\left(2hx\right)=\frac{N\sin\left(2x\right)-\sin\left(2Nx\right)}{4\sin^2 x}.\tag{1.26}$$

Expanding the exponential as a sum of complex sine and cosine leads to

$$B=\sum_{h=1}^{N-1}(N-h)\left[\cos\left(j\alpha Dh\right)+j\sin\left(j\alpha Dh\right)\right]\cos\left(2hk_0D\right),\tag{1.27}$$

or equivalently to

$$\begin{aligned}B=&\frac{1}{2}\sum_{h=1}^{N-1}(N-h)\cos\left(2h\gamma^+D\right)+\frac{1}{2}\sum_{h=1}^{N-1}(N-h)\cos\left(2h\gamma^-D\right)+\\&+\frac{j}{2}\sum_{h=1}^{N-1}(N-h)\sin\left(2h\gamma^+D\right)-\frac{j}{2}\sum_{h=1}^{N-1}(N-h)\sin\left(2h\gamma^-D\right),\end{aligned}\tag{1.28}$$

where $\gamma^\pm=k_0\pm j\alpha/2$. Thus, inserting Eqs. (1.25–1.26), we get

$$\begin{aligned}B=&\frac{1}{4}\left[\frac{\sin^2\left(N\gamma^+D\right)}{\sin^2\left(\gamma^+D\right)}-N\right]+\frac{1}{4}\left[\frac{\sin^2\left(N\gamma^-D\right)}{\sin^2\left(\gamma^-D\right)}-N\right]+\\&+\frac{j}{2}\frac{N\sin\left(2\gamma^+D\right)-\sin\left(2N\gamma^+D\right)}{4\sin^2\left(\gamma^+D\right)}-\frac{j}{2}\frac{N\sin\left(2\gamma^-D\right)-\sin\left(2N\gamma^-D\right)}{4\sin^2\left(\gamma^-D\right)}.\end{aligned}\tag{1.29}$$

To better understand each term of this last equation, we can rewrite it as

$$\begin{aligned}B=&-\frac{N}{2}+j\frac{N}{4}\left[\cot\left(\gamma^+D\right)-\cot\left(\gamma^-D\right)\right]+\\&+\frac{1}{8}\left[\frac{2\sin^2\left(N\gamma^+D\right)-j\sin\left(2N\gamma^+D\right)}{\sin^2\left(\gamma^+D\right)}+\frac{2\sin^2\left(N\gamma^-D\right)+j\sin\left(2N\gamma^-D\right)}{\sin^2\left(\gamma^-D\right)}\right].\end{aligned}\tag{1.30}$$

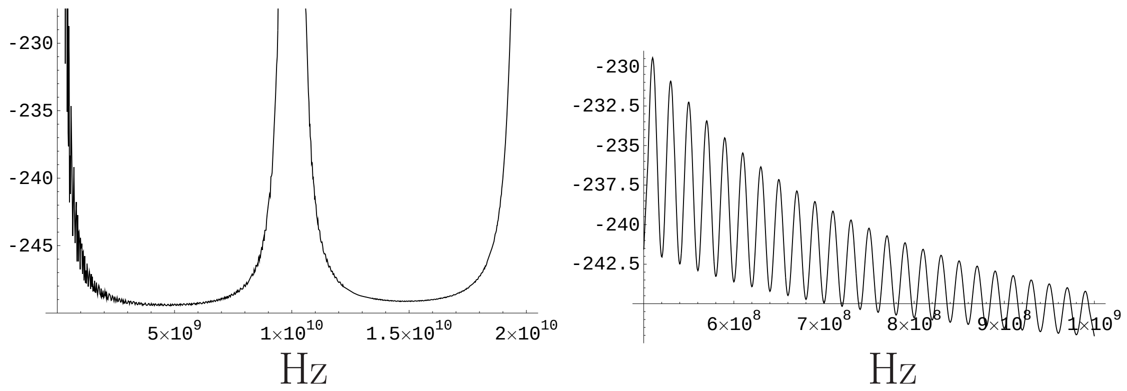

Figure 1.2: The coefficient $B(D, N, \alpha, f)$ as a function of frequency (Hz) for $N = 500$ holes. The attenuation constant α depends on the square root of the frequency (see Eq. (1.45)); all the parameters are chosen as in the case of LHC (see Table 1.1). (b) is a zoom of the "plateau" between the peaks and shows the presence of a ripple. Since α is increasing with frequency ($\alpha \propto \sqrt{\omega}$), the attenuation is more efficient at higher frequencies and thus the ripple becomes smaller. For lower N, the amplitude of the ripple increases.

Figure 1.2 is a plot of B as a function of frequency, using the LHC nominal parameters (see [1]); the attenuation constant α is chosen to depend on the square root of the frequency (case of non anomalous ohmic losses in the coaxial region). The constant term $-N/2$ in Eq. (1.30) gives the minimum value of the plateau; the second term is (roughly speaking) responsible for the main peaks. They occur at frequencies such that

$$k_0 D = n\pi \quad \text{that is} \quad f_n = n\frac{c}{2D}; \tag{1.31}$$

their width depends on the attenuation constant and their height is proportional to N^2. Due to the small value of D, those frequencies are well above the relevant part of the bunch spectrum; infact if we assume a longitudinal Gaussian beam with r.m.s. bunch length σ, its frequency spectrum is still Gaussian with a r.m.s. frequency of $f_c = c/2\pi\sigma$ (at top energy, $\sigma = 7.5\,\mathrm{cm}$ implies $f_c = 640\,\mathrm{MHz}$); f_c is sometimes called cut-off frequency of the bunch. The planned partial randomisation of the position of the holes widens those peaks and reduces their heights even if it doesn't affect the loss factor (see [5]). Moreover we just have to mention that at those frequencies other modes are propagating both in the coaxial region and in the beam pipe and they are no longer synchronous with the beam. Due to imperfections in the coaxial region (the holes themselves or anything perturbing our ideal geometry), they can exchange energy with the TEM mode we are treating and therefore this scenario could be too pessimistic. Anyway, a detailed study in this sense has not been done, at least for many holes; for a single hole a numerical study based on field matching method has been performed [11] and the results agree with what reported here. As shown in Fig. 1.2, there is a ripple superimposed onto the plateau; as it can be seen from the third term in Eq. (1.30), its frequency is

$$Nk_0D = \pi \quad \text{that is} \quad f = \frac{c}{2DN}. \tag{1.32}$$

Strictly speaking, the third term in Eq. (1.30) gives also a minor contribution to the values of the peaks. Increasing the amount of attenuation the peaks widen and their height decreases, while the frequency of the ripple and the minimum value of the plateau remain unchanged; a deeper study of Eq. (1.30) can help in giving a quantitative evaluation of this effects.

It is worth remarking that B (i.e. the effect of backward propagating waves) has a component not depending on the frequency (nor on the attenuation). So even if the major peaks are surely out of the bunch spectrum, the backward propagating wave has indeed an effect at low frequency.

An automatic evaluation of B, based on Eq. (1.30) is still very time consuming, so we propose to simplify it by rewriting the cosine in B as the real part of a complex exponential so that

$$B = Re\left[\sum_{h=1}^{N-1}(N-h)e^{-\alpha Dh - j2hk_0D}\right] = Re\left[\sum_{h=1}^{N-1}(N-h)e^{-\beta Dh}\right] \quad \text{with} \quad \beta = \alpha + j2k_0. \tag{1.33}$$

It is easy to see that

$$\sum_{h=1}^{N-1}(N-h)q^h = \frac{q\left(N - Nq + q^N - 1\right)}{(1-q)^2}; \tag{1.34}$$

using this relation with $q = e^{-\beta D}$ and taking the real part we obtain the exact value for B. We have used it in drawing Fig. 1.2 and we will use it in all the following numerical calculations.

Far away from the resonances and for large numbers N, we can approximate B simply with the constant value of Eq. (1.30); we will exploit this later, since the peak at low frequency has no big effect on the overall impedance because the contribution due to B is weighted by the frequency squared. What is lost in this approximation is the contribution of the ripple, but the latter becomes more and more negligible with increasing number of holes.

An approximate expression for the coupling impedance

We already discussed useful approximations for $F(D,N,\alpha)$ and $B(D,N,\alpha)$; our aim is now to put them together in a simplified expression for the coupling impedance. This will be important later for the analytical estimate of the loss factor. Recalling that

$$F(D,N,\alpha) \simeq \frac{N}{\alpha D} + \frac{e^{-\alpha DN}-1}{(\alpha D)^2} \quad \text{for} \quad \alpha D \ll 1,$$

$$B(D,N,\alpha,\omega) \simeq -\frac{N}{2} \quad \text{far from the peaks}$$

and inserting in Eq. (1.18) yields

$$Z_{RE}(\omega) \simeq Z_0 \frac{\omega^2\,(\alpha_m+\alpha_e)^2}{16\pi^3 b^4 \ln{(d/b)} c^2} \left[\frac{N}{2} + \frac{N}{\alpha D} + \frac{e^{-\alpha DN}-1}{(\alpha D)^2}\right]. \tag{1.35}$$

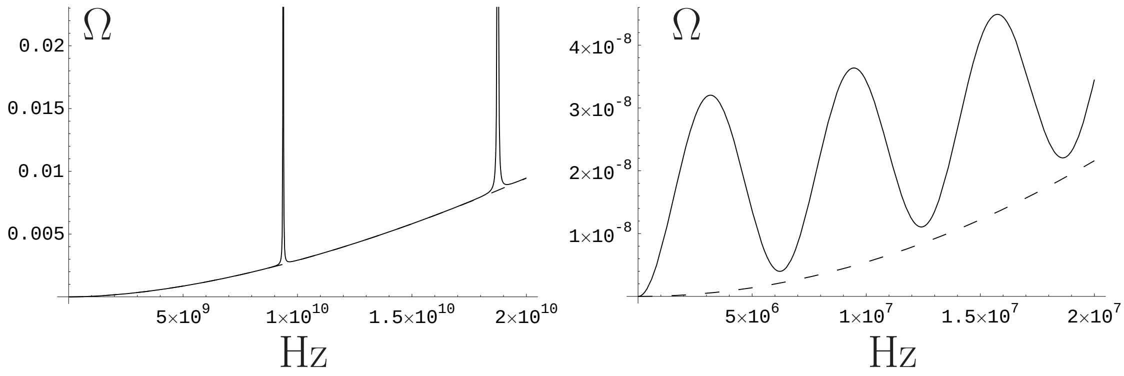

Figure 1.3: Comparison between the exact expression for the coupling impedance (solid line) and the approximated one (dashed line), for 1500 rounded-end holes (that is a ~ 24 m long device). In a) they can be hardly distinguished far from the peaks, while the difference is clear in the zoom at low frequencies b). All numerical values are taken from LHC parameters (see Table 1.1) and we have included the corrections due to the wall thickness (see Sec. 1.5).

Figure 1.3 compares, in a practical case, the "exact" coupling impedance (Eq. (1.18)) to its approximation (Eq. (1.35)); it grows as ω^2 except near frequencies satisfying the resonance condition (1.31), i.e. near the peaks due to interference of backward propagating TEM waves in the coaxial. We see that Eq. (1.35) follows very well the exact one, at least far from resonances. In the low frequency range, we see the presence of a ripple with frequency given by (1.32); it is not considered in our approximation. Increasing N, the ripple becomes more and more negligible (with respect to other terms); moreover, using Eq. (1.35) leads to a remarkable simplification in the following computation allowing us to provide analytical results for the loss factor, as we will see in Sec. 1.3 where we show that the discrepancy presented in Fig. 1.3.b has no important effect.

1.2.3 Considering only the forward propagating TEM wave

Most of the literature includes only the forward propagating TEM wave in the coaxial region; the reason being that one can expect from it the major contribution to losses since it is travelling synchronous with the beam. Anyway this assumption is somehow arbitrary, since it is well known from the theory of directional microwave couplers (see for instance [22]) that the back-scattered wave plays its role and is usually exploited to synthetize the frequency behaviour of the directivity of the coupler. In this subsection we will compare this approach to our previous one, discussing the differences in our practical case (LHC).

Going back to the equivalent hole dipoles (Eq. (1.11)), neglecting the backward wave they become in this case:

$$\begin{aligned} M_\varphi(z_i) &\simeq \alpha_m H_{0\varphi}(z_i)\left\{1 - j\frac{k_0}{4\pi b^2\ln(d/b)}\left[\alpha_m + (\alpha_e+\alpha_m)\,F_i\,e^{-\alpha z_i}\right]\right\}, \\ P_r(z_i) &\simeq \varepsilon\alpha_e E_r(z_i)\left\{1 - j\frac{k_0}{4\pi b^2\ln(d/b)}\left[\alpha_e + (\alpha_e+\alpha_m)\,F_i\,e^{-\alpha z_i}\right]\right\}. \end{aligned} \tag{1.36}$$

Thus, the coupling impedance is

$$\begin{aligned} Z(\omega) &= jZ_0\frac{\omega}{4\pi^2b^2c}N\left(\alpha_m+\alpha_e\right) + \\ &+ Z_0\frac{\omega^2}{16\pi^3b^4\ln(d/b)c^2}\left[N\left(\alpha_m^2+\alpha_e^2\right) + (\alpha_m+\alpha_e)^2\sum_{h=1}^{N}F_h e^{-\alpha z_h}\right] \end{aligned} \tag{1.37}$$

and rewriting the real part for uniformly spaced holes, we get:

$$Z_{RE}(\omega) = Z_0\frac{\omega^2}{16\pi^3b^4\ln(d/b)c^2}\left[N\left(\alpha_m^2+\alpha_e^2\right) + (\alpha_m+\alpha_e)^2 F\left(D,N,\alpha\right)\right], \tag{1.38}$$

using the previous notations. The meaning of the two terms is clear: the non interacting holes (first one) and the interference effect due to forward propagating wave (second one).

Fig. 1.4 compares graphically this last equation with the exact one (Eq. (1.18)), in the LHC case. We remind that the resonant peaks (see Fig. 1.4.a) and the ripple (see Fig. 1.4.b) are due to the backward wave and so they are lost if we consider only the forward wave. The difference between the dashed and solid lines in Fig. 1.4 and 1.3 is thus due to the constant term ($\propto N/2$) coming from $B(D,N,\alpha,\omega)$.

In conclusion we see that, at least for a LHC-like geometry, the main differences between considering and not considering the backward waves are at frequencies well above the cut-off of the bunch spectrum. Nevertheless also at low frequency (inside the bunch spectrum) there is a difference, even though not a substantial one.

It is worth noting that the relative influence of the back - forward waves depends on the hole shape, since the two terms are weighted with different functions of the polarizabilities. For instance, with circular holes the difference seen in Fig. 1.4.a (that is for rounded-end holes) is far less evident.

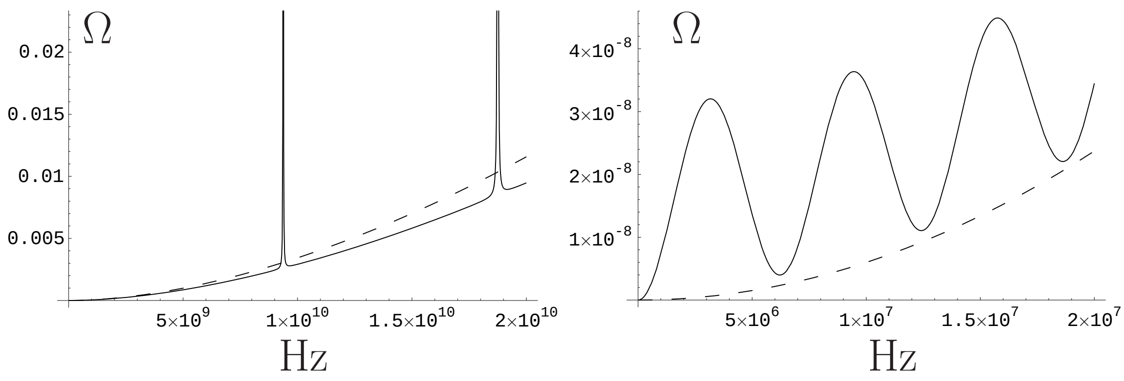

Figure 1.4: Comparison between the exact expression for the coupling impedance (solid line) and the one obtained considering only the forward propagating waves (dashed line), for 1500 rounded-end holes. b) is a detail at low frequencies. All numerical values are taken from LHC parameters (see Table 1.1) and we have included the corrections due to effects of the wall thickness (see Sec. 1.5).

1.3 Loss Factor

The loss factor is the energy lost by the bunch normalised to its charge squared; it depends on the coupling impedance and, for a Gaussian bunch of length σ, it can be written

$$k(\sigma) = \frac{1}{\pi} \int_0^\infty Z_{RE}\,(\omega)\, e^{-(\omega\,\sigma/c)^2} d\omega, \tag{1.39}$$

as we anticipated in Sec. 1.1.1.

First we introduce an approximation for bunch length bigger than the spacing among the holes and when the losses in the coaxial are negligible. Then we study the loss factor when there are ohmic losses giving analytical formulae and discussing the approximations involved.

1.3.1 Loss factor without attenuation

The integral in the loss factor can be performed analytically in this case, as reported in [5]. We now remind that formula and show some useful simplifications valid if the length of the bunch is longer than the distance between the holes and for a large number of them.

The coupling impedance with no losses in the coaxial region is reported in Eq. (1.21); rewriting it with the help of Eq. (1.25) and performing the integration (1.39) yields

$$k(\sigma) = \frac{Z_0\sqrt{\pi}c}{128\pi^4 b^4 \ln(d/b)\sigma^3}\left[N^2(\alpha_m+\alpha_e)^2 + N(\alpha_m-\alpha_e)^2 - 2(\alpha_m-\alpha_e)^2 S\right], \tag{1.40}$$

where

$$S = \sum_{h=1}^{N-1}(N-h)e^{-(hD/\sigma)^2}\left[2\left(\frac{D}{\sigma}h\right)^2 - 1\right]. \tag{1.41}$$

As shown in Appendix A.2, for large N Eq. (1.41) can be approximated by

$$S \simeq \frac{1}{2}\left[N - \left(\frac{\sigma}{D}\right)^2\right] \qquad \text{if} \qquad \frac{D}{\sigma} < 1 \tag{1.42}$$

since many terms of the sum are negligible; the loss factor (1.40) becomes

$$k(\sigma) \simeq \frac{Z_0\sqrt{\pi}c}{128\pi^4 b^4 \ln(d/b)\sigma^3}\left[N^2(\alpha_m+\alpha_e)^2 + \left(\frac{\sigma}{D}\right)^2(\alpha_m-\alpha_e)^2\right]. \tag{1.43}$$

The dependence on N^2 takes into account interference effects between the holes and it is physically sound. Moreover, if

$$\frac{1}{N^2}\left(\frac{\sigma}{D}\right)^2\frac{(\alpha_m-\alpha_e)^2}{(\alpha_m+\alpha_e)^2} \ll 1,$$

the loss factor is proportional to N^2, although it is not N^2 times the loss factor of a single hole (that is proportional to $(\alpha_m^2+\alpha_e^2)$). In formulae

$$k(\sigma) \simeq \frac{Z_0\sqrt{\pi}c}{128\pi^4 b^4 \ln(d/b)\sigma^3}N^2(\alpha_m+\alpha_e)^2 \qquad \text{if} \qquad N \gg A\frac{\sigma}{D} \qquad A = \frac{(\alpha_m-\alpha_e)}{(\alpha_m+\alpha_e)}. \tag{1.44}$$

In the case of circular holes in a thin wall, for example, $A = 3$.

The result of Eq. (1.44) shows the importance of the interference effects between the holes due to the presence of the TEM field in the coaxial region. These effects are not always considered in the literature and they cause the total loss factor to depend on N^2; for example [12] proposes, for the same geometry, to estimate the total energy lost by the bunch by taking N times the loss factor for a single hole.

1.3.2 Attenuation due to ohmic losses

We have studied the impedance for an attenuation source in the coaxial region such that the field propagating there remains essentially TEM shaped; this is for instance the case of distributed dielectric losses.

In first approximation, also the effect of lossy walls can be treated in this way by using the following attenuation constant [7]

$$\alpha(\omega) = a\sqrt{\omega} \qquad \text{with} \qquad a = \frac{1}{2\,Z_0\,\ln(d/b)}\left(\frac{\sqrt{\rho_b}}{b} + \frac{\sqrt{\rho_d}}{d}\right)\sqrt{\frac{\mu}{2}} \tag{1.45}$$

where ρ_b (ρ_d) is the resistivity of the cylindrical surface of radius b (d). Although it is only an approximation, this approach is widely used in the estimation of losses in high power RF transmission lines [19].

Using Eq. (1.45) in Eq. (1.18) yields the real part of the coupling impedance for this particular source of losses and then performing the integral of Eq. (1.39), we get the loss factor. Unfortunately this cannot be done analytically and we use now the approximations for the coupling impedance discussed earlier, namely the one including only the forward propagating TEM wave of Eq. (1.38) and the one including everything but the peaks of the impedance, see Eq. (1.35).

First of all, to check their validity, we focus on the function under the integral, that is Z_{RE} times the bunch current in absolute squared value (i.e. the Gaussian of Eq. (1.39) modulo some constant), that is the spectrum in frequency of the power lost by the bunch.

Figure 1.5 shows the function under the integral, when we include only the effect of forward propagating waves, namely using Eq (1.38) for the coupling impedance; Fig. 1.5.b shows the detail at low frequency, where the ripple is again due to interference effects associated to backward scattered waves. Thus there is a difference between the exact and the approximated one, but it is not dramatic and it leads to an overestimated value of the loss factor.

On the other hand, Fig. 1.6 compares the exact value of the spectrum of the power lost by the beam with the one we got by using Eq. (1.35). The difference can not be seen in a wide frequency range (Fig. 1.6.a), but is clear at low frequencies even if it is very small.

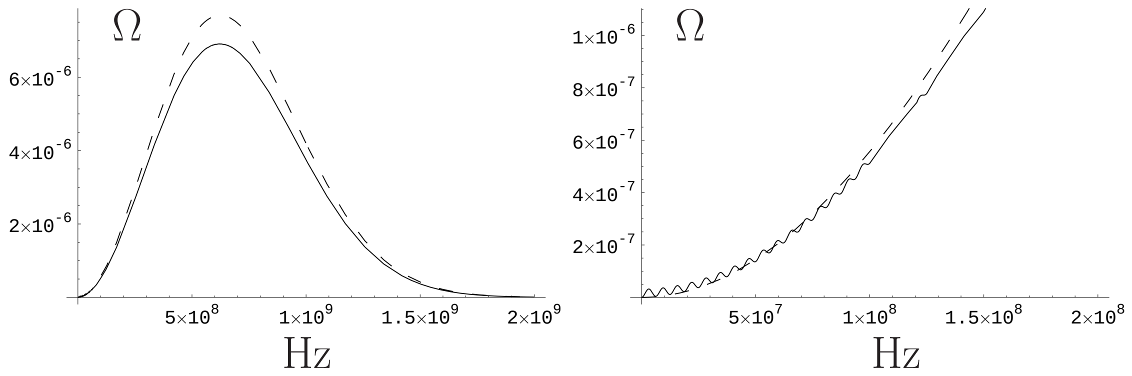

Figure 1.5: Function under the integral of the loss factor using the exact expression for the coupling impedance (solid line) and considering only the forward propagating waves (dashed line), for 1500 rounded-end holes. b) is a detail at low frequencies. All numerical values are taken from LHC parameters (see Table 1.1) and we are including the corrections due to effects of the wall thickness (see Sec. 1.5).

The previous curves correspond to a fixed number of holes ($N = 1500$ that is a section 24 m long); decreasing the number of holes increases the magnitude of the ripple (as seen in Sec. 1.2.2) and our approximate formulae lose in accuracy, even though the result remains acceptable, as we will show.

Thus, both approximations are not far from reality, although they do not take into account the sharp peaks of the impedance; infact those peaks are outside the relevant spectrum of the bunch.

We now use the two approximate formulae for the coupling impedance, Eqs. (1.35) and (1.38), to derive analytically the loss factor and we compare it with numerical results using the exact impedance.

Since

$$I_1 = \int_0^\infty \omega^2 e^{-(\omega\sigma/c)^2} d\omega = \frac{\sqrt{\pi}}{4}\left(\frac{c}{\sigma}\right)^3, \quad I_2 = \int_0^\infty \omega^{3/2} e^{-(\omega\sigma/c)^2} d\omega = \frac{1}{2}\Gamma\left(\frac{5}{4}\right)\left(\frac{c}{\sigma}\right)^{5/2},$$

$$I_3 = \int_0^\infty \omega\left(e^{-aDN\sqrt{\omega}} - 1\right) e^{-(\omega\sigma/c)^2} d\omega =$$
$$-\frac{c^2}{2\sigma^2} + \frac{c^2}{2\sigma^2}\, {}_1F_3\left(1; \frac{1}{4}, \frac{1}{2}, \frac{3}{4}; \frac{a^4c^2}{256\sigma^2}N^4D^4\right) - \Gamma\left(\frac{5}{4}\right)\frac{a}{2}\left(\frac{c}{\sigma}\right)^{5/2}\, {}_0F_2\left(; \frac{1}{2}, \frac{3}{4}; \frac{a^4c^2}{256\sigma^2}N^4D^4\right) ND +$$
$$+\frac{\sqrt{\pi}a^2c^3}{8\sigma^3}\, {}_0F_2\left(; \frac{3}{4}, \frac{5}{4}; \frac{a^4c^2}{256\sigma^2}N^4D^4\right) N^2D^2 - \Gamma\left(\frac{3}{4}\right)\frac{a^3}{16}\left(\frac{c}{\sigma}\right)^{7/2}\, {}_0F_2\left(; \frac{5}{4}, \frac{3}{2}; \frac{a^4c^2}{256\sigma^2}N^4D^4\right) N^3D^3,$$

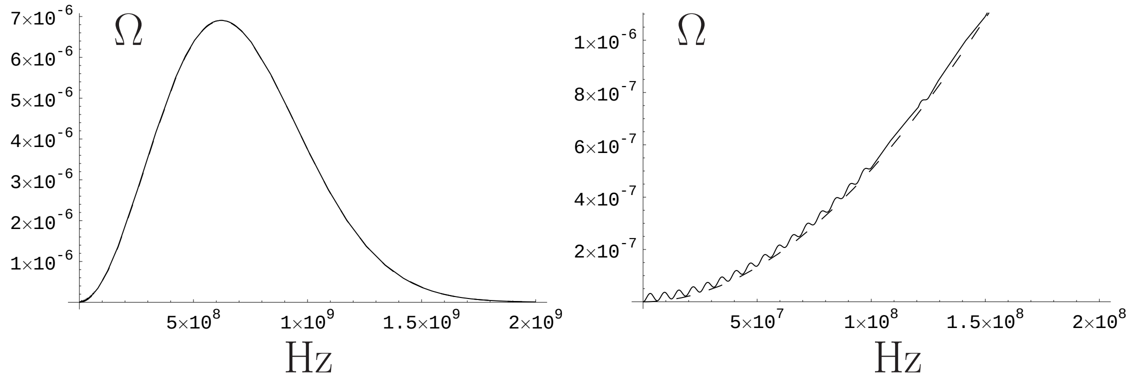

Figure 1.6: Function under the integral of the loss factor using the exact expression for the coupling impedance (solid line) and the approximation valid far from the frequencies of its peaks (dashed line), for 1500 rounded-end holes. In a) they can be hardly distinguished, while the difference is clear in the detail at low frequencies b). All numerical values are taken from LHC parameters (see Table 1.1) and we are including the corrections due to effects of the wall thickness (see Sec. 1.5).

where ${}_pF_q$ is the generalised hypergeometric series [16], we get

$$k(\sigma) = \frac{Z_0\left(\alpha_m + \alpha_e\right)^2}{16\pi^4 b^4 \ln\left(d/b\right) c^2}\left[\frac{\sqrt{\pi}}{8}\left(\frac{c}{\sigma}\right)^3 N + \frac{1}{2}\Gamma\left(\frac{5}{4}\right)\frac{c^{5/2}}{aD\sigma^{5/2}}N + \frac{I_3}{a^2 D^2}\right]. \tag{1.46}$$

In the limit of large N the third term in the square brackets becomes negligible with respect to the other two, as it is clear from the definition of I_3.

The behaviour of the loss factor as a function of the length of perforated screen L_d is shown in Fig. 1.7. When L_d (or N) is small, the holes interfere as if no attenuation was present in the coaxial region and the loss factor grows quadratically (Fig. 1.7.a). As the length increases, not all the holes interact with each other since the attenuation damps the field; if two holes are too far away their contribution to the losses is simply the sum of the contributions of the two non interacting holes. Thus, for large lengths the loss factor grows linearly, as seen in Fig. 1.7.b. The dashed line is the loss factor accounting only for forward propagating waves in the coaxial, while the solid one includes also the back-scattered waves; the dots are numerical values of the loss factor integral including the exact impedance of Eq. (1.18). The agreement of the results is good: at the length of 15 m the error between the solid line and the numerical result is of 0.3% while for the dashed it is 17%. Going to small lengths, our approximations loses in accuracy since the term B of Eq. (1.18) can not be approximated simply by a constant, as already said. Thus we expect a bigger error for small length, as we see in Fig. 1.8.

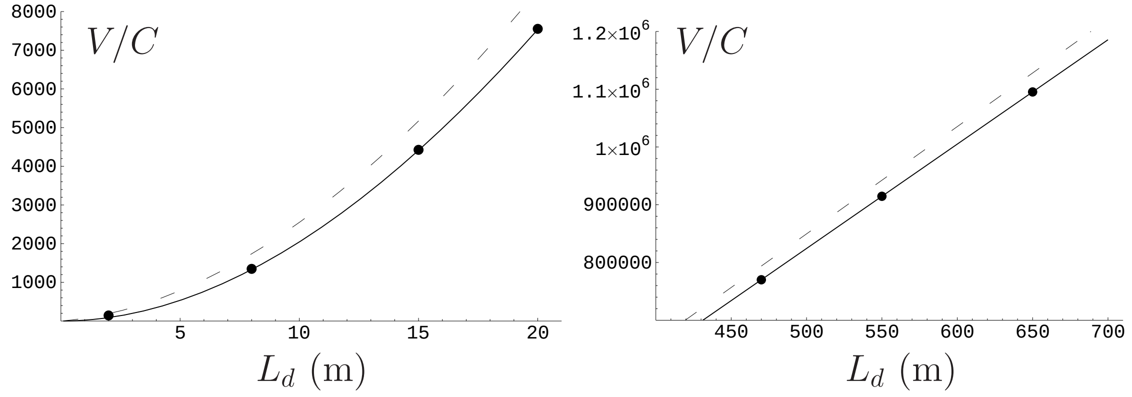

Figure 1.7: Loss factor as a function of the length of the beam screen. The dots are obtained numerically using the exact coupling impedance, while the lines are the analytical approximations including only forward waves (dashed) and the impedance without the peaks. All numerical values are taken from LHC parameters (see Table 1.1) and we are including the corrections due to effects of the wall thickness (see Sec. 1.5).

1.4 Power lost per unit length

The excited TEM field dissipates power on the walls of the coaxial region, causing heating of the cold bore; thus, providing an estimate of such power is essential in the project of the LHC.

We first discuss the connection between the power per unit length and the loss factor, then we provide an analytical formula, using previous results for $k(\sigma)$. To better understand and to achieve handy formulae, we focus on the two limiting behaviours (namely for very small and infinite lengths) and define a boundary between these two. Eventually we treat the case of more than one hole per cross section.

The energy lost by the bunch in a section of length $L_d = ND$ is the loss factor times Q^2, where Q is the charge of the bunch. If the inner part of the beam screen is a perfect conductor, all the energy lost by the bunch is transferred to the propagating field (energy conservation law). Dividing that energy by the time the bunch takes to cover the length L_d (i.e. L_d/c for relativistic bunches) yields the power flowing in the coaxial. The ratio between this and again the length L_d is defined as the power per unit length and takes into account the effect of a single bunch travelling in the inner pipe. If we assume that the total power is the sum of the power due to each of the n_b bunches in a length L_d, we get the expression of

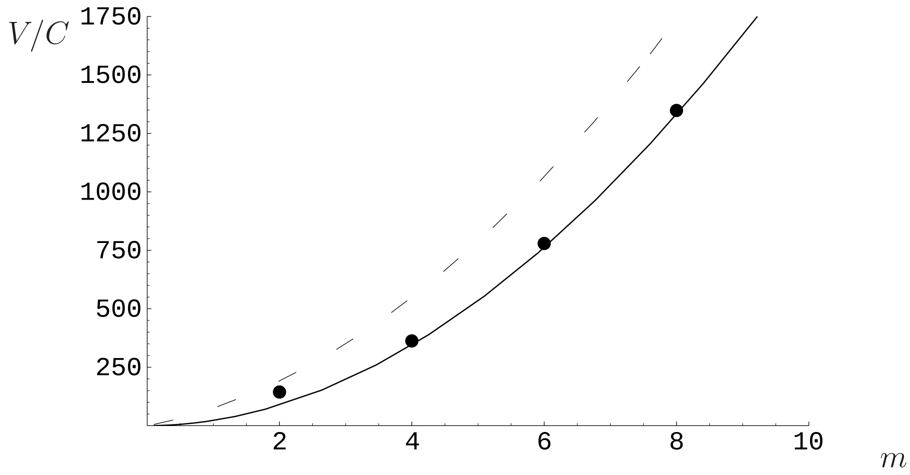

Figure 1.8: Loss factor as a function of the length of the beam screen. The dots are obtained numerically using the exact coupling impedance, while the lines are the analytical approximations including only forward waves (dashed) and the impedance without the peaks (solid). All numerical values are taken from LHC parameters (see Table 1.1) and we are including the corrections due to effects of the wall thickness (see Sec. 1.5).

the power per unit length given in Sec. 1.1.1:

$$P = n_b \frac{c\, Q^2\, k\,(\sigma)}{L^2} = \frac{c\, Q^2\, k\,(\sigma)}{S_b\, L}, \tag{1.47}$$

where S_b is the bunch spacing ($S_b = L_d/n_b$).

In Sec. 1.3.1 we derived and discussed an analytical expression for $k(\sigma)$ that was found to be a very good approximation of the real one; inserting it in Eq. (1.47) yields

$$P = \frac{(\alpha_m + \alpha_e)^2}{16\,\pi^4\, b^4\, \ln{(d/b)}\, S_b\, D} \left[\frac{\sqrt{\pi}}{8} \frac{Z_0\, Q^2\, c^2}{\sigma^3} + \frac{1}{2}\Gamma\!\left(\frac{5}{4}\right) \frac{Z_0\, Q^2\, c^{3/2}}{a\, D\, \sigma^{5/2}} + \frac{1}{N} \frac{Z_0\, Q^2\, I_3}{a^2\, D^2\, c} \right]. \tag{1.48}$$

A typical behaviour of P with the device length L_d ($L_d = ND$) is drawn in Fig. 1.9, for the nominal LHC case. The distance between the holes D and their number N are such that the surface covered by the holes is the 4.4% of the total surface of the pipe.

As shown in Fig. 1.9, there are two simple limiting behaviours of P: it saturates for very long devices, while it grows linearly when the length L_d is small.

In the limit of large L_d, Eq. (1.48) becomes constant:

$$P_\infty = \lim_{N\to\infty} P = \frac{(\alpha_m + \alpha_e)^2}{16\,\pi^4\, b^4\, \ln{(d/b)}\, S_b\, D} \left[\frac{\sqrt{\pi}}{8} \frac{Z_0\, Q^2\, c^2}{\sigma^3} + \frac{1}{2}\Gamma\!\left(\frac{5}{4}\right) \frac{Z_0\, Q^2\, c^{3/2}}{a\, D\, \sigma^{5/2}} \right]. \tag{1.49}$$

The physical reason is that over a certain length, the number of holes interacting with each other is fixed by the attenuation of the field: increasing the number of holes (i.e. L_d) doesn't

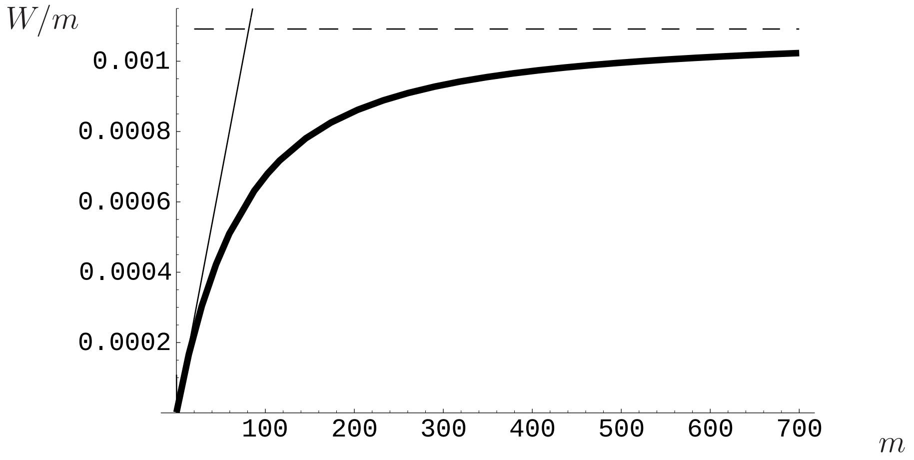

Figure 1.9: Power per unit length (W/m) as a function of the length of the beam screen (m). The thick line is the exact value, while the solid thin line accounts for the case without losses; the dashed one is the limit value, reached at very long length. All numerical values are taken from LHC parameters (see Table 1.1) and we are including the corrections due to effects of the wall thickness (see Sec. 1.5); the number and the distance between the rounded-end slots are chosen such that the surface covered by the holes is 4.4% of the surface of the pipe.

change the losses per unit length. In this range the loss factor goes linearly with L_d, see Fig. 1.7.b.

On the contrary, the attenuation doesn't dump the field efficiently in short lengths; the loss factor for such lengths grows parabolically, see Fig. 1.7.a. We can study this limit as if there were no attenuation and using Eq. (1.44) for the loss factor yields

$$P_{lin} = \frac{\sqrt{\pi}}{128\,\pi^4}\,\frac{Z_0\,Q^2\,c^2}{\sigma^3}\,\frac{(\alpha_m+\alpha_e)^2}{b^4\,D\,S_b\,\ln(d/b)}\,N. \tag{1.50}$$

It grows linearly with N (or L_d) because of the interference effect among all the holes: each hole interacts with all the others. This is actually an approximation of Eq. (1.48) for short L_d, but it gives a simple formula physically sound.

It is useful to define a boundary between these two behaviours, namely the linear and the saturated one: below that we can consider the power per unit length to grow linearly with L_d, while above we can assume it constant and equal to its saturation value P_∞. Therefore, we define L_α as the length such that the linear approximation P_{lin} crosses the limit value P_∞, that is

$$L_\alpha = D + \frac{4}{\sqrt{\pi}}\,\Gamma\!\left(\frac{5}{4}\right)\frac{\sqrt{\sigma}}{a\,\sqrt{c}} = D + \frac{4}{\sqrt{\pi}}\,\Gamma\!\left(\frac{5}{4}\right)\frac{1}{\alpha\,(\omega_c)}, \tag{1.51}$$

where $\omega_c = 2\pi f_c$ and f_c is the cut-off frequency of the Gaussian spectrum of the bunch. After L_α, the power per unit length can be approximated with its saturation value.

L_α depends on the the attenuation α, on the bunch length and on the spacing among the holes. The dependence on D is not relevant for our practical case (LHC) because the second term is orders of magnitude bigger; that dependence simply states that for very strong attenuation (i.e. $\alpha \to \infty$) the saturation value is reached at lengths equal to the spacing among the holes. This is not surprising, because (see Sec. 1.2.1) in this case the holes do not interact; consequently the coupling impedance (and thus the loss factor) is linear in L_d (or in N) and the power lost per unit length is constant. The other term is proportional to the inverse of the attenuation constant computed at the cut-off frequency f_c; it is not exactly $1/\alpha\,(\omega_c)$ (as we could expect) since the loss factor (and P) is an average on all the frequencies. For the nominal values of the LHC (see Table 1.1) L_α is about 80 m.

Up to now we have assumed a single line of holes drilled with constant spacing equal to D. If there are more than one hole for a given longitudinal position, we have to multiply our formulae by the number of holes per cross section N_b squared. Infact holes in the same section always interfere constructively, since both the charge field and the TEM one are constant in the azimuthal coordinate and thus they are excited with the same phase. Anyway in the example shown in Fig. 1.9, where the constraint is the pumping surface, increasing the number of pumping holes per cross section N_b implies an increase of the distance between the holes D. Now, the dominant term of Eq. (1.49) for P_∞, is proportional to N_b/D squared and thus its value doesn't change if we increase the number of holes per cross section. The same reasoning holds for Eq. (1.50), since if we rewrite it in terms of the length L_d ($N = L/D$), P_{lin} depends again on N_b/D squared.

1.5 The effect of wall thickness

Up to now, we have neglected the effect of the finite thickness of the wall: it changes the problem geometry and introduces an attenuation for the fields in the holes.

About the change of the problem geometry, we should notice that, because of the thickness of the wall, the radius of the pipe "seen" by the beam is different from the radius of the inner tube of the coaxial structure. Calling b_1 and b_2, respectively the inner and the outer radius of the beam pipe (see Fig. 1.1), one can show that the factor b^4 in the denominator of the expressions of impedance and loss factor has to be replaced by the product $b_1^2 b_2^2$. A similar argument holds for the $\ln(d/b)$ that becomes $\ln(d/b_2)$.

The most important correction is on the polarizabilities since the fields are exponentially attenuated going through the holes. We can imagine that the outer magnetic (electric) polarizability scales as the magnetic (electric) field going into a cylindrical waveguide of the same cross-section of the hole. Because the hole is supposed to be very small with respect to λ (since we are dealing with static polarizabilities), all the modes of these equivalent wave-guides are below cut-off and their attenuation is exponential with the thickness. If the latter is sufficiently large with respect to a typical dimension of the hole, only the contribution of the less attenuated mode (i.e. the fundamental one of the wave guide corresponding to the hole) will affect the scaling of thin wall polarizabilities. Although only approximate, this approach, presented and discussed in [20], has been adopted in [5] and also in [12].

For circular holes of radius R these modified polarizabilities are [5]

$$\begin{aligned} \tilde{\alpha}_m = C_M\, \alpha_m\, e^{-1.841\, T/R} \quad & \text{with} \quad C_M = 0.84 \quad \text{and} \quad \alpha_m = \frac{4}{3} R^3, \\ \tilde{\alpha}_e = C_E\, \alpha_e\, e^{-2.405\, T/R} \quad & \text{with} \quad C_E = 0.83 \quad \text{and} \quad \alpha_e = -\frac{2}{3} R^3, \end{aligned} \tag{1.52}$$

where $T = b_2 - b_1$ is the wall thickness and the numerical values for C_E and C_M are taken from [20]. The exponential factor is clearly related to the attenuation of fields due to the thickness. Performing the overlapping integral between the source field and the modes of the cylindrical wave-guide equivalent to the hole yields the appropriate values for C_E and C_M; due to the normalisation of wave guide modes they must be always less than 1.

The pumping holes foreseen for the beam screen of LHC are rounded-end shaped. Their "thin wall" polarizabilities are [18]

$$\begin{aligned} \alpha_m &= \frac{\pi}{16} W^2 L \left[1 - 0.0857\, \frac{W}{L} - 0.0654 \left(\frac{W}{L} \right)^2 \right], \\ \alpha_e &= -\frac{\pi}{16} W^2 L \left[1 - 0.7650\, \frac{W}{L} + 0.1894 \left(\frac{W}{L} \right)^2 \right], \end{aligned} \tag{1.53}$$

where W is the width and L is the length of the holes. In case of finite thickness of the wall they can be corrected as in [6], that is

$$\tilde{\alpha}_m = C_M \, \alpha_m \, e^{-\upsilon T} \quad \text{with} \quad \upsilon = -\frac{\pi}{W},$$
$$\tilde{\alpha}_e = C_E \, \alpha_e \, e^{-\gamma T} \quad \text{with} \quad \gamma = -\pi \sqrt{\frac{1}{L^2} + \frac{1}{W^2}}; \tag{1.54}$$

where the value proposed (using numerical results) for $C_M = C_E$ is 0.61. We should notice that γ and υ are the attenuation constants of rectangular wave-guide modes, not of "rounded-end" ones (that can not be expressed analytically). The error introduced using the "rectangular" constants is negligible. Moreover, the ratio between the thickness of the wall and the dimensions of the holes in LHC allows us to use Eqs. (1.54) that clearly take into account only the effects of one TE and one TM mode of a rectangular waveguide.

In a following section (Sec. 1.7), where are presented numerical estimates for LHC with rounded-end slots, we will take the maximum possible value for C_M and C_E, that is 1, as stated before.

1.6 Discussion

We now compare our results to a previous paper [7] which reports on some measurements done on a 2 m long model of the LHC vacuum chamber and tries to interpret them with the help of a simplified model. In Sec. 1.6.1 we consider the case of negligible attenuation (i.e. small L_d), while in Sec. 1.6.2 we discuss P_∞.

In [7] they study essentially the build up of the forward TEM wave, that is the main source of losses since it is synchronous with the beam. They derived a simple equation for the amplitude of the field in the coaxial with the holes described again by means of polarizabilities. Only circular holes were treated and the expressions of the polarizabilities are essentially the same ones given in Eq. (1.52), including the dependence on the wall thickness. They focus on the transmission coefficient (i.e. the ratio between the maximum absolute value of the field in the coaxial and the field in the beam pipe) in the two limiting cases: ignoring the attenuation (suitable for length much smaller than L_α) and for infinite length. The first case is also compared to measurements showing that the theoretical values are about a factor two below the measured ones. The effects of non interacting holes and of the backward propagating waves were ignored. These two contributes are anyway marginal, at least for the LHC: the first one is important only when the attenuation is very high ($\alpha \to \infty$), while the backward waves give remarkable contributions only at very high frequencies, at least for the LHC.

1.6.1 Forward transmission coefficient

The forward transmission coefficient is given by

$$G(\omega) = \left| \frac{E_{sr}}{E_0} \right| \tag{1.55}$$

where $E_{sr}(z)$ is the electric field radiated by all the holes in the coaxial region and the source field E_0 is that one of a relativistic charge given in Eq. (1.2).

$E_{sr}(z)$ is the superposition of the field radiated by each hole. To measure the overall transmission coefficient we will consider the field at the end of the rows of holes and Eq. (1.5) becomes

$$E_{sr}\left(z\right) = \sum_{h=1}^{N} E_r\left(z, z_h\right) = e^{-jk_0 z} \sum_{i=1}^{N} c_{0i} e_{0r} e^{jk_0 z_i}, \tag{1.56}$$

since $z > z_h \quad \forall\, h \quad (h = 1, \ldots, N)$; the coefficients c_{0i} are given by Eq. (1.7). We recall that we are considering fields in the frequency domain. Inserting Eqs. (1.6) and (1.7) into Eq. (1.56) yields

$$E_{sr}\left(z\right) = j \frac{Z_0\ \omega}{4\pi b^2 \ln\left(d/b\right)} e^{-jk_0 z} \sum_{i=1}^{N} \left[\frac{M_\varphi(z_i)}{c} + P_r(z_i) \right] e^{jk_0 z_i} \tag{1.57}$$

and eventually we get, from Eq. (1.4),

$$E_{sr}\left(z\right) = \frac{q\, Z(\omega)}{2\, b\, \ln\left(d/b\right)} e^{-j\dfrac{\omega}{c} z}. \tag{1.58}$$

The forward transmission coefficient is then

$$G(\omega) = \frac{\pi}{\ln\left(d/b\right)} \frac{|Z(\omega)|}{Z_0}. \tag{1.59}$$

Since the absolute value of the coupling impedance is dominated by its imaginary part (given in Eq. (1.14)), the coefficient $G(\omega)$ becomes

$$G(\omega) \simeq N \frac{\omega}{4\, \pi\, b_1\, b_2 \ln\left(d/b_2\right) c} \left|\tilde{\alpha}_m + \tilde{\alpha}_e\right|, \tag{1.60}$$

where we have already included the effect of the wall thickness using b_1, b_2 and the polarizabilities for "thick" wall $\tilde{\alpha}_m$ and $\tilde{\alpha}_e$, as previously discussed (Sec. 1.5). This result is identical to the analytical expression derived in [7], since when there is no attenuation, the effect of the forward propagating wave (the only one considered in [7]) dominates.

1.6.2 Power lost per unit length: the asymptotic value

The saturation value of the power lost per unit length derived in [7] and expressed in our notation is

$$\widehat{P}_\infty = \frac{1}{2}\Gamma\left(\frac{5}{4}\right) N_b^2 \frac{Z_0\, Q^2\, c^{3/2}\, \left(\tilde{\alpha}_m + \tilde{\alpha}_e\right)^2}{16\,\pi^4\, b_1^2\, b_2^2 \ln\left(d/b_2\right) S_b\, a\, D^2\, \sigma^{5/2}}. \tag{1.61}$$

It is actually the second term of Eq. (1.49) that is the one accounting for the effect of the forward propagating TEM field, having included the changes discussed in Sec. 1.5 because of the thick wall and considering N_b holes per cross section.

It is worth noting that in the complete expression the term accounting for the effect of non interacting holes and the one due to the backward wave have different signs and almost cancel each other giving the second term in the square brackets of Eq. (1.49). This explains why Eq. (1.61) gives almost exactly the value of the plateau in Fig. 1.9.

It is useful to rewrite the saturation value of the power lost as [23]

$$P_\infty = \frac{1}{2\sqrt{2}\,\pi^2}\Gamma\left(\frac{5}{4}\right) \frac{Z_0^2\, Q^2\, c^{3/2}}{\sqrt{\mu}\,\sqrt{\rho}\, S_b\, \sigma^{5/2}} \frac{b_2\, d}{\left(b_2 + d\right)\, b_1^2} \frac{\left(\tilde{\alpha}_m + \tilde{\alpha}_e\right)^2}{A^2}\, f^2, \tag{1.62}$$

by simply reminding that

$$D = N_b \frac{L_d}{N} = N_b \frac{A L_d}{2\pi b_2 L_d f} = N_b \frac{A}{2\pi b_2 f}. \tag{1.63}$$

Figure 1.10 gives a graphic representation of Eq. (1.62), showing curves of constant P_∞ for different values of the wall thickness T and the slot width W. For a reduced screen thickness of 0.5 mm and assuming the same slot width of 1.5 mm, the maximum single beam power loss would increase from about 1 mW/m to 7 mW/m. Note, however, that countersunk slots with an effective depth smaller than the screen thickness would significantly enhance the RF leakage. To keep the same safety margins on the power dissipated on the cold bore, it would then be advisable to reduce the slot width to 1 mm. A simpler formula for P_∞, fitting the exact values within a maximum error of 25% in the interesting parameter range

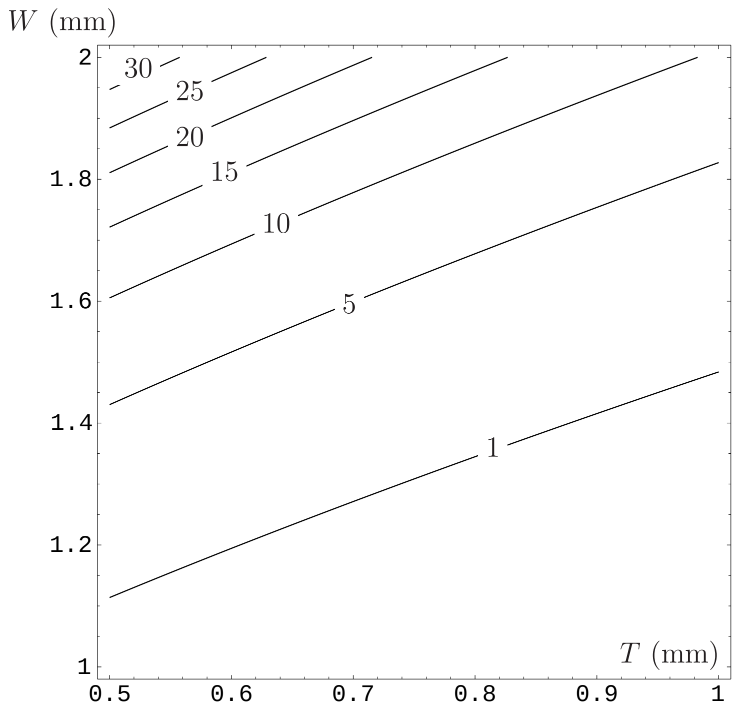

Figure 1.10: Curves of constant power per unit length, obtained with the exact formula (1.62), as a function of the wall thickness T and of the slot width W. The number on each curve gives the power per unit length in mW/m.

($T = 0.5 \div 1$ mm and $W = 1 \div 2$ mm), can be obtained by introducing the approximations $b_1 \sim b_2$, $A \sim LW$ and $L \gg W$, leading to

$$\frac{b_2\, d}{(b_2+d)\; b_1^2}\,\frac{(\tilde{\alpha}_m+\tilde{\alpha}_e)^2}{A^2} \sim \left(\frac{\pi}{16}0.68\right)^2 \frac{1}{1+b_2/d}\,\frac{1}{b_2}\,\frac{1}{L^2}\,W^4\,e^{-1.75\,\pi\,T/W}. \tag{1.64}$$

The asymptotic power loss can be eventually written

$$P_\infty \sim P_0\, e^{-1.75\,\pi\,T/W}, \tag{1.65}$$

where

$$\begin{aligned} P_0 =& 42\,\mathrm{mW/m}\left(\frac{Q}{16\times10^{-9}\,\mathrm{C}}\right)^2\left(\frac{7.1\times10^{-7}\,\Omega\mathrm{m}}{\rho}\right)^{1/2}\left(\frac{7.5\,\mathrm{m}}{S_b}\right)\left(\frac{7.5\,\mathrm{cm}}{\sigma}\right)^{5/2} \\ & \left(\frac{2\,\mathrm{cm}}{b_2}\right)\left(\frac{2}{1+\frac{b_2/d}{0.82}}\right)\left(\frac{8\,\mathrm{mm}}{L}\right)^2\left(\frac{W}{1.5\,\mathrm{mm}}\right)^4\left(\frac{f}{0.044}\right)^2. \end{aligned} \tag{1.66}$$

For convenience, all the relations involved in this paper are reported in a Mathematica notebook [24].

1.7 LHC case

All the numerical examples given before are done with LHC nominal parameters, in particular assuming rounded-end slots and the attenuation due to ohmic losses in the walls of the coaxial region (see Table 1.1 for numerical values).

The maximum power loss per unit length in the nominal case is 1.1 mW/m and L_α is 81.5 m, as we see in Fig. 1.9. Probably the pure coaxial structure will be limited only to sections shorter than L_α since all the devices such as pumps, kickers, ... will be installed outside the beam screen, resulting in different geometries for the "coaxial" region. Therefore the linear approximation P_{lin} could be the most useful in practical cases.

In the original proposal circular holes were foreseen; P has the same behaviour (L_α doesn't change), but its value is scaled by

$$\frac{(\tilde{\alpha_m}+\tilde{\alpha_e})^2_{circ}}{(\tilde{\alpha_m}+\tilde{\alpha_e})^2_{round}}\,\frac{N^2_{circ}}{N^2_{round}} \simeq 13, \tag{1.67}$$

if we assume the radius of the holes $R = W/2$, the nominal values for L, W, and T and if we put $C_M = C_E = 1$ both for rounded-end and circular holes. N_{round} (N_{circ}) are the number of rounded-end (circular) holes covering 4.4% of the beam screen surface. The value estimated in this way agrees with the previous estimate [2].

In Table 1.2 we report some values for two different (and relevant) device lengths: the first is the dipole length (14 m) while the second is $L_d \gg L_\alpha$ (i.e. the limiting value P_∞). The critical parameters are the thickness of the screen and the width of the slots W as well as their shapes: small changes on them imply large changes on the final value of P.

It is worth noting that the specific power given by Eq. (1.47) is dissipated in the coaxial because of the ohmic losses in the walls. It will be dissipated partly on the inner wall and partly on the outer one. The cold bore heating depends only on the power dissipated in the outer wall; assuming the same conductivity for both walls, we should then scale the previous result by the geometric factor $b_2/(b_2 + d) \simeq 45\%$, as stated in [7].

1.8 Conclusions

Analytical formulae are given for coupling impedance, loss factor and power lost per unit length for many holes in a coaxial liner and in presence of attenuation in the coaxial region.

	Rounded-end slots		Circular holes	
	@ Dipole	P_∞	@ Dipole	P_∞
$W = 1.5\,\mathrm{mm},\ L = 8.0\,\mathrm{mm},\ T = 1.0\,\mathrm{mm}$	0.19	1.1	2.49	14.5
$\boldsymbol{W} = 2.0\,\mathrm{mm},\ L = 8.0\,\mathrm{mm},\ T = 1.0\,\mathrm{mm}$	1.65	9.5	13.2	76.9
$\boldsymbol{W} = 3.0\,\mathrm{mm},\ L = 8.0\,\mathrm{mm},\ T = 1.0\,\mathrm{mm}$	22.3	129.6	85.6	497.1
$W = 1.5\,\mathrm{mm},\ L = 8.0\,\mathrm{mm},\ \boldsymbol{T} = 0.5\,\mathrm{mm}$	1.22	7.0	21.4	124.3

Table 1.2: Power lost per unit length (mW/m) in the LHC case for different length and different hole shapes, using P_{lin} and P_∞ ($C_M = C_E = 1$). The **bolded** letters stress the changed value in each row with respect to the first row (nominal values).

These results confirm and generalise previous ones; they are also helpful to understand the most relevant physical parameters in the design of the LHC beam screen.

Interference effects between the holes (not always considered in the literature) are mainly responsible for the beam energy loss. The attenuation in the coaxial region (at least the ohmic one in LHC) reduces them, but only over long distances (we find $\simeq$ 80 m for the LHC).

The coupling impedance for equally spaced holes is parabolic in frequency with superimposed interference peaks that are sharp and high. Those are nevertheless out of the bunch spectrum in the LHC and are also reduced by the foreseen randomisation: they don't seem to be dangerous for beam stability.

The power per unit length dissipated in the cold bore ($\leq$ 1.1 mW/m for nominal parameters) is not affected by the randomisation of the position of the holes. It depends strongly on the shape and dimensions of the holes. In particular the critical parameters are the width of the hole W and the wall thickness T: increasing the first or decreasing the second has to be done carefully to avoid too much power flowing in the coaxial region and heating the cold bore. The fraction of this power dissipated in the beam screen is less important since it has to be added to other sources of heating, for instance the incoherent synchrotron radiation (estimated [2] around 206 mW/m), that impose more serious limits. Moreover many devices will be installed outside the beam pipe; they will interrupt the ideal coaxial geometry to lengths shorter than L_α where the losses are linear with the device length and are remarkably smaller (0.19 mW/m for a dipole length).

Chapter 2

Wakefields due to surface waves in a beam pipe with periodic rough surface

2.1 Introduction

The effect of surface roughness is a relatively new subject, of interest in the design of machines with extremely short bunches of the order of tens of microns. In this case, in fact, the surface roughness may be a source of wakefields which might significantly increase the beam emittance and the energy spread. Recently, a corrugation of the LHC beam pipe has been proposed at CERN in order to reduce the reflectivity of the walls, and therefore decrease the heat load on the cold dipole beam screen due to photoelectrons accelerated by the proton beam [3].

The low frequency coupling impedance due to the wall surface roughness has been estimated in Ref. [25]. A different approach, using a small angle approximation in the wall profile, has been developed and gives estimations of the coupling impedance based on the statistical properties of the surface (see for example [26]). A dielectric layer model has also been proposed [27]: the roughness is replaced by a thin dielectric layer at the waveguide walls, which supports a surface wave. The synchronous mode resulting from the interaction of a particle beam and a corrugated waveguide has been already studied in the framework of the synchronous wave pick-up proposed in [28].

In this chapter we review the problem of the wakefields produced by an ultrarelativistic charge travelling inside a beam tube with a periodic corrugation, making use of a standard theory based on the hybrid modes propagating in the waveguide. We first derive the dispersion relation for the fields and study the frequency where a synchronous wave can be excited. Then, through the reciprocity principle we get the amplitude of the fields excited by the charge. Finally we apply our results to the case of the LHC beam screen and of the LCLS undulator [29].

2.2 The Method

Let us consider the periodically corrugated rectangular waveguide sketched in Figs. 2.1–2.2, a being the dimension of the corrugated side (x-axis) and b the distance (along the y-axis) between the corrugations on the opposite faces. We model the wall roughness as a series of periodic (with period L) rectangular obstacles of height h and thickness t. The beam travels along the z-axis; we assume $t \ll L$ and $L \ll \lambda$, where λ is the wavelength of the electro-magnetic fields. We neglect ohmic losses in the material.

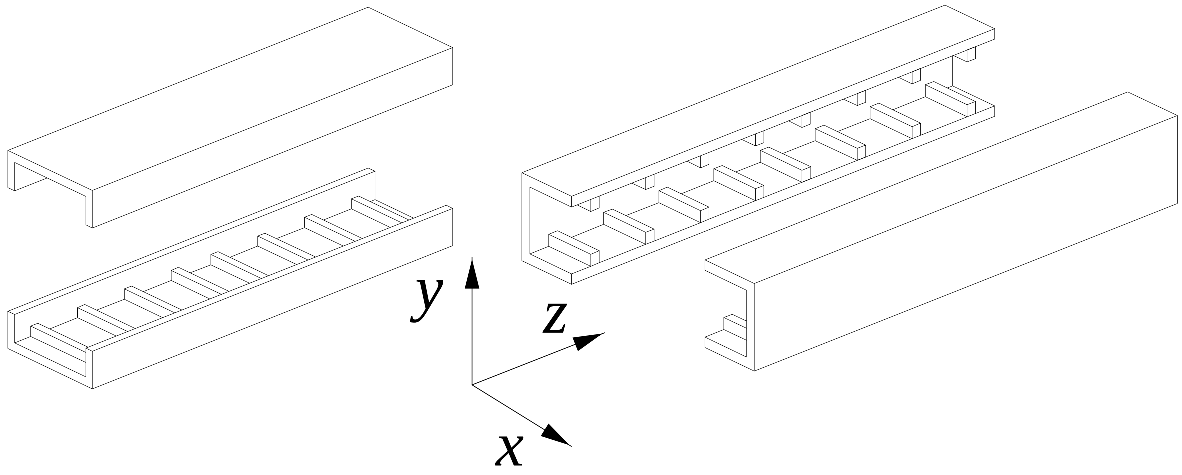

Figure 2.1: Relevant geometry.

Following [30], we consider a rectangular pipe with corrugations at only two opposite sides. The periodicity of the geometry along z allows the use of Floquet's theorem which implies a field solution independent of the period L (obtained from a single cell). For reader's convenience, we first apply the method to the case of a charge travelling on-axis (longitudinal problem); the solution for the transverse case (off-axis charge) is given in [31]. In order to find the longitudinal wake function per unit length [14], we go through the following steps. We first solve the homogeneous problem, thus finding the modes propagating in the corrugated waveguide (Sec. 2.3), then we apply the reciprocity principle including the sources (Sec. 2.4).

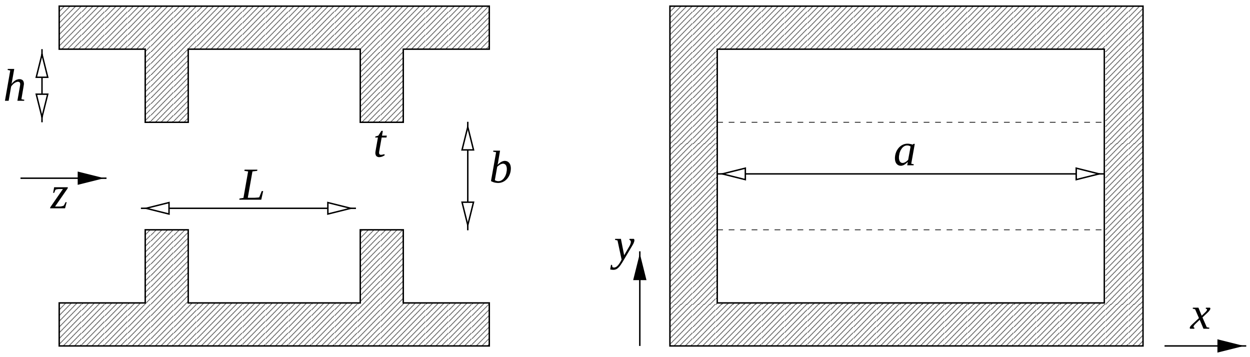

Figure 2.2: Schematic view of the waveguide and notations adopted.

Finally, we calculate the coupling impedance and wake function (Sec. 2.5). Throughout the chapter, we use (ξ_x, ξ_y, ξ_z) for the wave numbers of the field in a rough waveguide, (k_x, k_y, k_z) for a smooth waveguide, and (K_x, K_y) for the propagation inside the corrugation, that is in the region where $|y| > b/2$.

2.3 Homogeneous problem (on-axis charge)

Since we have assumed $L \ll \lambda$, the fields inside the corrugation do not depend on the z variable and, due to the rectangular geometry, they can be written as

$$E_z^c = -j\omega\mu_0 \sum_n B_n \sin\left[K_{yn}\left(b/2 + h - |y|\right)\right] \cos\left(K_{xn}x\right), \tag{2.1a}$$

$$E_y^c = 0, \tag{2.1b}$$

$$H_z^c = 0, \tag{2.1c}$$

$$H_y^c = \frac{\pi}{a} \sum_n nB_n \sin\left[K_{yn}\left(b/2 + h - |y|\right)\right] \sin\left(K_{xn}x\right), \tag{2.1d}$$

$$H_x^c = -K_{yn} \sum_n B_n \cos\left[K_{yn}\left(b/2 + h - |y|\right)\right] \cos\left(K_{xn}x\right), \tag{2.1e}$$

where B_n is the field amplitude (depending on the sources),

$$K_{yn} = \sqrt{\left(\omega/c\right)^2 - K_{xn}^2} \quad \text{and} \quad K_{xn} = k_{xn} = n\pi/a, \quad \text{with} \quad n = 1, 3, 5, \ldots. \tag{2.2}$$

Such fields satisfy the boundary condition $E_z^c = 0$ at $x = \pm a/2$ and $y = \pm(b/2 + h)$. The fields of interest in the internal region of the waveguide can be derived from the magnetic

Hertzian potential $\mathbf{\Pi} = \hat{\boldsymbol{x}}\Pi_x$ alone:

$$\boldsymbol{E} = -j\omega\mu_0 \nabla \times \mathbf{\Pi}, \tag{2.3a}$$

$$\boldsymbol{H} = (k^2 + \nabla\nabla\cdot)\mathbf{\Pi}. \tag{2.3b}$$

As shown in Appendix B.1, depending on the symmetry there are four possible expressions for Π_x, namely Π_{xi} with $i = 1, \ldots, 4$. In our case, with the charge travelling along the z-axis, only Π_{xi} corresponding to $i = 2$ has to be considered; it gives a non vanishing E_z on the beam axis. A y-directed magnetic Hertzian potential is excluded in our analysis since it would produce an E_x vanishing on the corrugation, because of continuity over the boundary, as in a smooth conducting rectangular waveguide. Again for continuity reasons K_x does not change going from the corrugation to the waveguide: $\xi_x = K_{xn} = k_{xn}$. Eventually we can write:

$$k_{xn}^2 + \xi_y^2 + \xi_z^2 = (\omega/c)^2 . \tag{2.4}$$

The field is continuous over the boundary, i.e.

$$E_z^c = E_z \quad \text{and} \quad H_x^c = H_x \quad \text{for} \quad y = \pm b/2 \tag{2.5}$$

and thus (considering only fields derived from Π_{x2})

$$K_{yn} \tan(K_{yn}h) = \xi_y \cot(\xi_y b/2) . \tag{2.6}$$

Equation (2.6) is usually referred to as dispersion relation; for each value of K_{yn}, it has an infinite number of solutions.

In the limit of a smooth waveguide ($h \to 0$), E_z^c and H_x^c vanish in Eqs. (2.5) and we recover the well-known condition $\xi_y = k_y = m\pi/b$, with $m = 1, 3, 5, \ldots$.

For finite values of h, solving numerically Eq. (2.6) and plugging the resulting value for ξ_y in Eq. (2.4), we get the wave number ξ_z. A convenient graphical representation for the propagation behaviour of these waves is the Brillouin diagram; to show the basic features of the solution, we study the case of a square waveguide of side a and plot the normalised wave number $\xi_z a$ as a function of the normalised frequency a/λ in Fig. 2.3. The dispersion curve of a smooth waveguide (dashed line) at very high frequencies tends asymptotically to

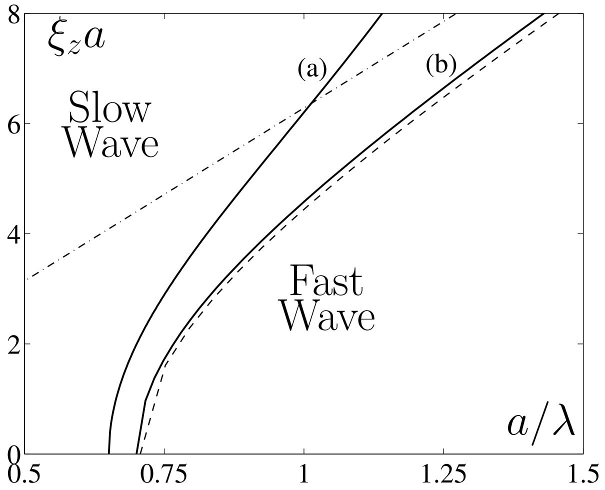

Figure 2.3: Dispersion diagram for a square waveguide of side a with corrugation on two opposite sides. The solid lines are obtained from Eq. (2.6): line (a) is for $h/a = 0.1$, while line (b) is for $h/a = 0.01$. The dashed line corresponds to the unperturbed TM_{11} mode of the smooth waveguide and the dot-dashed line represents an ultrarelativistic beam.

the wave number of an ultrarelativistic beam $\omega/c = 2\pi/\lambda$ (dot-dashed line), but it never crosses it. However, due to the corrugation, there may be a crossing of the dispersion curves at particular frequencies where the waveguide mode and the beam are synchronous (that is $\xi_z = \omega/c$) and a coherent exchange of energy is possible. These crossing frequencies depend on the depth of the corrugation h. When $\xi_z = \omega/c$, from Eq. (2.4)

$$\xi_y^2 = -k_{xn}^2 \quad \Rightarrow \quad \xi_y = jk_{xn}; \tag{2.7}$$

if h is small with respect to λ and to the waveguide dimension a, we may also write

$$K_{yn} \tan(K_{yn}h) \approx K_{yn}^2 h. \tag{2.8}$$

Then using the definition of K_{yn} (Eq. (2.2)), we rewrite the dispersion relation Eq. (2.6) as

$$\left(\frac{2\pi \overline{f_n}}{c}\right)^2 - k_{xn}^2 = \frac{k_{xn}}{h} \coth\left(\frac{b}{2}k_{xn}\right), \tag{2.9}$$

thus obtaining the crossing frequencies

$$\overline{f_n} = \frac{c}{2\pi}\sqrt{k_{xn}^2 + \frac{k_{xn}}{h}\coth\left(k_{xn}\frac{b}{2}\right)}. \tag{2.10}$$

For very small h, the second term in the square root dominates, resulting in a behaviour $\overline{f_n} \propto 1/\sqrt{h}$, analogous to the case of a pipe covered with a dielectric layer of thickness h [27].

The modes propagating in the corrugated waveguide are called hybrid modes [30], since they can be derived by a superposition of the standard TE and TM modes (along the z-axis). The hybrid modes in general do not satisfy an orthogonality condition; physically this means that they are coupled to each other. Since the coupling coefficients are proportional to the height of the corrugation h, for very small corrugation depths the modes are practically decoupled.

The minimum frequency beyond which a mode can propagate in the guide (namely its cut-off frequency f_c) depends on the corrugation depth as well. Mathematically the cut-off frequency is found by imposing the condition $\xi_z = 0$, which implies $\xi_y = \sqrt{(\omega/c)^2 - k_{xn}^2} = K_{yn}$ (from Eq. (2.4)). The dispersion relation becomes

$$K_{yn} \tan\left(K_{yn} h\right) = K_{yn} \cot\left(K_{yn} b/2\right) \quad \text{that is} \quad \cos\left(K_{yn} \frac{2h+b}{2}\right) = 0. \tag{2.11}$$

Solving for K_{yn} and using Eq. (2.2), it is straightforward to get

$$f_c = \frac{c}{2\pi}\sqrt{\left(\frac{n\pi}{a}\right)^2 + \left(\frac{m\pi}{2h+b}\right)^2} \quad \text{with} \quad n = 1, 3, 5, \ldots \quad \text{and} \quad m = 1, 3, 5, \ldots. \tag{2.12}$$

For frequencies higher than cut-off, the solution of Eq. (2.6) combined with Eq. (2.4) gives real values for ξ_z, while ξ_z is purely imaginary for lower frequencies. In the limit of $h \to 0$, we find the well-known cut-off frequencies for the modes of a smooth waveguide. Equation (2.12) concerns only the modes obtainable from Π_{x2}.

Moreover, for small h we can write a formula for ξ_z as a function of the wave number k_z of the smooth waveguide (see Appendix B.2):

$$\xi_z \approx k_z + \frac{2K_{yn}}{k_z b} \tan\left(K_{yn} h\right). \tag{2.13}$$

Since k_z and K_{yn} are both depending on the frequency f, it is non trivial to get Eq. (2.10) directly from Eq. (2.13).

If the wave number of our hybrid mode falls in the region below (above) the dot-dashed line in Fig. 2.3, the wave is usually referred to as fast (slow) because its phase velocity is larger (smaller) than the speed of light. Moreover, for a rough waveguide ξ_z can exceed the wave number of the smooth one, meaning that the solution ξ_y of Eqs. (2.6) is purely imaginary (see Eq. (2.4)). In that case the wave is said to be a surface wave, because it is exponentially damped in the y-direction.

2.4 Including the sources

Having solved the homogeneous problem, i.e. having derived the modes of the structure, the field generated by a point charge can be found by means of the Lorentz reciprocity principle [17]. Referring to Appendix B.3, we may write

$$-\sum_m b_m e^{-j(\xi_{zn}-\xi_{zm})z} A_{nm} + \sum_m a_m e^{-j(\xi_{zn}+\xi_{zm})z} B_{nm} = \int_V \boldsymbol{J} \cdot \boldsymbol{E}_n^+ \, dV, \tag{2.14a}$$

$$-\sum_m a_m e^{-j(\xi_{zn}-\xi_{zm})z} A_{nm} - \sum_m b_m e^{-j(\xi_{zn}+\xi_{zm})z} B_{nm} = \int_V \boldsymbol{J} \cdot \boldsymbol{E}_n^- \, dV, \tag{2.14b}$$

where $\boldsymbol{J}$ is the spectral current density of a point charge travelling on-axis ($\hat{z}_o$ unit vector along the z-axis),

$$\boldsymbol{J}(x, y, z; \omega) = q\,\delta(x)\delta(y)e^{-jz\omega/\beta c}\hat{z}_o; \tag{2.15}$$

a_n (b_n) is the coefficient of the expansion of the field using the forward (backward) propagating modes of the structure $\boldsymbol{E}_n^+, \boldsymbol{H}_n^+$ $\left(\boldsymbol{E}_n^-, \boldsymbol{H}_n^-\right)$. Denoting by S_c the cross section of the guide,

$$A_{nm} = \int_{S_c} (\boldsymbol{e}_{tn} \times \boldsymbol{h}_{tm} + \boldsymbol{e}_{tm} \times \boldsymbol{h}_{tn}) \cdot \hat{z}_o \, dS_c, \tag{2.16a}$$

$$B_{nm} = \int_{S_c} (\boldsymbol{e}_{tn} \times \boldsymbol{h}_{tm} - \boldsymbol{e}_{tm} \times \boldsymbol{h}_{tn}) \cdot \hat{z}_o \, dS_c, \tag{2.16b}$$

where $\boldsymbol{e}_t$ and $\boldsymbol{h}_t$ are the transverse modal function, i.e. the transverse behaviour of the mode field. For instance in a smooth waveguide, where the modes are orthogonal, it holds

$$A_{nm} = 2\delta_{nm} \quad \text{and} \quad B_{nm} = 0, \tag{2.17}$$

resulting in well known relations for a_n, b_n [17] (δ_{nm} stands for the Kronecker's symbol).

In a rough waveguide the (hybrid) modes are no longer orthogonal. Nevertheless only the mode synchronous with the beam can exchange energy over an infinite interaction length [14] (*surfing effect*), thus we may treat modes one by one; moreover the coupling itself goes to zero in the limit $h \to 0$ that we are presently interested in. In this case Eqs. (2.14) become

$$a_n A_{nn} = -\int_V \boldsymbol{J} \cdot \boldsymbol{E}_n^- \, dV \qquad \text{and} \qquad b_n A_{nn} = -\int_V \boldsymbol{J} \cdot \boldsymbol{E}_n^+ \, dV. \tag{2.18}$$

Since, as shown in Appendix B.3.1,

$$A_{nn} = \omega\mu_0 \left|\xi_{zn}\right| \left(k^2 - k_{xn}^2\right) a \, \left[\frac{b}{2} - \frac{\sin(\xi_y b)}{2\xi_y}\right] \tag{2.19}$$

and

$$\int_V \boldsymbol{J} \cdot \boldsymbol{E}_n^{\pm} \, dV = \pm jq\omega\mu_0 \xi_y 2\pi\delta\left(\frac{\omega}{\beta c} \pm \xi_{zn}\right), \tag{2.20}$$

the electric field has a resonant behaviour around the crossing frequencies:

$$\begin{aligned} E_z\left(x, y, z; \omega\right) = -2\pi \, \beta \, & \frac{qZ_0 \left[\delta\left(\frac{\omega}{\beta c} - \xi_{zn}\right) + \delta\left(\frac{\omega}{\beta c} + \xi_{zn}\right)\right]}{a\left[b/2 \; - \; \sin(\xi_y b)/2\xi_y\right]} \times \\ & \frac{\xi_y^2}{k^2 - k_{xn}^2} \cos\left(k_{xn}x\right) \cos\left(\xi_y y\right) e^{-jz\omega/\beta c}, \end{aligned} \tag{2.21}$$

where δ is the Dirac delta-function, c is the light velocity in vacuum, $k = \omega/c$, β is the relativistic factor, Z_0 is the free-space characteristic impedance and ξ_y is obtained by solving Eq. (2.6). The field is non null only at the crossing frequencies $\bar{f}$ given by Eq. (2.10), i.e. those such that $\xi_z = \omega/\beta c$. It is worth noting that all the frequency dependent quantities in Eq. (2.21), i.e. ξ_y and k, have now to be computed at the crossing frequency because of the Dirac functions; thus we may simplify Eq. (2.21) since for $h \ll \lambda$ and from Eq. (2.6):

$$\frac{\xi_y^2}{k^2 - k_{xn}^2} = -\frac{k_{xn}\, h}{\coth\left(k_{xn} b/2\right)}. \tag{2.22}$$

The synchronism between the field in the waveguide and the beam is possible because of the slowing effect due to the surface roughness.

For ultrarelativistic particles ($\beta = 1$) and small h ($h \ll \lambda$), the electric field at the lowest frequency ($n = 1$) is

$$\begin{aligned} E_z\left(x, y, z; \omega\right) \sim -4\pi^2 \, q \, Z_0 \, \frac{h}{a} \, \frac{1}{ab} \, & \left\{\coth\left(\frac{\pi}{2}\frac{b}{a}\right)\left[\frac{\sinh\left(\pi b/a\right)}{\pi b/a} - 1\right]\right\}^{-1} \times \\ \cos\left(\frac{\pi}{a}x\right) \, \cosh\left(\frac{\pi}{a}y\right) \, & e^{-jz\omega/c}\left[\delta\left(\omega/c \; - \; \xi_{z1}\right) + \delta\left(\omega/c \; + \; \xi_{z1}\right)\right], \end{aligned} \tag{2.23}$$

providing that Eq. (2.7) holds for ξ_y at the crossing frequency. First of all, E_z has a phase difference of π relative to the charge field (the minus sign), meaning that it is a decelerating field. The field is confined in the waveguide region near the corrugated wall (it is exponentially growing for $y \to \pm b/2$), as we expect for a surface wave. The height of the corrugation fixes not only the resonant frequency through ξ_{z1}, but also the field amplitude through to the factor h/a: the field decreases in amplitude and increases in frequency as h decreases.

A structure of finite length ℓ will result in a spread of frequencies that can be excited, since

$$2\pi\delta\left(\omega/\beta c\ \pm\ \xi_{zn}\right) \longrightarrow \ell\frac{\sin\left[\left(\omega/\beta c\ \pm\ \xi_{zn}\right)\ell/2\right]}{\left(\omega/\beta c\ \pm\ \xi_{zn}\right)\ell/2}. \tag{2.24}$$

2.5 Longitudinal coupling impedance and wake function

Following the standard definition of the (specific) longitudinal coupling impedance [14]

$$\frac{\partial Z(\omega)}{\partial z} = -\frac{1}{q}E_z\left(x=0, y=0, z, \omega\right)e^{jz\omega/c}, \tag{2.25}$$

from Eq. (2.23) we get the (real) coupling impedance due to the surface wave:

$$\begin{aligned}\frac{\partial Z\left(\omega\right)}{\partial z} =& 4\pi^2\ Z_0\ \frac{h}{a}\ \frac{1}{ab}\ \left\{\coth\left(\frac{\pi}{2}\frac{b}{a}\right)\left[\frac{\sinh\left(\pi b/a\right)}{\pi b/a}-1\right]\right\}^{-1}\times \\ &\left[\delta\left(\omega/c\ -\ \xi_{z1}\right)+\delta\left(\omega/c\ +\ \xi_{z1}\right)\right].\end{aligned} \tag{2.26}$$

It is straightforward now to get the wake function for unit length and for a point charge [14], i.e.

$$\frac{\partial w(\tau)}{\partial z} = \frac{H(\tau)}{\pi}\int_{-\infty}^{\infty}\frac{\partial Z(\omega)}{\partial z}e^{j\omega\tau}d\omega, \tag{2.27}$$

where τ is the time distance of the trailing charge from the leading one and $H(\tau)$ is the Heaveside function. Eventually we get

$$\frac{\partial w(\tau)}{\partial z} = w_0\left(a,b,h\right)\cos\left(2\pi\overline{f_1}\,\tau\right)H(\tau), \tag{2.28}$$

where

$$w_0\left(a,b,h\right) = 8\pi\frac{Z_0\ c}{ab}\ \frac{h}{a}\ \left\{\coth\left(\frac{\pi}{2}\frac{b}{a}\right)\left[\frac{\sinh\left(\pi b/a\right)}{\pi b/a}-1\right]\right\}^{-1}. \tag{2.29}$$

To get the wake function for a bunch, one has to perform the convolution of Eq. (2.28) with the bunch spectrum. For instance, the wake function is

$$\frac{\partial W(\tau)}{\partial z} = w_0\left(a,b,h\right)\ \int_0^{\infty}\frac{e^{-(t-\tau)^2/2\sigma^2}}{\sqrt{2\pi}\sigma}\cos\left(2\pi\overline{f_1}\,t\right)\ dt \tag{2.30}$$

for a gaussian bunch of r.m.s bunch length σ and this integral has to be performed numerically.

2.5.1 Application to the LHC beam screen

The amplitude $w_0\,(a, b, h)$ of the sinusoidal wake function for an LHC-like geometry[1] ($a = 3.6 \times 10^{-2}$ m, $b = 4.3 \times 10^{-2}$ m and $h = 30$ μm) is $\simeq 0.3\ V\ pC^{-1}\ m^{-1}$ and the first crossing frequency $\overline{f_1}$ is 83 GHz (and $h \ll \lambda$, as assumed). Since the r.m.s. bunch length is $\sigma \approx 7.5$ cm, the bunch cut-off frequency $c/(2\pi\sigma)$ is of the order of 1 GHz, i.e. nearly a factor a hundred lower than the wake resonant frequency (that is the crossing frequency).

Until now we have shown that the wakefield due to the synchronous mode has a resonant behaviour and the quality factor Q of such a resonance is infinite, since we have assumed an infinite interaction length, no ohmic losses and an ideal geometry. This is clearly an approximation and, to estimate the threshold of the longitudinal instability, we will consider the standard resonator model [33] with a shunt resistance R_s given by

$$R_s = \frac{Q w_0 L_0}{2\pi \overline{f_1}} = 1.6 \times 10^4 Q \quad \Omega \tag{2.31}$$

with a finite Q value. The LHC parameters we will use are given in Table I.

momentum compaction (10^{-4})	α_c	3.47	
machine length (km)	L_o	26.66	
revolution frequency (kHz)	f_o	11	
energy (GeV)	E_o	7 10^3 (top)	450 (inj.)
bunch length (mm)	σ	75 (top)	130 (inj.)
energy spread (10^{-4})	$\sigma_{\varepsilon o}$	1.1 (top)	4.7 (inj.)

Table 2.1: LHC parameter list for two operating conditions, namely at top energy (top) and at injection energy (inj.).

The impedance at frequencies well below the resonator frequency (for example at the frequency $f_{bunch} = c/2\pi\sigma$ associated with the bunch length) is inductive and such that

$$|Z/n| \approx \frac{R_s}{Q} \frac{f_o}{\overline{f_1}} \approx 2 \text{ m}\Omega, \tag{2.32}$$

i.e. two orders of magnitude smaller than the LHC impedance budget (n is the harmonic number $n = f/f_o$). At the resonator frequency $\overline{f_1}$, the impedance $|Z/n|$ is real and equal to that of Eq. (2.32) multiplied by the Q factor.

[1] In the LHC the corrugations are on the vertical, shorter sides.

An estimate of the longitudinal instability threshold (for mode numbers of the order of $\overline{f_1}/f_{bunch} = 130$) can be done by using the Boussard criterion [32], derived from the coasting beam theory, which we write here in the form

$$N_{th} = \frac{(2\pi)^{(3/2)}\,(E_0/e)\ \alpha_c\ \sigma\ \sigma_{\varepsilon 0}^2}{c\ e\ \ |Z/n|}, \tag{2.33}$$

with E_0 the nominal energy, e the electron charge, α_c the momentum compaction, $\sigma_{\varepsilon 0}$ the energy spread, and Z the coupling impedance at a frequency corresponding to harmonic number n. For the top energy of 7 TeV we get

$$N_{th} = \frac{7.22 \times 10^{11}}{\left|\frac{Z/n}{\Omega}\right|} \tag{2.34}$$

protons per bunch, while in the case of injection energy (450 GeV) the threshold is a factor 2 higher.

In the most pessimistic case in which the perturbation of the unstable oscillation mode has the same resonant frequency $\overline{f_1}$ of the wake, we obtain a threshold of

$$N_{th} = \frac{3.67 \times 10^{14}}{Q} \tag{2.35}$$

protons per bunch, depending on the value of Q. Quality factors Q higher than 2×10^3 (equivalent to effective interaction lengths longer than 6 m) are therefore dangerous for the LHC, whose ultimate intensity is 1.6×10^{11} protons per bunch.

On one hand, a more accurate stability analysis including azimuthal [33] and radial [34] mode coupling would then be in order. On the other hand several mechanisms, not included in the previous derivation, will limit the quality factor Q, including ohmic losses and geometric imperfections. In particular, pumping slots in the LHC beam screen induce mixing of the modes propagating in the beam pipe and attenuation of the synchronous surface wave, presumably after a distance of a few meters [35].

2.5.2 Application to the LCLS undulator

The longitudinal wake discussed so far is relevant also for very short bunches; an interesting example is the LCLS undulator [29], where the expected bunch is short (the r.m.s. bunch length is $\sigma = 15\ \mu$m) and rather rectangular in shape. For a rectangular charge distribution, with half width $T = \sqrt{3}\sigma/c$, the r.m.s energy spread (over the whole machine) is simply given by [36]:

$$\frac{\Delta E^{rms}}{E} = \frac{Nq\, L_c\, w_0(a,b,h)}{2E}\sqrt{\frac{1}{2\,(\omega_1 T)^2}\left[1 - \frac{\sin\,(4\omega_1 T)}{4\omega_1 T}\right] - \left[\frac{\sin\,(\omega_1 T)}{\omega_1 T}\right]^4}, \tag{2.36}$$

where E is the energy, L_c the length of the machine, Nq is the bunch charge and $\omega_1 = 2\pi\overline{f_1}$. Figure 2.4 shows the result for a geometry similar to the LCLS undulator (the circular beam pipe of radius $r = 2.5$ mm is approximated by a square one with a side of $a = 4$ mm). Thus,

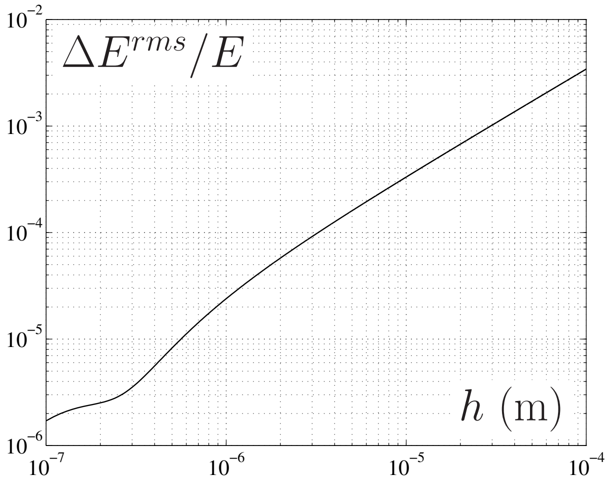

Figure 2.4: Energy spread for a geometry approximating the LCLS undulator as a function of the depth of the corrugation ($a = b = 4$ mm, $L_c = 112$ m, $Nq = 1$ nC, $E = 14.3$ GeV, $\sigma = 15$ μm).

concerning the effect of a synchronous mode, the requirement of having a relative energy spread increase smaller than 5×10^{-4} is satisfied if the beam pipe roughness is kept below 10 μm.

2.6 Conclusions

In this chapter we have derived the longitudinal wakes due to a periodic corrugation in a rectangular beam pipe. For a point charge, the amplitude of the sinusoidal wake function is proportional to the corrugation depth h and the oscillation frequency is proportional to $1/\sqrt{h}$. For $h \to 0$ the frequency of the wake function goes to infinity, while its amplitude vanishes. This last result disagrees from the one obtained in [27] with a dielectric layer model, where the amplitude of the wake does not depend on the corrugation depth.

Application of our results to the case of the LHC beam screen indicates that the Q-factor of the synchronous surface wave should not exceed 2000 to ensure longitudinal beam stability. In the case of the LCLS undulator a beam pipe roughness below 10 μm is acceptable.

Chapter 3

Azimuthally inhomogeneous pipe

3.1 Motivation and goals

The LHC beam pipe has a longitudinal welding strip all along its length and its effect on the power loss has to be estimated. This strip (which is about 1/60th of the entire pipe circumference) is made of a conductor whose conductivity can be well approximated by the stainless steel one. Therefore the beam will "see" an azimuthally inhomogeneous pipe made for the greatest part by copper but with an azimuthally small piece of stainless steel (whose conductivity is roughly sixty times worse than the copper one at room temperature).

The distribution of the image currents is important to estimate the beam-wall interaction. In fact if the currents would avoid the badly conducting region and would flow mainly in the copper layer, the beam would practically not "see" any difference between the real beam pipe and a copper one. For resistors in parallel this is the case: the currents somehow choose the less "dissipative" path and the resistors with lower resistivity carry the highest current (according to Ohm's law). On the contrary, if the image currents are constant over the azimuth, i.e. if the same amount of current flows in the copper and in the stainless steel, then the beam would dissipate a considerable power due to the weldings.

To answer this question we consider a single particle travelling on axis in an infinitely long cylindrical beam pipe, whose conductivity is varying with the azimuth. The relevant range of conductivity values is between the copper one and the stainless steel one, both at room and at cryogenic temperature (approximately 20 K for the LHC beam screen). We seek for an analytical (or semi-analytical) solution for the field excited by an ultrarelativistic charge in such a structure in order to get the current distribution on the boundary surface.

The fields inside the pipe can be derived from magnetic and electric Hertzian potentials (Sec. 3.2), whose amplitudes depend on the driving term (the charge field) and on the boundary conditions. Since the pipe is metallic, some simplified boundary conditions can be assumed. They are discussed in Sec. 3.3 and first applied to known (simple) cases, to check their validity (Sec. 3.4). Such approximate conditions drastically simplify the problem which is reduced to the solution of a linear system of equations for the coefficients of a multipole expansion of the Hertzian potentials (Sec. 3.5). The system is truncated to a given order and recurrence relations are found for the quantities needed to express the fields everywhere inside the beam pipe, as done in Secs. 3.6–3.7. The longitudinal and azimuthal currents are proportional, respectively, to the azimuthal and longitudinal magnetic field on the boundary and their behaviour is discussed in Sec. 3.8 and compared in Sec. 3.9 to more simplified approaches. To asses validity of the results, comparisons with numerical simulations (HFSS) and with bench measurements are discussed in Secs. 3.10–3.11. Implications for the LHC are briefly discussed in Sec. 3.13.

3.2 Green's function approach: Hertzian potentials in a perfectly conducting circular waveguide

The Green's function method has been successfully applied to study the coupling impedance of discontinuities in perfectly conducting cylindrical beam pipes, either for a charge travelling on-axis [37] or travelling off-axis [38]; a review can be found in [39]. The fields are expressed (through the Hertzian potentials) as a function of the currents on the perfect conductor; by imposing the boundary conditions, they find a set of integral equations which can be solved using a Wiener-Hopf technique [40], getting eventually the longitudinal and transverse coupling impedance. In the following, we will assume that the fields inside the pipe can be expanded as in [38]; these fields satisfy the boundary conditions on the conductor of finite conductivity σ, as discussed in Sec. 3.3.

We consider only time harmonic electromagnetic fields with a time dependence specified by the complex factor $\exp(-j\omega t)$, which is omitted. In a stationary, linear, isotropic, homogeneous medium which is free of sources, Maxwell's equations for the field can be written

$$\nabla \times \boldsymbol{E} = jkZ\boldsymbol{H} \quad \text{and} \quad \nabla \times \boldsymbol{H} = -jkY\boldsymbol{E}, \tag{3.1}$$

where $\boldsymbol{E}, \boldsymbol{H}$ are the complex phasors representing the electric and magnetic fields, respectively, $Z = 1/Y = \sqrt{\mu/\varepsilon}$ is the intrinsic impedance of the medium and $k = \omega\sqrt{\mu\varepsilon}$ is the propagation constant or wave number. The permittivity and permeability of the medium ε and μ may be complex, thus incorporating the effect of losses. In the particular case of a vacuum, $Z = Z_0 = 120\pi\ \Omega$, and we distinguish the corresponding parameters by the suffix "0". SI units are used throughout. Maxwell's equations are invariant under the *duality* transformation

$$\boldsymbol{E} \to \boldsymbol{H}, \quad \boldsymbol{H} \to -\boldsymbol{E}, \quad \varepsilon \leftrightarrow \mu, \quad Z \leftrightarrow Y. \tag{3.2}$$

The field can be expressed through the magnetic and electric Hertzian potentials $\boldsymbol{\Pi}$ and $\widetilde{\boldsymbol{\Pi}}$ as follows:

$$\boldsymbol{E} = (k^2 + \nabla\nabla\cdot)\boldsymbol{\Pi} - jkZ_0\nabla \times \widetilde{\boldsymbol{\Pi}}, \tag{3.3a}$$

$$\boldsymbol{H} = -j\frac{k}{Z_0}\nabla \times \boldsymbol{\Pi} - (k^2 + \nabla\nabla\cdot)\widetilde{\boldsymbol{\Pi}}. \tag{3.3b}$$

The Hertzian potentials must be solutions of the wave equation; having applied the separation of variables

$$\frac{1}{r}\frac{\partial}{\partial r}\left(r\frac{\partial \boldsymbol{\Pi}}{\partial r}\right) + \frac{\partial^2 \boldsymbol{\Pi}}{\partial z^2} + \left(k^2 - \frac{m^2}{r^2}\right)\boldsymbol{\Pi} = 0; \tag{3.4}$$

furthermore $\boldsymbol{\Pi}$ and $\partial\widetilde{\boldsymbol{\Pi}}/\partial r$ must be continuous at the beam pipe radius $r = b$, as follows from the relation of these functions to the electromagnetic field. We therefore seek these functions in the form [40, 38]:

$$\Pi_z = \frac{Z_0}{4\pi k}\sum_{m=0}^{\infty}\cos(m\phi)\int_{-\infty}^{+\infty} F_m(\alpha)\left\{\begin{array}{l} J_m(\Omega r)\,H_m(\Omega b) \\ J_m(\Omega b)\,H_m(\Omega r) \end{array}\right\} e^{j\alpha z}\,d\alpha \quad \begin{array}{l} r < b \\ r > b \end{array}, \tag{3.5a}$$

$$\widetilde{\Pi}_z = \frac{1}{4\pi k}\sum_{m=1}^{\infty}\sin(m\phi)\int_{-\infty}^{+\infty} \frac{\widetilde{F}_m(\alpha)}{\Omega}\left\{\begin{array}{l} J_m(\Omega r)\,H'_m(\Omega b) \\ J'_m(\Omega b)\,H_m(\Omega r) \end{array}\right\} e^{j\alpha z}\,d\alpha \quad \begin{array}{l} r < b \\ r > b \end{array}, \tag{3.5b}$$

where J_m and $H_m = H_m^{(1)}$ are the Bessel and Hankel (first kind) functions of order m, $\Omega^2 = k^2 - \alpha^2$ and $F_m(\alpha)$, $\widetilde{F}_m(\alpha)$ are the unknown coefficients. To build the field only the

z-components of the potentials are needed. A more general expression for the Hertzian potentials, would be with $\exp(jm\phi)$ instead of sine and cosine. Let us define the function $G_m(\alpha; r, b)$ such that

$$G_m(\alpha; r, b) = \begin{cases} J_m(\Omega r) H_m(\Omega b) & r < b \\ J_m(\Omega b) H_m(\Omega r) & r > b \end{cases}, \tag{3.6}$$

which is continuous at $r = b$.

As it is clear from Appendix C.1, the physical justification of such Hertzian potentials is that the perfectly conducting boundary can be replaced by a sheet of currents radiating in the free space; the field can then be described as the sum of terms weighted by F_m and $\widetilde{F}_m$ (strictly related to the currents) which depend on the boundary conditions.

When the potentials (and the derived fields) are used in a perfectly conducting waveguide, they give the usual modes: the TE modes are derived from Π_z while the TM modes from $\widetilde{\Pi}_z$ (see Appendix C.1). In all the other boundary conditions, e.g. discontinuous perfectly conducting wall or continuous wall but with finite conductivity, the two potentials must be considered jointly.

The currents that can be excited by a single particle travelling with a phase velocity βc in an infinitely long structure are synchronous with the source and thus proportional to $\delta(\alpha - \omega/\beta c)$:

$$\left.\begin{array}{l} F_m(\alpha) = F_m \delta(\alpha - \omega/\beta c) \\ \widetilde{F}_m(\alpha) = \widetilde{F}_m \delta(\alpha - \omega/\beta c) \end{array}\right\} \Longrightarrow \Omega = j\frac{k}{\beta\gamma}.$$

Eventually, the potentials become

$$\Pi_z = -\frac{j}{2\pi^2}\frac{Z_0}{k}\sum_{m=0}^{\infty} F_m \left\{\begin{array}{l} I_m(kr/\beta\gamma) K_m(kb/\beta\gamma) \\ I_m(kb/\beta\gamma) K_m(kr/\beta\gamma) \end{array}\right\} \cos(m\phi) e^{jzk/\beta} \quad \begin{array}{l} r < b \\ r > b \end{array}, \tag{3.7a}$$

$$\widetilde{\Pi}_z = \frac{j}{2\pi^2}\frac{\beta\gamma}{k}\sum_{m=1}^{\infty} \widetilde{F}_m \left\{\begin{array}{l} I_m(kr/\beta\gamma) K'_m(kb/\beta\gamma) \\ I'_m(kb/\beta\gamma) K_m(kr/\beta\gamma) \end{array}\right\} \sin(m\phi) e^{jzk/\beta} \quad \begin{array}{l} r < b \\ r > b \end{array}. \tag{3.7b}$$

To obtain the fields reported in Appendix C.1, one simply needs to use Eqs. (3.3).

In the case of perfectly conducting walls, the surface (electric) current density $\boldsymbol{J}_S$ is equal to the discontinuity of the magnetic field at the boundary, i.e.

$$J_{Sz} = H_\phi(b^+) - H_\phi(b^-) = -\frac{1}{2\pi^2}\sum_{m=0}^{\infty}\left[\frac{F_m}{b} + \frac{m}{\beta}\left(\frac{\beta\gamma}{kb}\right)^2 \widetilde{F}_m\right] \cos(m\phi) e^{jzk/\beta}, \tag{3.8a}$$

$$J_{S\phi} = H_z(b^-) - H_z(b^+) = \frac{1}{2\pi^2}\sum_{m=1}^{\infty} j\frac{\widetilde{F}_m}{kb} \sin(m\phi) e^{jzk/\beta}, \tag{3.8b}$$

showing the strict relationship between F_m, $\widetilde{F}_m$ and the currents; $H_\phi(b^+)$ means $H_\phi(r \to b^+)$ and so on. In a non-perfect conductor, there are no surface currents, since the field is continuous over the boundary. Nevertheless, when using some approximate boundary condition (see Sec. 3.3), surface currents may "appear", but with an expression different from Eq. (3.8).

3.3 Approximate Boundary Conditions

Approximate boundary conditions provide a relationship between the electric and magnetic field on a chosen surface. In general their purpose is to simplify the analytical or numerical solution of wave problems involving complex structures. They are important in all disciplines, e.g. acoustics, hydrodynamics and electromagnetics, where boundary conditions are involved, and are becoming more so as we seek to model more complicated situations. Some versions have also been around for a long time and, although the classical condition $\boldsymbol{E}_{tan} = 0$ at the surface of a metal is often regarded as exact, it is in fact an approximation for all metals even at microwave frequencies.

In 1938–1939, approximate boundary conditions at the surface of a good conductor were suggested by M.A. Leontovitch [41] who actually published his results only in 1948 [42]. Since then the range of boundary value problems in electrodynamics involving the presence of good conductors has continued to increase, and Leontovich's boundary conditions have been widely used in high frequency physics and engineering. One of their first rigorous derivation was given by S.M. Rytov [43], who developed conditions valid through the second order (the order of a condition is specified by the highest derivative present in one manifestation of the condition) applicable at the curved surface of a highly conducting body.

The simplest approximate boundary conditions are the (standard) impedance boundary conditions applicable at the surface of a lossy dielectric; they came into use in the 1940's in connection with ground wave propagations over the Earth. More recently, due to increasing of demanding applications, improved or higher order versions of the impedance boundary conditions are being considered and they are usually referred to as "generalised impedance boundary conditions" (GIBCs). A comprehensive treatment in the framework of a generalised Rytov analysis is reported in [44] where applications and validity limits are also discussed.

For the time being, we will limit ourselves to first order boundary conditions and their limit of validity. For a homogeneous body whose boundary is a coordinate surface in a (generic) system of orthogonal curvilinear coordinates, Rytov showed that the tangential components of the electric field at the boundary could be expressed as power series in the (small) penetration depth δ, with coefficients which involve the tangential magnetic field components and their tangential derivatives. Taking the zeroth order of such expansion, it can be shown that (on the boundary)

$$\boldsymbol{n} \times \boldsymbol{E} = Z\,\boldsymbol{n} \times (\boldsymbol{n} \times \boldsymbol{H}) \quad \text{where} \quad Z = \sqrt{\frac{\mu}{\varepsilon}}. \tag{3.9}$$

where $\boldsymbol{n}$ is the outward unit vector normal to the surface; these relations (and their equivalent forms) are usually quoted as "Leontovitch boundary conditions"[1]. Equation (3.9) is an example of a first order boundary condition, sometimes referred to as an SIBC (Standard Impedance Boundary Condition).

It can be also shown [44] that Eq. (3.9) remains unaffected by any variation of ε and/or μ either laterally or in depth provided that these are slow on the scale of the local wavelength in the material. This is an important feature of Eq. (3.9). It explains, for example, its ability to model progressive changes in the material properties if the local value of Z is given at each point of the surface.

Usually, Eq. (3.9) is derived for a planar surface and then extended to a generic surface under the assumption that the minimum curvature radius is *not too small*. Establishing rigorously such validity limits is easy in the framework of the Rytov analysis [43]; a generalised version of the Rytov analysis (leading also to boundary conditions of any order) is reported in Appendix A of Ref. [44].

As we pointed out above, Eq. (3.9) results from the zeroth order of an expansion of the fields at the boundary in powers of the penetration depth. Taking the first order of such expansion, the boundary condition reads

$$\boldsymbol{n} \times \boldsymbol{E} = \overline{\overline{\eta}} \cdot \boldsymbol{n} \times (\boldsymbol{n} \times \boldsymbol{H}) \tag{3.10}$$

[1] In a footnote of [42], Leontovich indicated that the boundary condition was originally proposed by Schukin.

where $\overline{\overline{\eta}}$ is the effective impedance tensor. For cylindrical coordinates and a surface r =constant, it is given by

$$\overline{\overline{\eta}} = Z\left[1 - \frac{2}{2jk_0N}\frac{\partial}{\partial r}(\ln Z)\right]\overline{\overline{I}} - \frac{Z}{2jk_0Nr}\left(\hat{\phi}\hat{\phi} - \hat{z}\hat{z}\right), \tag{3.11}$$

where N is the diffraction index $N = \sqrt{\varepsilon_r\mu_r}$ (the derivative is evaluated at the surface). Equation (3.11) gives a first idea about the magnitude of the term neglected when using Eq. (3.9). Later we will give more explicit validity limits.

Since $N \to N$ and $Z \to 1/Z$ under the duality transformation, it can be verified that Eq. (3.10) satisfies duality to first order in $|N|^{-1}$. The anisotropy is a consequence of the curvature of the surface; in the special cases of planar or spherical surfaces, the effective impedance becomes a scalar.

To the order shown, only the normal variation of the impedance has an effect. This is consistent with the interpretation of the surface impedance as the local impedance "looking into the metal" and provides justification for applying the SIBC Eq. (3.9) at each point of a surface even when the properties of the material vary laterally.

A surface subject to an impedance boundary condition supports electric and magnetic currents

$$\boldsymbol{J}_{Se} = -\boldsymbol{n} \times \boldsymbol{H} \quad \text{and} \quad \boldsymbol{J}_{Sm} = \boldsymbol{n} \times \boldsymbol{E}, \tag{3.12}$$

respectively, and these are evidently related; $\boldsymbol{n}$ is the outward unit normal. Thus, from Eq. (3.11) written for a scalar effective impedance $\overline{\overline{\eta}} = \eta$

$$\boldsymbol{J}_{Se} = \frac{1}{\eta}\boldsymbol{n} \times \boldsymbol{J}_{Sm} \quad \text{or} \quad \boldsymbol{J}_{Sm} = -\eta\,\boldsymbol{n} \times \boldsymbol{J}_{Se}, \tag{3.13}$$

so that in the solution of a boundary value problem it is sufficient to determine just one current.

On the surface of a lossy medium for which we can consider $\overline{\overline{\eta}} = Z$, the conditions under which Eq. (3.10) can be justified have been discussed in [43]–[44] and the summary of the requirements is:

(i) On the surface the external field is slowly varying on a scale of λ_0 (e.g. no sharp edges).

(ii) Any variation of the material properties is slow on a scale of the local wavelength in the material, i.e.

$$\left|k_0^{-1}N^{-1}\nabla(lnZ)\right| \ll 1. \tag{3.14}$$

(iii) At each point of the material

$$|N| \gg 1. \tag{3.15}$$

(iv) At each point of the material

$$|Im(N)|\, k_0\rho \gg 1. \tag{3.16}$$

where ρ is the smallest radius of curvature or dimension of the body.

Based on detailed examinations of computed data and comparisons with situations where exact results are known, the last two conditions are rewritten in [45] as

$$|N| \gtrsim 10 \quad \text{and} \quad |Im(N)|\, k_0\rho \gtrsim 2.3. \tag{3.17}$$

For practical reasons, since we seek for (semi)analytical solution, we will use Eq. (3.9) and its validity limits are such that the higher order terms can be neglected. On top of that, we will deal with good conductors where (in our frequency range) the displacement current can be neglected compared to the conduction current, that is

$$\varepsilon = \varepsilon_0 - \frac{\sigma}{j\omega} \approx \frac{j\sigma}{\omega} \quad \text{and then} \quad Y(\omega) = \sqrt{\frac{\varepsilon}{\mu}} \approx j\sqrt{\frac{\sigma}{j\omega\mu}}; \tag{3.18}$$

this last assumption imposes an upper frequency limit weaker than the constraint imposed by Eqs. (3.15)–(3.17). The expression of the complex electrical permittivity ε depends on the time dependence of the field; for a time dependence of $\exp(j\omega t)$, ε is simply the complex conjugate of Eq. (3.18). The length of penetration of the field in a conductor is referred to as "skin depth" and is given by

$$\delta = \sqrt{\frac{2}{\omega\mu_0\sigma}} = \sqrt{2}\left|N^{-1}k_0^{-1}\right| \quad \text{since} \quad N = \sqrt{\frac{j\sigma}{\omega\varepsilon_0}} \tag{3.19}$$

for non magnetic conductors ($\mu_r = 1$). Therefore Eq. (3.14) states that the variation of material properties is slow on the scale of a skin depth, while Eq. (3.16) imposes that the minimum radius of curvature of the surface has to be much larger than the skin depth (at any relevant frequency).

3.3.1 Model surface admittance

Our aim is to find the fields generated by an ultrarelativistic charge travelling in a conducting beam pipe whose conductivity σ is a function of the azimuth ϕ, but is constant in the radial and longitudinal direction. Assuming for $\sigma = \sigma(\phi)$ a sinusoidal behaviour, such as

$$\sigma(\phi) = \left[\frac{\sqrt{\sigma_{max}} + \sqrt{\sigma_{min}}}{2} + \frac{\sqrt{\sigma_{max}} - \sqrt{\sigma_{min}}}{2} \cos(n\phi)\right]^2, \tag{3.20}$$

the surface admittance is as well a function of ω and ϕ, that is

$$Y(\omega, \phi) = Y_0(\omega) + Y_n(\omega) \cos(n\phi) \qquad \left(\Omega^{-1}\right); \tag{3.21}$$

n is the number of oscillations of the conductivity between σ_{max} and σ_{min} along the pipe circumference. Y_0 depends on the square root of the frequency, while Y_n/Y_0 is a purely geometrical factor:

$$Y_0(\omega) = \sqrt{\frac{j}{\omega\mu_0}} \frac{\sqrt{\sigma_{max}} + \sqrt{\sigma_{min}}}{2} \quad \text{and} \quad \frac{Y_n}{Y_0} = \frac{\sqrt{\sigma_{max}} - \sqrt{\sigma_{min}}}{\sqrt{\sigma_{max}} + \sqrt{\sigma_{min}}} \tag{3.22}$$

from Eq. (3.18) and considering non magnetic conductors. Big changes in the conductivity imply values of Y_n/Y_0 near unity. For example if the conductivity varies from the one of copper (at room temperature) $\sigma_{Cu} = 6 \times 10^7$ S/m to the conductivity of the stainless steel $\sigma_{Ss} = 10^6$ S/m, then Y_n/Y_0 is $\simeq 0.76$; such a behaviour of the conductivity σ is shown in Fig. 3.1. Y_n/Y_0 "measures" the variation of conductivity along the azimuth ($Y_n/Y_0 = 0$ is a homogeneous conductor); our final solution (see Sec. 3.6) is derived as an expansion in this parameter; when it approaches to unity, more high order terms are needed. The penetration in the metal follows the skin depth: at a given frequency it is bigger in the worst conductor, as shown in Fig. 3.1 (dash-dotted line). Typical values are of the order of microns for copper and ten microns for stainless steel at 1 GHz.

Eventually to asses the applicability limits of the SIBCs, we will use Eq. (3.17), that is that the skin depth has to be smaller than the wavelength and than the radius of the pipe. For example using the numerical values given in Fig. 3.1, the lower limit in frequency is ≈ 1 kHz while the upper one is ≈ 200 THz (at least concerning the use of Leontovich boundary conditions).

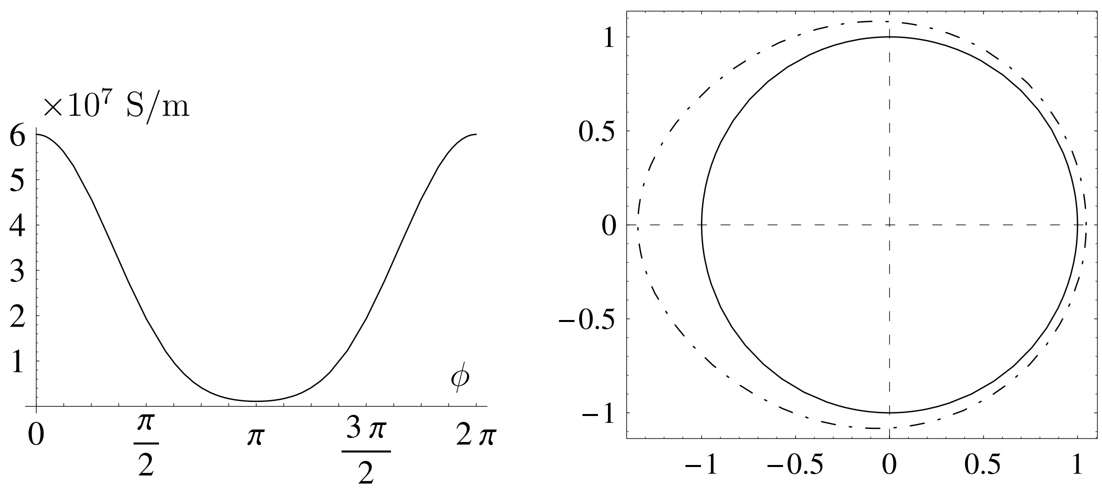

Figure 3.1: Shape of the conductivity as a function of the azimuth ϕ (left plot) and corresponding behaviour of the skin depth inside the conductor at 5 kHz (right plot). The conductivity varies from copper at room temperature ($\phi = 0$) to stainless steel ($\phi = \pi$). In the right plot, the black line represents the circular section of the pipe (in units of the radius) and the dash-dotted line is $\delta(\phi)/b$ away from it, where b is the pipe radius. ($b = 2$ cm, $\sigma_{Cu} = 6\ 10^7$ S/m, $\sigma_{Ss} = 10^6$ S/m)

3.4 Known cases

Before going through the detailed analysis of the effect of an azimuthal variation of the conductivity, we review a few well known cases in the framework of the formalism presented in Sec. 3.2–3.3.

A charge Q travelling in the free space in the z-direction with a velocity βc is associated with a current density (in the frequency domain) of:

$$\boldsymbol{J}(r, \phi, z; \omega) = \hat{z} Q \frac{\delta(r)}{2\pi r} \exp\left(j \frac{k}{\beta} z \right). \tag{3.23}$$

The electric Hertzian potential does not depend on ϕ and, following Eqs. (C.1–C.2) with $b = 0$, it is

$$\Pi_{0z} = j \frac{Z_0 Q}{2\pi k} K_0 \left(\frac{kr}{\beta\gamma} \right) \exp\left(j \frac{k}{\beta} z\right), \tag{3.24}$$

with γ being the relativistic factor. The fields are then easily obtained using Eqs. (3.3) with the only electric potential and they are reported in Appendix C.1. In the ultrarelativistic regime, i.e. when the particle velocity approaches the speed of light ($\gamma \to \infty$), the only non-vanishing field components are the radial electric field and the azimuthal magnetic one.

In a perfectly conducting pipe, the field will be the sum of the field of the charge in the free space (known) and a *scattered* field (unknown, for the moment), due to the presence of the perfectly conducting boundary; thus the total Hertzian potential will be as well the sum of the free space one (Π_{0z}) and of Π_{iz} which can be written as in Eq. (3.5a), namely

$$\Pi_{TOTz} = \Pi_{0z} + \frac{Z_0}{4\pi k} \int_{-\infty}^{\infty} F_0(\alpha) G_0(\alpha; r, b) e^{j\alpha z} d\alpha, \tag{3.25}$$

where only the monopole term $m = 0$ has been taken due to the symmetries (the charge is travelling along the z-axis); $G_0(\alpha; r, b)$ is defined in Eq. (3.6). Applying the boundary condition, i.e. that the E_z is null at $r = b$, $F_0(\alpha)$ can be derived from a potential Π_{TOTz} that is zero for $r \geq b$ and

$$\Pi_{TOTz} = j\frac{Z_0 Q}{2\pi k}\left[K_0\left(kr/\beta\gamma\right) - \frac{K_0\left(kb/\beta\gamma\right)}{I_0\left(kb/\beta\gamma\right)} I_0\left(kr/\beta\gamma\right)\right] e^{jzk/\beta} \quad \text{for} \quad r < b, \tag{3.26}$$

as shown in Appendix C.1. The well known properties of a charge travelling in a perfectly conducting pipe are easily found in Eq. (3.26). First of all, there is no field inside the perfect conductor ($r > b$), since the Hertzian potential is zero; moreover $I_0(kr/\beta\gamma)$ tends to unity in the ultrarelativistic limit and thus the field generated by Π_{TOTz} is identical to the one generated by Π_{0z} inside the pipe ($r < b$), since they differ only by a constant. Therefore inside a perfectly conducting pipe, the field of a relativistic charge is identical to the one in the free space, while it is zero for $r > b$: perfectly conducting walls "cut" the field lines. The surface current density, according to Eqs. (3.8a, C.8), is

$$J_{Sz} = -\frac{Q}{2\pi b} \frac{e^{jzk/\beta}}{I_0(kb/\beta\gamma)} \longrightarrow -\frac{Q}{2\pi b} e^{jzk/\beta} \quad \text{for } \beta \to 1. \tag{3.27}$$

The image current flowing in a perfect conductor (i.e. the integral of J_{Sz} along a generic circle of radius b) is equal in amplitude to the current of the charge, (that is the integral of J_z in Eq. (3.23) over a generic surface normal to the propagation direction), but opposite in sign.

When the charge is moving in a pipe with finite, uniform conductivity σ, the Hertzian potential can still be written as in Eq. (3.25), but with a different $F_0(\alpha)$ since the fields satisfy different boundary conditions (E_z is not anymore null on the boundary). Again, only the monopole term ($m = 0$) has an effect and this is related to the symmetry imposed by the uniform conductivity. To first order, the longitudinal electric field and the azimuthal magnetic one satisfy the SIBC discussed in Sec. 3.3, in particular Eq. (3.9). Applying this condition, we find again an equation for $F_0(\alpha)$ which leads to the following expression for the total Hertzian potential:

$$\Pi_{TOTz} = j\frac{Z_0 Q}{2\pi k}\left[K_0\left(kr/\beta\gamma\right) - \frac{K_0\left(kb/\beta\gamma\right) - j\frac{\beta\gamma}{Z_0 Y}K_1\left(kb/\beta\gamma\right)}{I_0\left(kb/\beta\gamma\right) + j\frac{\beta\gamma}{Z_0 Y}I_1\left(kb/\beta\gamma\right)}I_0\left(kr/\beta\gamma\right)\right]e^{jzk/\beta}, \quad (3.28)$$

where $Y = 1/Z$ has been used. Such expression is meaningful only for $r < b$ since assuming the SIBC, we implicitly assume a null field inside the conductor. In the limit of perfect conductor ($Y \to \infty$), Eq. (3.28) becomes Eq. (3.26), as it should be. All the fields can be, again, derived by the potential; in particular the longitudinal electric field is non-vanishing and constant with r; in fact (see Appendix C.1) for an ultrarelativistic charge Q

$$E_z = \frac{Q}{2\pi b}\frac{1/Y}{1 + jkb/\left(2Z_0 Y\right)}e^{jkz} \quad (3.29)$$

meaning that the travelling charge loses energy. Equation (3.29) is a result well known in literature (see for example [15, 46]).

3.5 System of equation for azimuthally varying admittance

The fields E_ϕ, H_ϕ, E_z, H_z satisfy the boundary condition Eq. (3.9), that we may rewrite in our circular geometry as:

$$\left.H_\phi\right|_{r=b} = Y(\omega,\phi)\left.E_z\right|_{r=b} \quad \text{and} \quad \left.H_z\right|_{r=b} = -Y(\omega,\phi)\left.E_\phi\right|_{r=b}, \quad (3.30)$$

where the surface admittance $Y(\omega, \phi)$ is (co)sinusoidal in ϕ and given by Eq. (3.21). The fields involved in Eq. (3.30) are the total fields on the boundary, that is the sum of the scattered field and the field of the source. We will use the superscript "w" for the scattered field (e.g. H_ϕ^w) and the superscript "$S.C.$" (space charge) for the source field (e.g. $H_\phi^{S.C.}$).

The scattered fields (on the boundary $r = b$) can be written as

$$\left.E_\phi^w\right|_{r=b} = -\frac{Z_0}{2\pi^2}E_\phi^m \sin(m\phi), \quad (3.31a)$$

$$\left.E_z^w\right|_{r=b} = \frac{Z_0}{2\pi^2}jkbE_z^m \cos(m\phi) + \frac{Z_0}{2\pi^2}jkbI_0 H_\phi^0, \quad (3.31b)$$

$$\left.H_\phi^w\right|_{r=b} = \frac{1}{2\pi^2}H_\phi^m \cos(m\phi) + \frac{1}{2\pi^2}\frac{(kb)^2}{2}\left(\frac{2\beta\gamma}{kb}I_0'\right)H_\phi^0, \quad (3.31c)$$

$$\left.H_z^w\right|_{r=b} = -\frac{j}{2\pi^2}H_z^m \sin(m\phi), \quad (3.31d)$$

where $m = 1, 2, \ldots$ and the "Einstein" summation rule over repeated indices is assumed. The coefficients can be obtained by comparison with Eqs. (C.5), i.e.

$$H_\phi^0 = \frac{1}{b}\frac{F_0}{\beta^2\gamma^2}K_0, \tag{3.32a}$$

$$E_\phi^m = \frac{m}{\beta}\frac{F_m}{b}I_m K_m - \widetilde{F}_m I'_m K'_m, \tag{3.32b}$$

$$H_\phi^m = \frac{kb}{\beta\gamma}\frac{F_m}{b}I'_m K_m - \frac{m}{\beta}\frac{\beta\gamma}{kb}\widetilde{F}_m I_m K'_m, \tag{3.32c}$$

$$E_z^m = \frac{1}{b}\frac{F_m}{\beta^2\gamma^2}I_m K_m, \tag{3.32d}$$

$$H_z^m = \frac{\widetilde{F}_m}{\beta\gamma}I_m K'_m, \tag{3.32e}$$

The arguments of the Bessel functions are always $kb/\beta\gamma$ and thus they have been omitted; the exponential factor $\exp(j\,z\,k/\beta)$ is not included as well. The new variables E_ϕ^m, H_ϕ^m, E_z^m, H_z^m have the dimension of a magnetic field in the Fourier space (that is C/m).

By substituting the last two Eqs. (3.32d–e) in the Eqs. (3.32b–c), we get:

$$E_\phi^m - H_\phi^m = (\beta\gamma)^2\left(\frac{m}{\beta} - \frac{kb}{\beta\gamma}\frac{I'_m}{I_m}\right)\left(E_z^m + \frac{H_z^m}{kb}\right), \tag{3.33a}$$

$$\frac{H_\phi^m}{(\beta\gamma)^2} = \frac{kb}{\beta\gamma}\frac{I'_m}{I_m}E_z^m - \frac{m}{\beta}\frac{H_z^m}{kb}, \tag{3.33b}$$

$$\frac{E_\phi^m}{(\beta\gamma)^2} = \frac{m}{\beta}E_z^m - \frac{I'_m}{I_m}\frac{H_z^m}{\beta\gamma}. \tag{3.33c}$$

The above quantities are limited and in general non null, since they appear directly in the fields. The previous relations hold for any value of β or more exactly for any value of $kb/\beta\gamma$.

In the ultrarelativistic limit, using Eq. (C.14) and the relation between β and γ, we get:

$$H_\phi^m - E_\phi^m \approx -\frac{1}{2}\left[m + \frac{(kb)^2}{m+1}\right]\left(E_z^m + \frac{H_z^m}{kb}\right) \quad \text{and} \quad E_z^m \approx \frac{H_z^m}{kb}, \tag{3.34}$$

since $E_\phi^m/(\beta\gamma)^2 \to 0$. The last relation can be obtained also from $H_\phi^m/(\beta\gamma)^2 \to 0$. Eventually we can write

$$H_z^m = A_m\left(H_\phi^m - E_\phi^m\right) \quad \text{and} \quad E_z^m = \frac{A_m}{kb}\left(H_\phi^m - E_\phi^m\right), \tag{3.35}$$

where

$$A_m = \frac{(m+1)kb}{(kb)^2 + m(m+1)}; \tag{3.36}$$

thus all the coefficients of the field on the boundary (see Eq. (3.31)) are now expressed in terms of the new variables H_ϕ^m and E_ϕ^m; we are actually changing variables from F_m, $\widetilde{F}_m$ to H_ϕ^m and E_ϕ^m.

The proportionality between the E_z^m and H_z^m agrees with the multipole field obtained in [33] (Eq. (2.34), pag. 52) by solving the Maxwell equations written for a particle travelling at the speed of light.

In the ultrarelativistic limit, the fields on the boundary are still given by Eqs. (3.31), with

$$I_0 \to 1 \quad \text{and} \quad \left(\frac{2\beta\gamma}{kb} I_0'\right) \to 1. \tag{3.37}$$

The source field has been derived in Sec. 3.4 and reported in Eqs. (C.6); for an ultrarelativistic particle travelling on axis the longitudinal electric field vanishes, that is

$$H_\phi^{S.C.} \approx \frac{Q}{2\pi b} \quad \text{and} \quad E_z^{S.C.} \approx 0, \tag{3.38}$$

Q being the charge of the particle(s) and having dropped the propagation (phase) factor.

By using Eqs. (C.15–C.16) (Appendix C.3) in Eq. (3.30) and equating the coefficients of sine (cosine) of the same order, a system of equations can eventually be written:

$$\frac{(kb)^2}{2} H_\phi^0 = Z_0 Y_0 \left(jkbH_\phi^0 + \frac{2\pi^2}{Z_0} E_z^{S.C.} + \frac{Y_n}{2Y_0} jkbE_z^n \right) - 2\pi^2 H_\phi^{S.C.}, \tag{3.39a}$$

$$H_\phi^n = Z_0 Y_0 \left(jkbE_z^n + \frac{Y_n}{2Y_0} jkbE_z^{2n} + \frac{Y_n}{Y_0}\frac{2\pi^2}{Z_0} E_z^{S.C.} + \frac{Y_n}{Y_0} jkbH_\phi^0 \right), \tag{3.39b}$$

$$-jH_z^n = Z_0 Y_0 \left(E_\phi^n + \frac{Y_n}{2Y_0} E_\phi^{2n} \right), \tag{3.39c}$$

$$H_\phi^{tn} = Z_0 Y_0 \left[jkbE_z^{tn} + jkb\frac{Y_n}{2Y_0} E_z^{(t-1)n} + jkb\frac{Y_n}{2Y_0} E_z^{(t+1)n} \right] \quad t = 2, 3, \ldots, \tag{3.39d}$$

$$-jH_z^{tn} = Z_0 Y_0 \left[E_\phi^{tn} + \frac{Y_n}{2Y_0} E_\phi^{(t-1)n} + \frac{Y_n}{2Y_0} E_\phi^{(t+1)n} \right] \quad t = 2, 3, \ldots, \tag{3.39e}$$

the forcing terms are the components of the charge field while the unknowns are only H_ϕ^0, H_ϕ^{kn} and E_ϕ^{kn} ($k = 1, 2, \ldots$). As discussed in Appendix C.3, orders different from kn give no contribution to the final solution. The system has a quite regular structure, except for the 0th and the 1st orders where the source terms appear and since there is no term in E_ϕ^m analogous to H_ϕ^0 (the azimuthal electric field has a null average along the azimuth). Each equation of the system relates the term of order tn to only terms of order $(t-1)n$ and $(t+1)n$; this symmetry will be exploited in the solution.

Inserting Eq. (3.35) into Eqs. (3.39), we can rewrite the system in the two variables that we will actually use to solve it, that is H_ϕ^{tn} and E_ϕ^{tn}.

- Zeroth Order

$$\frac{(kb)^2}{2}H_\phi^0 + 2\pi^2 H_\phi^{S.C.} = Z_0Y_0\left[jkbH_\phi^0 + \frac{2\pi^2}{Z_0}E_z^{S.C.} + j\frac{Y_n}{2Y_0}A_n\left(H_\phi^n - E_\phi^n\right)\right]. \tag{3.40}$$

- First Order

$$\begin{aligned}(1 - jZ_0Y_0A_n)\,H_\phi^n + jZ_0Y_0A_nE_\phi^n &= Z_0Y_0\left(\frac{Y_n}{Y_0}\frac{2\pi^2}{Z_0}E_z^{S.C.} + \frac{Y_n}{Y_0}jkbH_\phi^0\right) + \\ &\quad jZ_0Y_0\frac{Y_n}{2Y_0}A_{2n}\left(H_\phi^{2n} - E_\phi^{2n}\right), \end{aligned} \tag{3.41a}$$

$$A_nH_\phi^n - (A_n + jZ_0Y_0)\,E_\phi^n = jZ_0Y_0\frac{Y_n}{2Y_0}E_\phi^{2n}. \tag{3.41b}$$

- Order t $(t = 2, 3, \ldots)$

$$\begin{aligned}(1 - jZ_0Y_0A_{tn})\,H_\phi^{tn} + jZ_0Y_0A_{tn}E_\phi^{tn} &= j\frac{Y_n}{2Y_0}Z_0Y_0A_{(t-1)n}\left[H_\phi^{(t-1)n} - E_\phi^{(t-1)n}\right] + \\ &\quad j\frac{Y_n}{2Y_0}Z_0Y_0A_{(t+1)n}\left[H_\phi^{(t+1)n} - E_\phi^{(t+1)n}\right] \end{aligned} \tag{3.42a}$$

$$A_{tn}H_\phi^{tn} - \left(A_{tn} + jZ_0Y_0E_\phi^{tn}\right) = j\frac{Y_n}{2Y_0}Z_0Y_0E_\phi^{(t-1)n} + j\frac{Y_n}{2Y_0}Z_0Y_0E_\phi^{(t+1)n} \tag{3.42b}$$

3.6 Recursive solution of the System

The system of equations (3.40)–(3.41)–(3.42) is, in general, of infinite dimension and it is not diagonal: an analytical solution is therefore impossible. We may truncate it at a given order L, that is $H_\phi^{tn} = E_\phi^{tn} = 0$ for any $t > L$. Then exploiting the symmetries of the system, we can build a recursive solution. Considering Eqs. (3.42), the variable at the order t depends on both the orders $(t-1)$ and $(t+1)$. We can always write

$$H_\phi^{tn} = \frac{Y_n}{2Y_0}C_{tn}H_\phi^{(t-1)n} + \frac{Y_n}{2Y_0}D_{tn}E_\phi^{(t-1)n}, \tag{3.43a}$$

$$E_\phi^{tn} = \frac{Y_n}{2Y_0}E_{tn}H_\phi^{(t-1)n} + \frac{Y_n}{2Y_0}G_{tn}E_\phi^{(t-1)n}, \tag{3.43b}$$

where the dependence on the $(t+1)$–variable is hidden in the coefficients C, D, E, G, as it will become clearer later. The azimuthal change of the conductivity is directly related to $Y_n/2Y_0$. No assumption has been made in writing Eqs. (3.43) but neither any step towards the final solution. Using Eqs. (3.43) to write the $(t+1)$-variables as functions of the t-variables and substituting in Eqs. (3.42), we get

$$\begin{pmatrix} M_{11} & M_{12} \\ M_{21} & M_{22} \end{pmatrix} \begin{pmatrix} H_\phi^{tn} \\ E_\phi^{tn} \end{pmatrix} = j\frac{Y_n}{2Y_0} Z_0 Y_0 \begin{pmatrix} A_{(t-1)n} & -A_{(t-1)n} \\ 0 & 1 \end{pmatrix} \begin{pmatrix} H_\phi^{(t-1)n} \\ E_\phi^{(t-1)n} \end{pmatrix}. \tag{3.44}$$

The elements of the matrix $\mathbf{M}$ are:

$$M_{11} = 1 - jZ_0Y_0A_{tn} - jZ_0Y_0 \left(\frac{Y_n}{2Y_0}\right)^2 A_{(t+1)n} \left[C_{(t+1)n} - E_{(t+1)n}\right], \tag{3.45a}$$

$$M_{12} = jZ_0Y_0 \left\{ A_{tn} + \left(\frac{Y_n}{2Y_0}\right)^2 A_{(t+1)n} \left[D_{(t+1)n} - G_{(t+1)n}\right] \right\}, \tag{3.45b}$$

$$M_{21} = A_{tn} - j\left(\frac{Y_n}{2Y_0}\right)^2 Z_0Y_0E_{(t+1)n}, \tag{3.45c}$$

$$M_{22} = -A_{tn} - jZ_0Y_0 \left[1 + \left(\frac{Y_n}{2Y_0}\right)^2 G_{(t+1)n}\right], \tag{3.45d}$$

where the coefficients of order $(t+1)$ come from having written Eqs. (3.43) for $H_\phi^{(t+1)n}$ and $E_\phi^{(t+1)n}$. Therefore, Eq. (3.44) is simply a 2×2 system where the "unknowns" are H_ϕ^{tn}, E_ϕ^{tn} and the $H_\phi^{(t-1)n}$, $E_\phi^{(t-1)n}$ may be considered as driving terms. Inverting the matrix $\mathbf{M}$ and after some algebra, we get the following recurrence relations:

$$C_{tn} = -j\frac{Z_0Y_0}{\Delta_t} A_{(t-1)n} \left\{ A_{tn} + jZ_0Y_0 \left[1 + \left(\frac{Y_n}{2Y_0}\right)^2 G_{(t+1)n}\right]\right\}, \tag{3.46a}$$

$$\begin{aligned} D_{tn} = j\frac{Z_0Y_0}{\Delta_t} \Bigg\{ & A_{tn}A_{(t-1)n} + jZ_0Y_0\left[A_{(t-1)n} - A_{tn}\right] + \\ & + jZ_0Y_0 \left(\frac{Y_n}{2Y_0}\right)^2 \left\{A_{(t-1)n}G_{(t+1)n} - A_{(t+1)n}\left[D_{(t+1)n} - G_{(t+1)n}\right]\right\}\Bigg\}, \end{aligned} \tag{3.46b}$$

$$E_{tn} = -j\frac{Z_0Y_0}{\Delta_t} \left[A_{(t-1)n}A_{tn} - jZ_0Y_0 \left(\frac{Y_n}{2Y_0}\right)^2 A_{(t-1)n}E_{(t+1)n}\right], \tag{3.46c}$$

$$\begin{aligned} G_{tn} = j\frac{Z_0Y_0}{\Delta_t} \Bigg\{ & A_{tn}A_{(t-1)n} + 1 - jZ_0Y_0A_{tn} + \\ & - jZ_0Y_0 \left(\frac{Y_n}{2Y_0}\right)^2 \left\{A_{(t-1)n}E_{(t+1)n} + A_{(t+1)n}\left[C_{(t+1)n} - E_{(t+1)n}\right]\right\}\Bigg\}, \end{aligned} \tag{3.46d}$$

where

$$\Delta_t = det\,(\mathbf{M}) = M_{11}M_{22} - M_{12}M_{21}. \tag{3.47}$$

The initial condition of such a recurrence relation is simply given by the truncation of the system at a given order $t = L$, that is

$$C_{(L+1)n} = D_{(L+1)n} = E_{(L+1)n} = G_{(L+1)n} = 0. \tag{3.48}$$

To summarise, once fixed the order of truncation L the coefficients C_{tn}, D_{tn}, E_{tn} and G_{tn} can be computed by using Eqs. (3.46) with the initial condition given by Eq. (3.48). Then, applying Eqs. (3.43), H_ϕ^{tn} and E_ϕ^{tn} are known once determined $H_\phi^{(t-1)n}$ and $E_\phi^{(t-1)n}$, for $t \geq 2$. Therefore the next step is to find H_ϕ^0, H_ϕ^n and E_ϕ^n which are directly dependent on the source $H_\phi^{S.C.}$, $E_z^{S.C.}$, as shown in Eqs. (3.40)–(3.41).

Writing H_ϕ^n and E_ϕ^n according to Eqs. (3.43), we can write Eqs. (3.41) as:

$$\mathbf{M}\begin{pmatrix} H_\phi^n \\ E_\phi^n \end{pmatrix} = j\frac{Y_n}{Y_0}Z_0Y_0\begin{pmatrix} A_0 & 0 \\ 0 & 0 \end{pmatrix}\left\{(kb)^2\,H_\phi^0 - j\frac{2\pi^2}{Z_0}kbE_z^{S.C.}\right\}, \tag{3.49}$$

where the elements of the matrix $\mathbf{M}$ are again given by Eqs. (3.45), but now considering $t = 1$ and $A_0 = 1/(kb)$, following Eq. (3.36). Eventually solving this 2×2 system, we get

$$H_\phi^n = \frac{Y_n}{Y_0}C_n(kb)^2H_\phi^0 \quad \text{and} \quad E_\phi^n = \frac{Y_n}{Y_0}E_n(kb)^2H_\phi^0, \tag{3.50}$$

neglecting $E_z^{S.C.}$ in the ultrarelativistic limit of Eq. (3.38); the coefficients C_n and D_n are then given by Eqs. (3.46), assuming $t = 1$. Strictly speaking, Eqs. (3.46) hold only for $t \geq 2$; nevertheless for sake of simplicity and in view of a later computation we can redefine C_{tn}, D_{tn}, E_{tn} and G_{tn} such as that they obey Eqs. (3.46) for $t \geq 1$ with the additional condition

$$D_n = G_n = 0. \tag{3.51}$$

This "asymmetry" between the coefficients takes into account that E_ϕ has zero average over the azimuth ($E_\phi^n = 0$). Eventually, Eq. (3.40) becomes

$$H_\phi^0 = -2\pi^2H_\phi^{S.C.}\left[\frac{(kb)^2}{2} - jkbZ_0Y_0 - jZ_0Y_0\left(\frac{Y_n}{2Y_0}\right)^2 2A_n\,(C_n - E_n)\,(kb)^2\right]^{-1}, \tag{3.52}$$

where $H_\phi^{S.C.}$ is given by Eq. (3.38).

The solution is now complete. It is not known in a closed analytical formula, but nevertheless it can be computed. Once chosen the value of L, according to the desired degree of approximation, the solution can be obtained by going through the following steps:

1. Compute C_{tn}, D_{tn}, E_{tn} and G_{tn} using Eqs. (3.46) for $t \geq 1$, with initial conditions given by Eq. (3.48) and Eq. (3.51).

2. After having obtained H_ϕ^0 from Eqs. (3.52), compute H_ϕ^{tn} and E_ϕ^{tn} from Eq. (3.43) and Eq. (3.50).

3. Compute the scattered field on the boundary with Eq. (3.31) and Eq. (3.35), keeping in mind that $m = tn$ with $t = 1, 2, \ldots$.

The previous algorithm has been implemented in a *Mathematica* notebook. The evaluation of Eqs. (3.46) may result in a very heavy and time consuming (not feasible) computing task, if the recurrence law is applied directly. To speed up the computation, the so called "Dynamic Programming" has been applied [47]. The idea is simply to force each function to "remember" results of previous evaluations ([48], pag. 295) in order to avoid repetition of expensive calculations, as one would do in a self-made code. Therefore each generic recursive function f in that notebook has been defined using the following "idiom" (in *Mathematica* language):

$$f\,[x\_] := f\,[x] =< rhs > .$$

The solution obtained in this way is a semi-analytical one; its accuracy depends on the order L where the system of Eqs. (3.40–3.42) is truncated.

In principle, if the system is truncated at order L, the boundary conditions are satisfied up to order $(L-1)n$; this means that the quantity

$$\mathcal{E}_\phi = \left| \frac{H_\phi^L - Y(\omega) E_z^L}{H_\phi^{S.C.}} \right|_{r=b} \tag{3.53}$$

is proportional to $\cos(L\phi)$. The superscript L recalls that the solution is approximated to order L and thus that the fields are sinusoidal functions of $tn\phi$ with $t = 0, \ldots, L$. The same conclusion applies to

$$\mathcal{E}_z = \left| \frac{H_z^L + Y(\omega) E_\phi^L}{H_z^n} \right|_{r=b} \tag{3.54}$$

which is proportional to $\sin(L\phi)$. Equations (3.53–3.54) are simply the ratio between the term not satisfying a boundary condition and the amplitude of the lower order term of the fields involved in that boundary condition. Later we will use Eqs. (3.53–3.54) to asses the validity of our solution (Sec. 3.8).

3.7 Field solution for $\beta \to 1$

In the previous section 3.6, we have shown how to get the field on the boundary, namely for $r = b$. The field in the internal region ($r < b$) is given by Eqs. (C.5) as a function of two constants F_m and $\widetilde{F}_m$, directly related to the values of the field on the boundary.

First of all, only terms of orders $m = tn$ ($t = 0, 1, 2, \ldots$) do contribute to the solution. For such terms, it holds

$$E_z^{tn} = \frac{1}{b}\frac{F_{tn}}{\beta^2\gamma^2} I_{tn}\left(\frac{kb}{\beta\gamma}\right) K_{tn}\left(\frac{kb}{\beta\gamma}\right) \approx \frac{1}{b}\frac{F_{tn}}{\beta^2\gamma^2}\frac{1}{2tn}, \tag{3.55a}$$

$$H_z^{tn} = \frac{\widetilde{F}_{tn}}{\beta\gamma} I_{tn}\left(\frac{kb}{\beta\gamma}\right) K'_{tn}\left(\frac{kb}{\beta\gamma}\right) \approx -\frac{1}{2kb}\widetilde{F}_{tn}, \tag{3.55b}$$

where E_z^{tn} and H_z^{tn} are actually the longitudinal electric and magnetic field on the boundary which can be computed as shown in Sec. 3.6. Since E_z^{tn} and H_z^{tn} are proportional (see Eq. (3.35)), also F_{tn} and $\widetilde{F}_{tn}$ are proportional to each other. Applying the small argument approximations of Bessel functions [49] and taking the ultrarelativistic limit, we can write Eqs. (C.5) as functions of only $\widetilde{F}_{tn}$, that is (δ is the Kronecker symbol):

$$\begin{aligned}
E_r^w &= -\frac{Z_0}{8\pi^2}\left\{\left[\frac{tn}{(kb)^2} - \frac{1-\delta_{tn,1}}{tn-1}\right]\left(\frac{r}{b}\right)^{tn-1} + \frac{1}{tn+1}\left(\frac{r}{b}\right)^{tn+1}\right\}\widetilde{F}_{tn}\cos(tn\phi) + \\
&\quad + \frac{Z_0}{4\pi^2}\frac{r}{b}(kb)^2 H_\phi^0, && (3.56a)\\
E_\phi^w &= -\frac{Z_0}{8\pi^2}\left\{\left[\frac{1-\delta_{tn,1}}{tn-1} - \frac{tn}{(kb)^2}\right]\left(\frac{r}{b}\right)^{tn-1} + \frac{1}{tn+1}\left(\frac{r}{b}\right)^{tn+1}\right\}\widetilde{F}_{tn}\sin(tn\phi), && (3.56b)\\
E_z^w &= -\frac{Z_0}{4\pi^2}\frac{j}{kb}\left(\frac{r}{b}\right)^{tn}\widetilde{F}_{tn}\cos(tn\phi) + \frac{Z_0}{2\pi^2} jkbH_\phi^0, && (3.56c)\\
H_r^w &= \frac{1}{8\pi^2}\left\{\left[\frac{1-\delta_{tn,1}}{tn-1} + \frac{tn}{(kb)^2}\right]\left(\frac{r}{b}\right)^{tn-1} + \frac{1}{tn+1}\left(\frac{r}{b}\right)^{tn+1}\right\}\widetilde{F}_{tn}\sin(tn\phi), && (3.56d)\\
H_\phi^w &= \frac{1}{8\pi^2}\left\{\left[\frac{tn}{(kb)^2} + \frac{1-\delta_{tn,1}}{tn-1}\right]\left(\frac{r}{b}\right)^{tn-1} - \frac{1}{tn+1}\left(\frac{r}{b}\right)^{tn+1}\right\}\widetilde{F}_{tn}\cos(tn\phi) + \\
&\quad + \frac{1}{4\pi^2}\frac{r}{b}(kb)^2 H_\phi^0, && (3.56e)\\
H_z^w &= \frac{1}{4\pi^2}\frac{j}{kb}\left(\frac{r}{b}\right)^{tn}\widetilde{F}_{tn}\sin(tn\phi). && (3.56f)
\end{aligned}$$

We recall that the "Einstein" notation is adopted, $t = 1, 2, \ldots, L$ and the phase propagation factor $\exp(jkz)$ is dropped. As reminded by the superscript "w", the previous field is a scattered field and the total field in the beam pipe is the sum of this with the charge field. In the limit of constant conductivity ($Y_n \to 0$), we find the expected result of an E_z^w constant with ϕ and r (see Eq. (3.29)). For readers' convenience, Appendix C.2 is devoted to a summary of the Bessel functions approximations needed in the derivation of the previous Eqs. (3.56), while Appendix C.4 gives some guidelines in its derivation.

3.8 Numerical results and plots

Applying the results of the previous section, the field solution can be found analytically only for truncation indices L of the order of few units and therefore it is accurate only for small changes in conductivity (i.e. $Y_n/Y_0 \ll 1$), which is not our practical case. In this section we will present mainly numerical results and discuss their validity for arbitrary values of L. We are mostly interested in a conductivity varying from the copper one ($\sigma_{Cu} = 6\,10^7$ S/m at room temperature) to the stainless steel one ($\sigma_{Ss} = 10^6$ S/m), which correspond to $Y_n/Y_0 = 0.76$. Moreover the LHC will operate at cryogenic temperatures, where the conductivity σ of copper increases roughly by a factor 100, while electric properties of the stainless steel remain the same; this bigger variation in conductivity implies a Y_n/Y_0 much closer to unity, that is $Y_n/Y_0 = 0.97$. It is worth mentioning that in this case the lower frequency validity limit of SIBCs of Eq. (3.9) is now given by Eq. (3.14), that is a limitation on the spatial derivatives of $Y(\omega)$; the upper limit is unchanged since it is related to worstly conducting region.

3.8.1 Validity of the truncated numerical solution

First of all, the values of the coefficients C_{tn}, D_{tn}, E_{tn}, G_{tn} in Eqs. (3.46) depend on the order L to which the system of Eqs. (3.39) is truncated. For instance, for a given tn, C_{tn} is null if $L < tn$ (and the same holds for all the other coefficients); increasing L the coefficients approach their limit values with a velocity depending on the value of Y_n/Y_0. An example is given in Fig. 3.2 for the coefficients E_{tn} which have the slowest convergence; in the figure it is shown E_3, which is zero for $L < 2$ and then increases up to its limit value faster for $Y_n/Y_0 = 0.76$ (black dots) and slower for $Y_n/Y_0 = 0.97$ (gray dots). The saturation value is reached for $L \approx tn + 15$ in the worst case: this is approximately true for every tn and can be used in the actual solution. Thus if the system of Eqs. (3.39) is truncated to a given order L only the coefficients up to $tn \approx L - 15$ (in the worst case) are accurate. Obviously also the quantities directly involved in the field expressions of Eqs. (3.31) have the same saturating behaviour with L as shown in the right plot of Fig. 3.2 for H^0_ϕ; the convergence is somehow faster because also the coefficients other than E_n are involved (Eq. (3.52)). Both E_3 and H^0_ϕ are plotted normalised to their limit value.

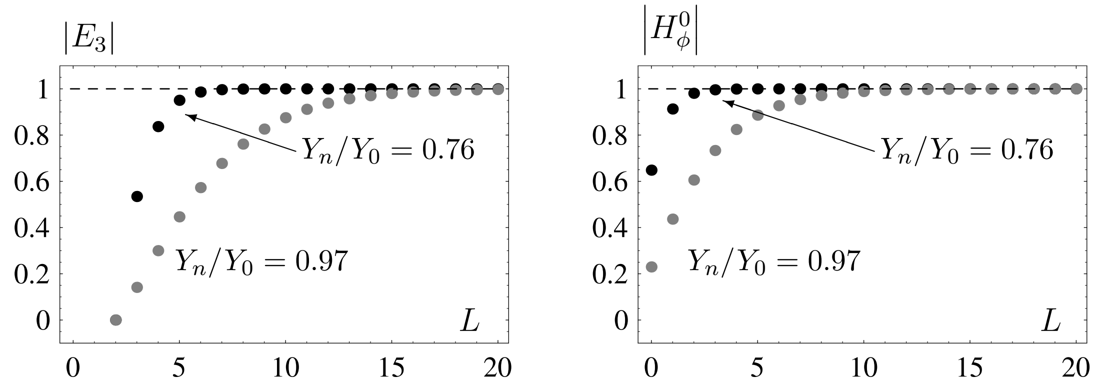

Figure 3.2: Convergence of the coefficients of the final solution as a function of the truncation order L at 1 GHz and for two different conductivity jumps. The left plot shows the coefficient E_3 from Eq. (3.46c) normalised to its limit value, while the right plot shows the average value of H_ϕ on the boundary normalised to its limit value. ($b = 2$ cm, $n = 1$)

For a given value of Y_n/Y_0, the accuracy of the solution of the system depends on the number of terms included (which we will call L from now on) and the order up to which the coefficients are calculated L' (and L' should be at least $\approx L + 15$ in the worst case). To asses the reliability of the truncation order L, we have introduced the quantities $\mathcal{E}_\phi$ and $\mathcal{E}_z$ in Eqs. (3.53–3.54). They are essentially the first term not included in the truncation of the solution, normalised to the lower order term; the solution may be considered reliable for a given order L, if $\mathcal{E}_\phi$, $\mathcal{E}_z \ll 1$. Increasing L, that is including more terms in the solution, $\mathcal{E}_\phi$ and $\mathcal{E}_z$ can be made as small as desired. An example is shown in Fig. 3.3 for $Y_n/Y_0 = 0.76$ at the frequency of 1 GHz and for $n = 1$; terms up to order $L = 10$ are included, resulting in $\mathcal{E}_\phi < 10^{-3}$ and $\mathcal{E}_z < 10^{-2}$. It is worth mentioning that $\mathcal{E}_\phi$ and $\mathcal{E}_z$ are sinusoidal functions of $L\phi$, as expected. For different frequencies, the maximum value of the errors is roughly of the same order (improving a little bit going to very small frequencies). To get the same order of

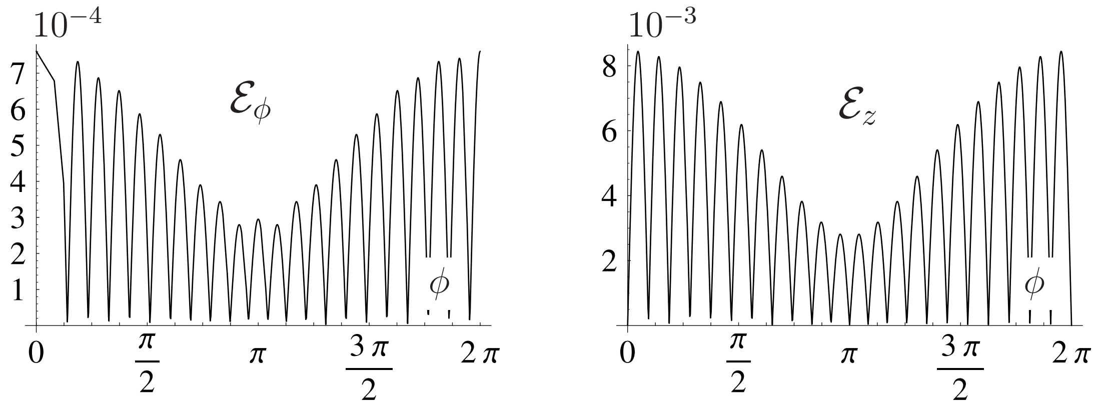

Figure 3.3: $\mathcal{E}_\phi$ and $\mathcal{E}_z$ for $Y_n/Y_0 = 0.76$ at 1 GHz; $L = 10$ but the coefficients are calculated at the order $L' = 16$. ($b = 2$ cm, $n = 1$)

magnitude of $\mathcal{E}_\phi$ and $\mathcal{E}_z$ with a higher conductivity jump, one should increase L. Figure 3.4 shows the situation for $Y_n/Y_0 = 0.97$ where a much higher number of terms ($L = 42$) is needed to keep $\mathcal{E}_\phi < 10^{-3}$ and $\mathcal{E}_z \lesssim 10^{-2}$. Again, changing frequency, more or less the same number of coefficients is needed to keep $\mathcal{E}_\phi$ and $\mathcal{E}_z$ constant. This is again a kind of higher limit in the interesting frequency range, for the given choice of L (and L').

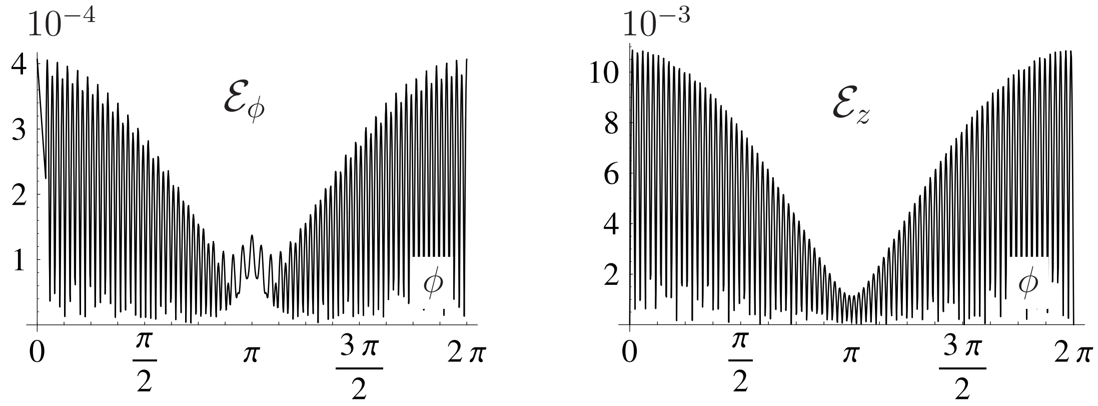

Figure 3.4: $\mathcal{E}_\phi$ and $\mathcal{E}_z$ for $Y_n/Y_0 = 0.97$ at 1 GHz; $L = 42$ but the coefficients are calculated at the order $L' = 60$. ($b = 2$ cm, $n = 1$)

3.8.2 Fields on the boundary

The surface density of the currents supported by the conductor is proportional to the magnetic field on the boundary, as stated in Eq. (3.12); the total current is then the integral along the circumference of such surface density. The behaviour of H_ϕ (the longitudinal current) is presented in Fig. 3.5 for various frequencies and for two different $\sigma(\phi)$; it is practically constant up to very low frequencies where the field (and the current) decreases in the worst conductor. The variation of the field is increasing with Y_n/Y_0. This is a first result important for the LHC: the current avoids the "bad" conductor only at very low frequencies and this may have consequences in the final design. To check if there is any evidence of azimuthal

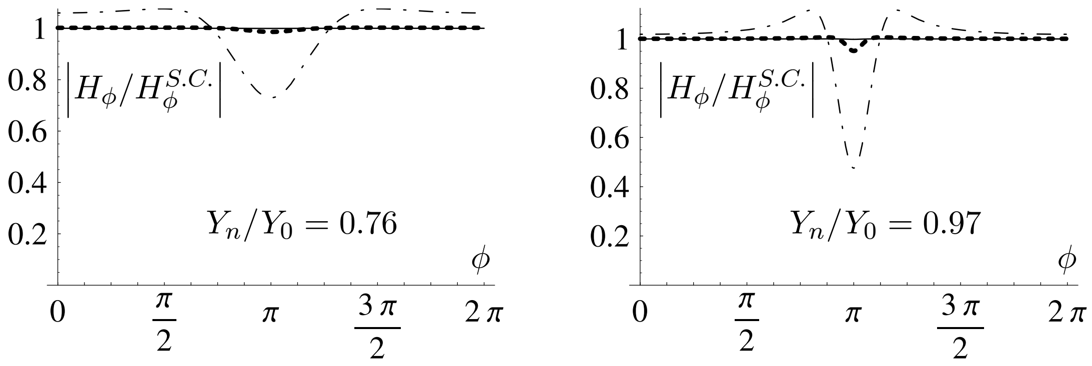

Figure 3.5: Azimuthal magnetic field on the boundary ($r = b$). The field is plotted at different frequencies: 1 GHz (solid line), 1 MHz (thick dashed line), 1 kHz (dot-dashed line) for two different variations of the conductivity. At the higher frequency the field is more or less constant and the solid lines are hardly visible. Increasing the variation in the conductivity, H_ϕ at the centre of the worst conductor decreases, but this is remarkable only at low frequencies. ($b = 2$ cm, $n = 1$)

currents, Figure 3.6 shows H_z, which is proportional to them, as shown in Eq. (3.12). The longitudinal magnetic field is negligible with respect to H_ϕ (four orders of magnitude of difference) and it is strongly decreasing with frequency; moreover it doesn't seem to depend strongly on the jump in the conductivity. Thus, the total field is TM-like.

The longitudinal electric field is found to be maximum in the worst conductor ($\phi = \pi$ if $n = 1$), as shown in Fig. 3.7 for two different jumps in the conductivity: the peak of the field is narrower for bigger variations in the conductivity, while its maximum seems not to be very much affected (at least in the examples shown). As we may expect, the longitudinal field is decreasing with at lower frequencies; in fact it is worth reminding that the average value (over ϕ) of E_z is constant with the radius, as stated in Eq. (3.56c) and thus it is equal to the longitudinal electric field on the z-axis. Then the longitudinal coupling impedance per unit length [39] can be roughly estimated by inspection of Fig. 3.7 (and of the analogous Figs. 3.10–3.13) that is exactly the longitudinal electric field per unit charge. The ϕ-average of E_z is simply proportional to the area of the curve representing the longitudinal electric field: it is smaller in the right plot which refers to a "cold" copper (that is more conducting

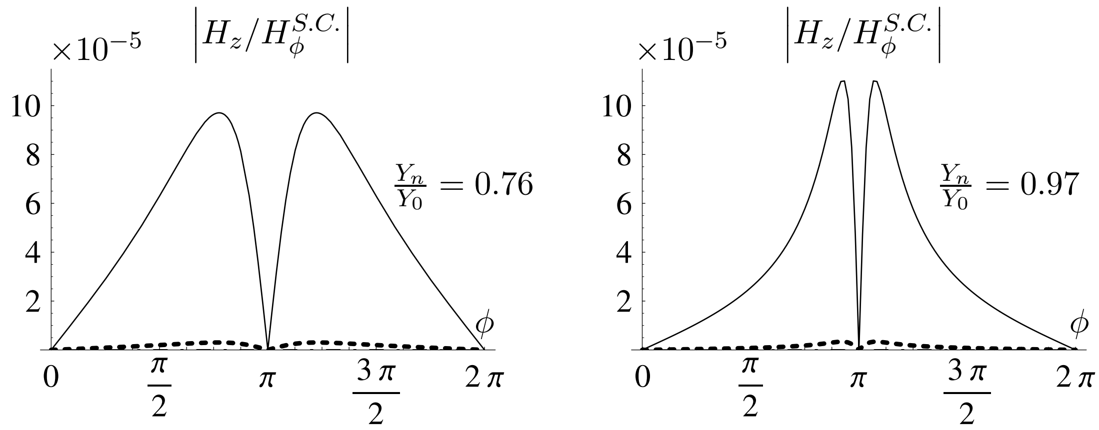

Figure 3.6: Longitudinal magnetic field on the boundary ($r = b$). The field is plotted at different frequencies: 1 GHz (solid line), 1 MHz (thick dashed line), 1 kHz (dot-dashed line) for two different variations of the conductivity. The field at 1 kHz is four orders of magnitudes smaller than at 1 GHz and the dot-dashed lines lie on the horizontal ϕ-axis. H_z is negligible with respect to H_ϕ even at 1 GHz, showing the TM nature of the excited field. ($b = 2$ cm, $n = 1$)

than at room temperatures) and this is physically sound.

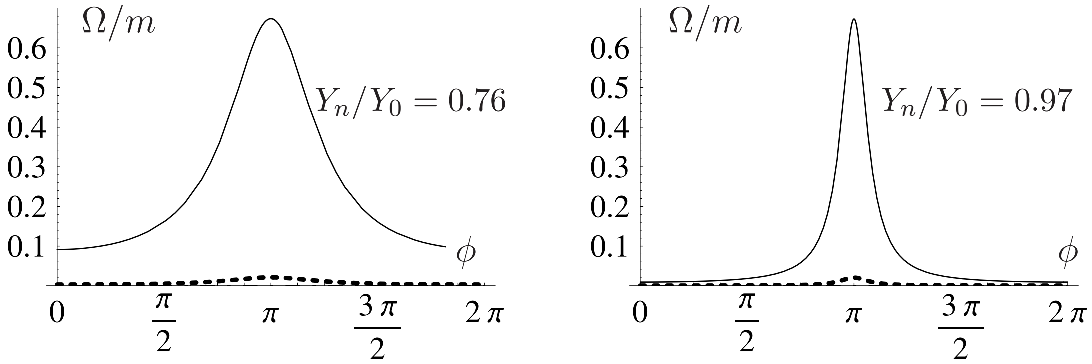

Figure 3.7: Longitudinal electric field on the boundary ($r = b$) per unit charge. The absolute value of the field is plotted at different frequencies: 1 GHz (solid line), 1 MHz (thick dashed line), 1 kHz (dot-dashed line) for two different variations of the conductivity. The field at 1 kHz is four orders of magnitudes smaller than at 1 GHz and the dot-dashed lines lie on the horizontal ϕ-axis (and they are not visible). The area of the curve is 2π the coupling impedance per unit length. ($b = 2$ cm, $n = 1$)

The frequency range of interest for an LHC-like case is up to a few GHz and in this range the azimuthal magnetic field is constant, while the longitudinal electric field has its maximum in the "badly" conducting region. The quantities

$$\frac{|\Delta H_\phi|}{|H_\phi|_{max}} = \frac{|H_{\phi max} - H_{\phi min}|}{|H_\phi|_{max}} \quad \text{and} \quad \frac{|\Delta E_z|}{|E_z|_{max}} = \frac{|E_{zmax} - E_{zmin}|}{|E_z|_{max}}, \tag{3.57}$$

will be small when the field is constant (over the azimuth), while they can (in principle) reach unity, when the field varies strongly with ϕ. The situation is sketched in Fig. 3.8 in a wide range of frequencies for $Y_n/Y_0 = 0.76$. The dotted regions highlight where the assumed SIBCs of Eq. (3.9) are not strictly valid. The solid line is the normalised variation of E_z

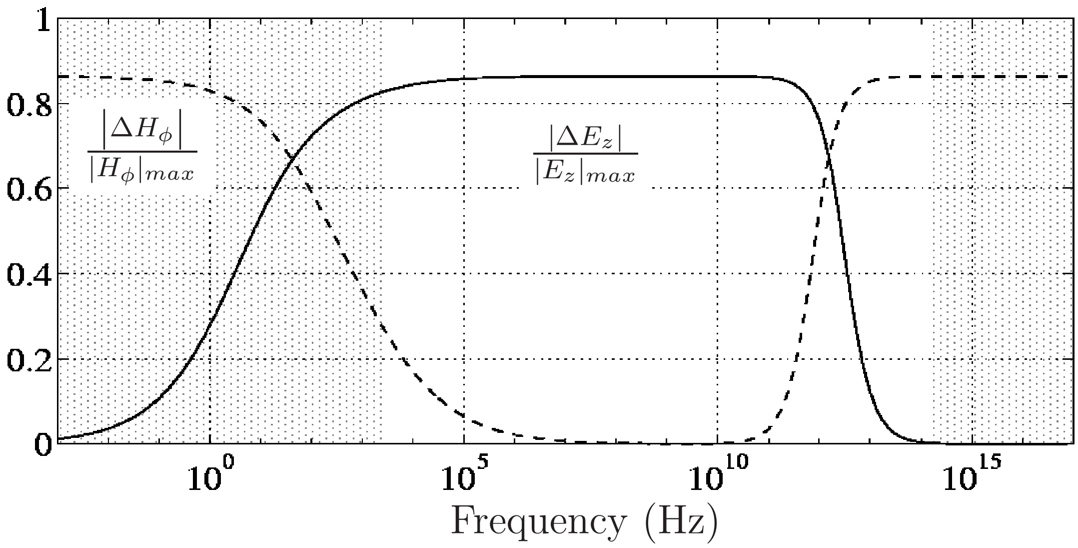

Figure 3.8: Variation of the H_ϕ and E_z on the boundary, normalised to their maximum values (on the boundary). The frequency is in logarithmic scale. In the dotted regions, the approximate boundary conditions assumed are not strictly valid. ($b = 2$ cm, $n = 1$)

while the dashed line refers to H_ϕ. The curves cross each other at two frequencies; between them the azimuthal magnetic field remains approximately constant (see Figs. 3.5, 3.7) while below the lower frequency and above the higher one, E_z is constant and H_ϕ varies with the azimuth. Such frequencies vary only a little with Y_n/Y_0; for example, keeping fixed the lower conductivity (stainless steel) and varying the maximum one from "cold" copper ($Y_n/Y_0 = 0.97$) to half of the copper conductivity at room temperature ($Y_n/Y_0 = 0.68$), the crossing frequencies remain around 100 Hz and 1 THz. The curves vary from a minimum value that is practically zero to a maximum (identical for both curves) that is 0.864 in the example of Fig. 3.8 ($Y_n/Y_0 = 0.76$). This maximum value is related to the variation in the conductivity, namely Y_n/Y_0; when the latter approaches unity, the maximum value grows (for instance it is 0.986 when $Y_n/Y_0 = 0.97$), but remains constant for both curves. Analogously when Y_n/Y_0 decreases, the plateau value decreases as well (e.g. for $Y_n/Y_0 = 0.68$ it is at 0.808). Plotting for those three cases the normalised variation of H_ϕ as a function of the normalised variation of E_z, we get Fig. 3.9. By increasing Y_n/Y_0, the curves tend to have

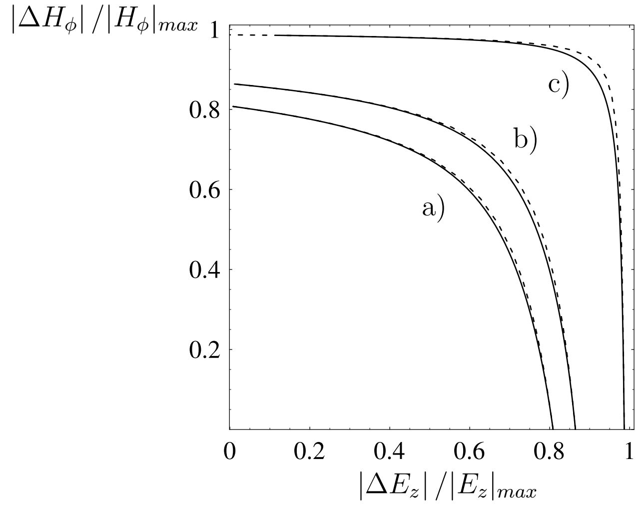

Figure 3.9: Normalised variation of the azimuthal magnetic field versus the normalised variation of the longitudinal electric field. The three sets of curves refer to different conductivity jumps: for the curves a) $Y_n/Y_0 = 0.68$, for b) $Y_n/Y_0 = 0.76$ while for c) $Y_n/Y_0 = 0.97$. Going from low frequency to higher ones, we follow clockwise the solid curves up to ≈10 GHz; then we come back in the opposite direction following the dashed curves. ($b = 2$ cm, $n = 1$)

a squared shape. The solid lines represent the path of a point going clockwise from low frequency (i.e. staring from $\Delta E = 0$ that is the y-axis) to ≈10 GHz (where $\Delta H = 0$ on the x-axis); then increasing the frequency from ≈10 GHz the points follow the dashed lines which end again on the y-axis where $\Delta E = 0$ (according to Fig. 3.8).

3.8.3 Low and high frequency regimes

We now investigate the very low and very high frequency regions, keeping in mind that they are outside (low frequencies) or very close (high frequencies) to the validity limit of the SIBCs (dotted region in Fig. 3.8). At high frequency the longitudinal electric field increases as shown in Fig. 3.10 for two different conductivities, up to ≈10 THz when it drops (dash-dotted lines). For very high frequencies (i.e. above 10 THz in our geometry), the electric field is proportional to $1/\omega$ and its value does not depend on the conductivity [15, 33]: the electric field is, indeed, constant along the azimuth ϕ (see Fig. 3.10 and the right transition of Fig. 3.8). As shown in Fig. 3.11, the azimuthal magnetic field (on the boundary) normalised to the field of a charge in the free space remains constant up to roughly 100 GHz (this value depends obviously on the geometrical dimensions chosen); for higher frequencies it

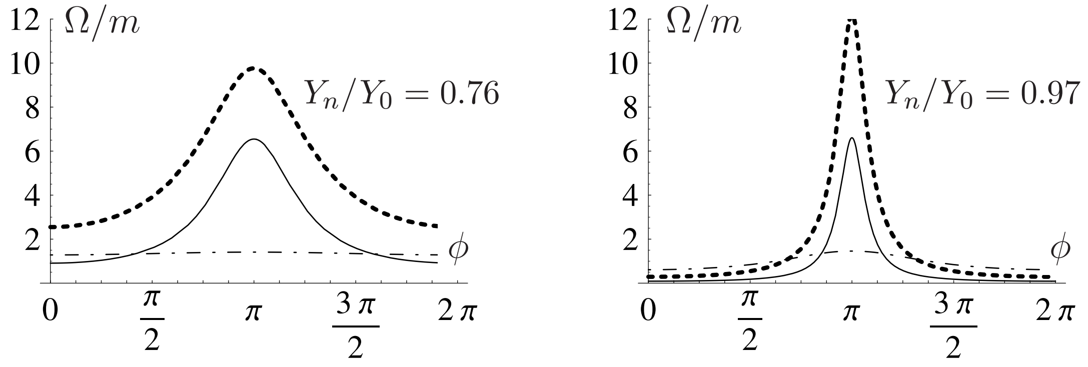

Figure 3.10: High frequency longitudinal electric field per unit charge on the boundary ($r = b$). The absolute value of the field is plotted at different frequencies: 100 GHz (solid line), 1 THz (thick dashed line), 10 THz (dot-dashed line) for two different variations of the conductivity. These frequencies are around the (right) sharp transition discussed in Fig. 3.8. ($b = 2$ cm, $n = 1$)

appears a modulation over ϕ and its value decreases (reaching zero in the limit of extremely high frequencies). It should be reminded that at so high frequency, the skin depth becomes

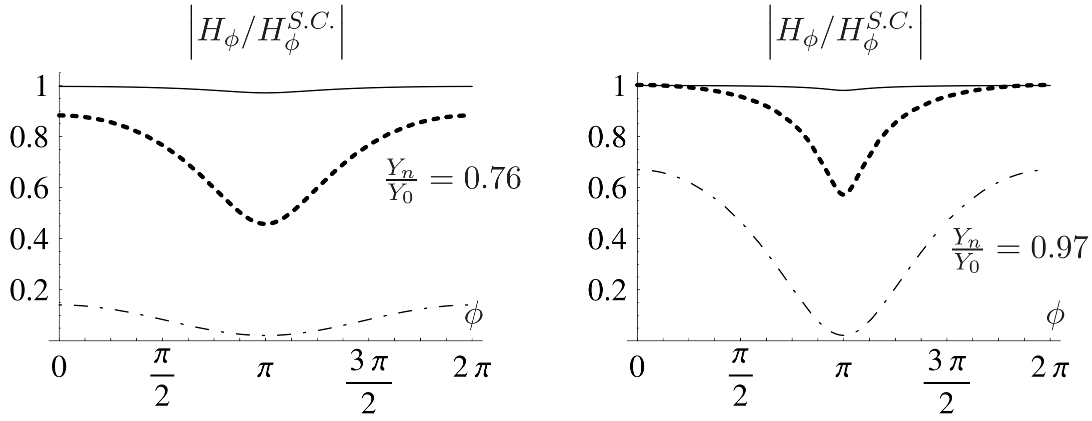

Figure 3.11: High frequency azimuthal magnetic field on the boundary ($r = b$). The absolute value of the field is plotted at different frequencies: 100 GHz (solid line), 1 THz (thick dashed line), 10 THz (dot-dashed line) for two different variations of the conductivity. These frequencies are around the (right) sharp transition discussed in Fig. 3.8. ($b = 2$ cm, $n = 1$)

comparable with the mean free path length of the conduction electrons inside the metal and the anomalous skin effect (not included in the theory) should be considered [51]. In fact for metals at cryogenic temperature (much longer mean free paths) the anomalous skin effect starts in the GHz range.

At low frequencies, the azimuthal magnetic fields presents as well a modulation with ϕ, but its average value remains more or less constant. Figure 3.12 shows its normalised absolute value for three frequencies around the low frequency crossing in Fig. 3.8, for two different conductivities. The longitudinal electric field decreases smoothly with the frequency, as

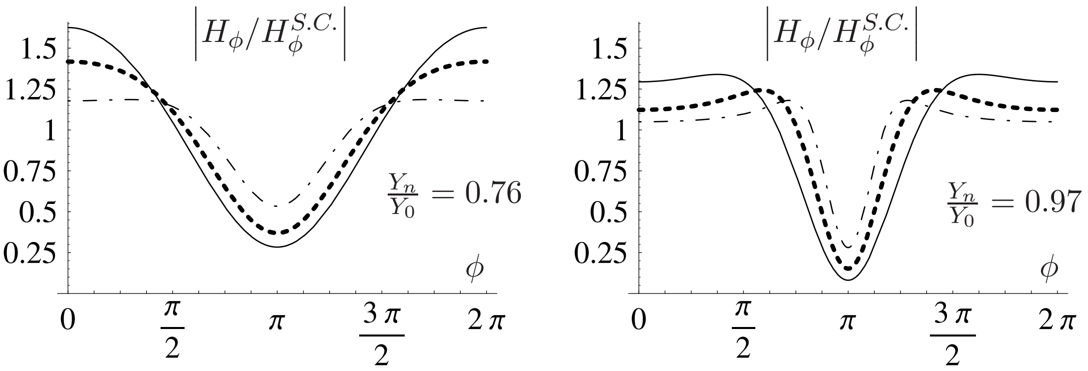

Figure 3.12: Low frequency azimuthal magnetic field on the boundary ($r = b$). The absolute value of the field is plotted at different frequencies: 1 Hz (solid line), 10 Hz (thick dashed line), 100 Hz (dot-dashed line) for two different variations of the conductivity. These frequencies (close to the left sharp transition discussed in Fig. 3.8) are outside the validity limits of the impedance boundary conditions assumed. ($b = 2$ cm, $n = 1$)

shown in Fig. 3.13.

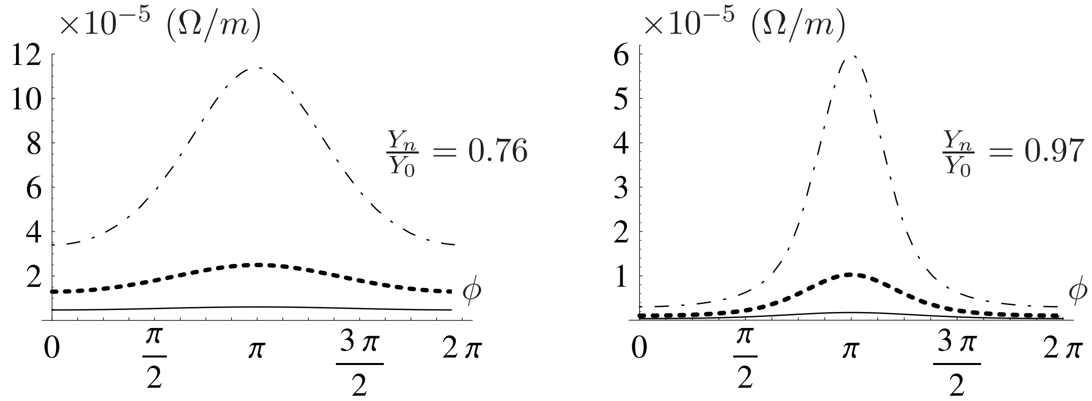

Figure 3.13: Low frequency longitudinal electric field per unit charge on the boundary ($r = b$). The absolute value of the field is plotted at different frequencies: 1 Hz (solid line), 10 Hz (thick dashed line), 100 Hz (dot-dashed line) for two different variations of the conductivity. Those frequencies (close to the left sharp transition discussed in Fig. 3.8) are outside the validity limits of the impedance boundary conditions assumed. ($b = 2$ cm, $n = 1$)

In the limit of low frequency, we expect the currents to behave consistently with Ohm's law, flowing more in the more conductive region. Denoting by I is the current flowing in the z-direction, according to Ohm's law, the current density dI/dS is proportional to $\sigma(\phi)$ (see Appendix C.5). The current density can be estimated by σE_z, computed on the pipe wall

($r = b$); in the limit of low frequency $J_z = \sigma E_z$ should have the same ϕ-dependence as dI/dS. A deeper comparison, e.g. comparing also the exact values and not only the ϕ-dependence, is non trivial since the analogy between our case (a beam travelling in a pipe with $\sigma(\phi)$) and lumped resistors in parallel is not easy to establish. To compare the ϕ-dependence, we normalise J_z and dI/dS to their maximum values (that is for $\phi = 0$). The plots are shown in Fig. 3.14 for two different values of Y_n/Y_0. The solid line is dI/dS (normalised to its maximum value), that is $\sigma(\phi)/\sigma(0)$; the dot-dashed lines are the results at 1 kHz and the dotted lines at 1 Hertz. Rigorously speaking the validity limit of SIBC is about 1 kHz (in our geometry) and lower frequencies have not to be taken too seriously. Also the skin depth at such frequencies exceeds any reasonable wall thickness for a beam pipe. Nevertheless it may be useful to check if the solution is coherent with our expectations, at least "mathematically". Moreover out of the frequency validity range, we can not rely on the values of the fields, but a ratio as $|J_z| / |J_z|_{max}$ may not be too far from reality. Figure 3.14 shows once again that the convergence is slower for higher Y_n/Y_0; in fact in the right plot the curves at 1 kHz and 1 Hertz are not distinguishable while they are well separate in the left plot. Anyway at lower frequencies, also for $Y_n/Y_0 = 0.97$ the normalised $|J_z|$ converges to $\sigma(\phi)/\sigma(0)$ (solid curves in Fig. 3.14).

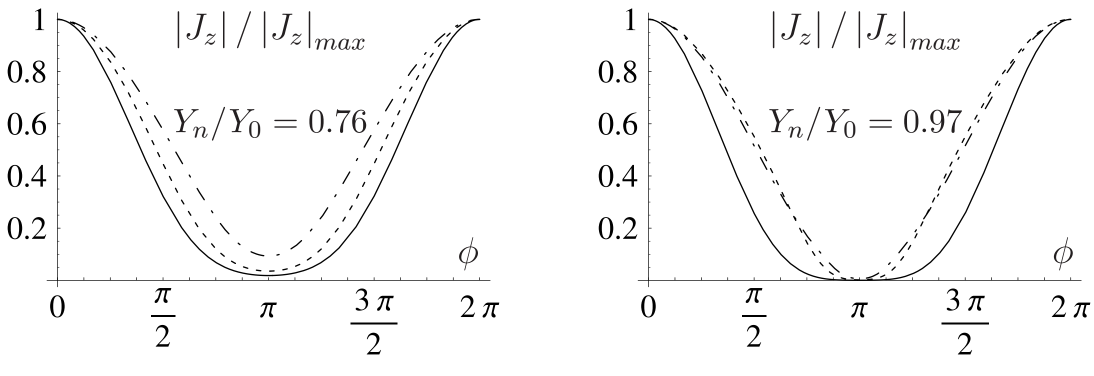

Figure 3.14: Density of the current on the pipe wall normalised to its maximum value for 1 kHz (dot-dashed line) and 1 Hertz (dashed line). The solid line is the behaviour according to the Ohm's law. Decreasing the frequency, the curves tend to Ohm's law prediction, with different rapidity depending on Y_n/Y_0. The limit of validity of the approximate boundary conditions assumed is around 1 kHz and lower frequencies are not physically meaningful, but they show that at least "mathematically" the solution behaves correctly. ($b = 2$ cm, $n = 1$)

From inspection of the results in Sec. 3.6, it is clear that the dependence on the pipe radius is always in the form kb, if we normalise the fields to the source field $H_\phi^{S.C.}$. From this statement, one can be tempted to think that by varying the radius and the frequency such that the product kb remains constant, will not change the field components. Unfortunately it is not the case since also Y_0 is frequency dependent (while the ratio Y_n/Y_0 is not) and this mixes-up everything. Nevertheless some "heuristic" results about the scaling law of the solution with b may be interesting. Varying both frequency and radius, it can be shown that for "low" frequencies the dependence on the frequency and on the radius is such that Z_0Y_0kb is constant; this means, for instance, that the azimuthal magnetic field (normalised to $H_\phi^{S.C.}$) at a frequency ω for a pipe of radius b is identical to the normalised field at $\omega/100$ in a pipe of $10b$ (since Y_0 depends on $\sqrt{\omega}$). On the contrary at high frequencies the ratio kb/Z_0Y_0 seems to be constant, meaning that the azimuthal magnetic field (normalised to $H_\phi^{S.C.}$) at a frequency ω for a pipe of radius b is equal to the normalised field at $\omega/10^{2/3}$ in a pipe of $10b$. The separation between these two regimes is (for $Y_n/Y_0 = 0.76$) around one GHz, that is exactly the most interesting region from the applications point of view and the previous ("heuristic") scaling laws are of little practical interest since they break down where they could be useful.

3.9 Other approximate solutions

Other (more) approximate solutions can be derived assuming a priori the number of ϕ-harmonics of the final results; this means that the scattered fields on the boundary in Eq. (3.31) contain only terms such that $m = n, \ldots, Tn$. This procedure is only reasonable when in the final "true" solution the high order ϕ-harmonics are negligible with respect to the harmonic of order Tn. As pointed out in the previous sections, higher values of Y_n/Y_0 imply a greater number of terms in the solution. Figure 3.15 shows, for three different values of Y_n/Y_0 (and n=1), the order $\widehat{L}$ such that for $m > \widehat{L}$ the amplitude of the m-harmonics are smaller than one tenth of the fundamental one ($m = n$) for the azimuthal magnetic field. This value is a function of the frequency and it is larger for larger variations in the conductivity. Once fixed the value Tn and derived somehow the solution, one can asses its validity by calculating $\mathcal{E}_\phi$, $\mathcal{E}_z$ given in Eq. (3.53–3.54) and verifying that they are below, for instance, 1%.

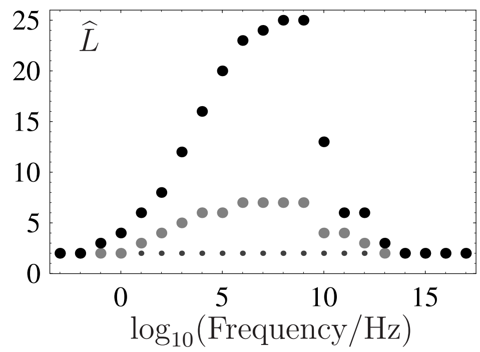

Figure 3.15: $\widehat{L}$ for different conductivities as a function of the frequency. The small black dots correspond to $Y_n/Y_0 = 0.1$ which is the case for example of a transition between brass and steel conductivities; the gray dots and the black bigger ones are the usual cases of $Y_n/Y_0 = 0.76$ and $Y_n/Y_0 = 0.97$ respectively. On the x-axis is reported the logarithm in base 10 of the frequency in Hz. ($b = 2$ cm, $n = 1$)

In the following we compare the "exact" solution of the previous section with other two approaches. The first one, called "analytical" solution, is obtained by assuming a priori the number of relevant ϕ-harmonics and then solving analytically the resulting system. On the contrary, the "perturbative" solution assumes that the magnetic field on the boundary is identical to the field of a beam in the free space.

The analytical solution for $T \leq 3$ can be found with a reasonably small effort with *Mathematica* for any value of β (providing that $kb/\beta\gamma \ll 1$ in order to simplify the Bessel functions) and the results are presented in Figs. 3.16–3.17 for $Y_n/Y_0 = 0.76$ and high β. The approximate field (red lines) is compared with the previous "exact" solution (green lines): the electric field agrees quite well at low and at high frequency, while the azimuthal magnetic field is quite different at low frequencies (note the different scales of the figures). Obviously these fields do not fulfil the boundary conditions. Nevertheless the solution is not far from the "real" one, at least in the GHz range (where the H_ϕ is constant with the azimuth). Decreasing the relativistic β the behaviour doesn't change significantly, at least in the GHz range, as shown if Fig. 3.18, where the field at low β (solid red curves) behave similarly to the $\beta \to 1$ case.

Another reasonable approach to obtain a simplified solution is the perturbative one: to first order the azimuthal magnetic field on the boundary is equal to the the field of the charge in the perfectly conducting pipe ($H_\phi^{S.C.}$). Then from the SIBC of Eq. (3.9), the longitudinal

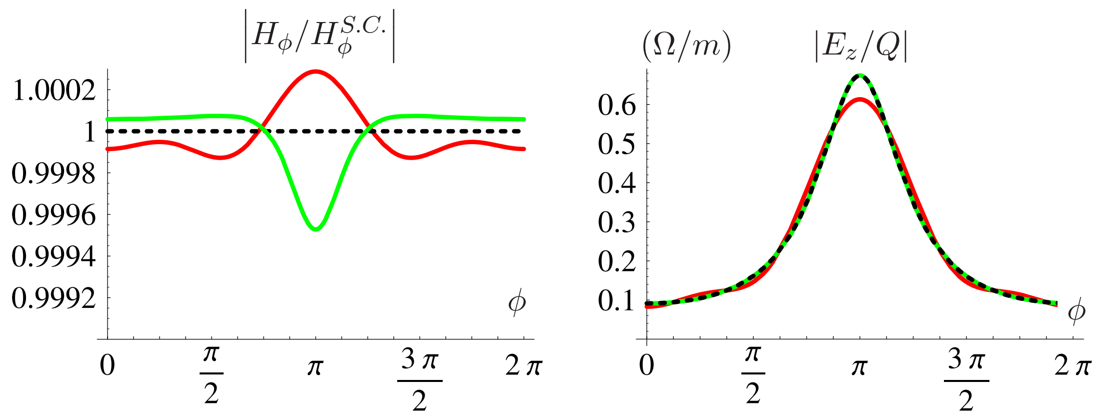

Figure 3.16: Azimuthal magnetic field and longitudinal electric field on the boundary at 1 GHz. The dashed black line is the result of the perturbative approach. The red line is an analytical solution including only the first three ϕ-harmonics for β=0.999999 and the green one is the "exact" solution. The three solutions are very similar. ($b = 2$ cm, $n = 1$)

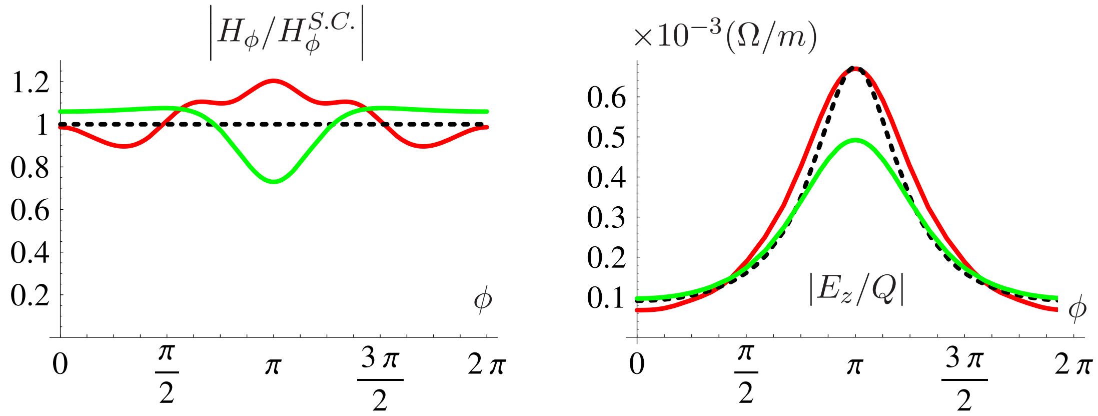

Figure 3.17: Azimuthal magnetic field and longitudinal electric field on the boundary at 1 kHz. The dashed black line is the result of the perturbative approach. The red line is an analytical solution including only the first three ϕ-harmonics for β=0.999999 and the green one is the "exact" solution. ($b = 2$ cm, $n = 1$)

electric field is $E_z \approx ZH_\phi^{S.C.}$; the results are plotted in Figs. 3.16–3.17 (black dashed lines). The agreement is good at high frequency, when the azimuthal magnetic field is actually constant. One can use the previous statement as a first step of an iterative solution; anyway to get the "correct" value of the H_ϕ one has to make many iterations and the final solution has a complexity analogous to our solution.

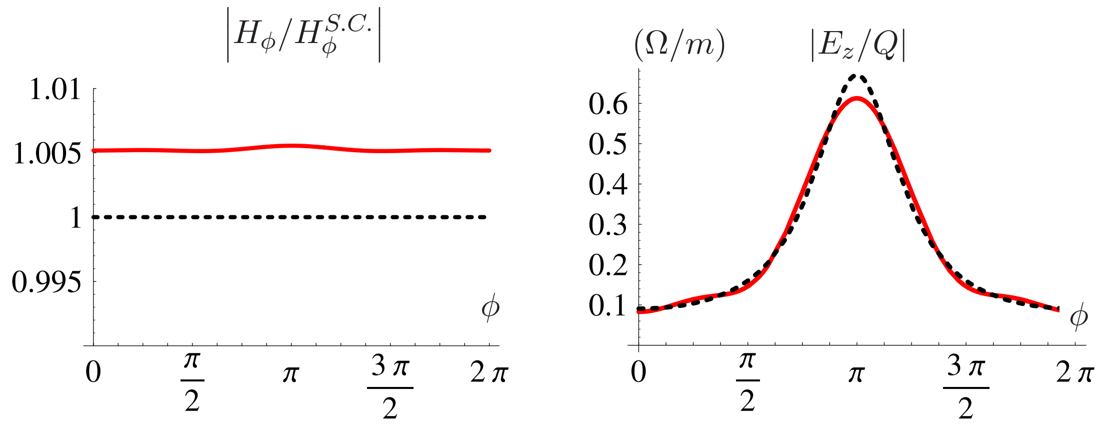

Figure 3.18: Azimuthal magnetic field and longitudinal electric field on the boundary at 1 GHz for $\beta = 0.99$. The dashed black line is the result of the perturbative approach. The red line is an analytical solution including only the first three terms. ($b = 2$ cm, $n = 1$)

3.10 Numerical simulations with HFSS

In the design of accelerator components, it is becoming nowadays a common practise to use general purpose electromagnetic fields simulators such as the High Frequency Structure Simulator (HFSS) [52]. As in most of the general purpose simulators, it is not possible to include directly the beam in the numerical simulation and we are forced to use the coaxial wire method. In fact, there is an analogy between the effects of a given structure on a particle beam and the properties of the coaxial transmission-line obtained by inserting a metallic wire on the axis of the structure itself. This analogy, first developed in 1974 [53], is now widely used in a number of different situations and the coaxial wire method is one of the most common bench measurements to estimate the energy lost by a particle going through an accelerator component. From then, the theory of the wire method has been improved and it can now be applied in many different situations (see for instance [54]). One of the appealing features of simulating the wire method is therefore the direct relation with the bench measurement.

In our case, the simulated structure is sketched in Fig. 3.19; it is a cylindrical pipe (yellow) with a metallic wire in the middle (blue line); its longitudinal length is chosen to be equal to the wavelength λ (that is 30 cm in our case). The radius of the pipe is 4 cm, while the radius of the wire is 2 mm; the smaller is the radius of the wire, the more the coaxial line resembles the situation seen by a pencil beam. In practice the wire can not be too small in order to get a clear signal (both in the simulations and in the real bench measurements). The relation between the radii and the frequency of the simulation (or measurement) is such that only the TEM wave is propagating in the structure (the cut-off frequency of the TE_{11} for this set-up is, in fact, about 2 GHz). To reduce the computation time, only half of structure is simulated. Figure 3.19 shows, as well, a density plot of the electric field on the symmetry plane: the red regions corresponds to maximum field, while the field is low in the blue (and darker green) ones.

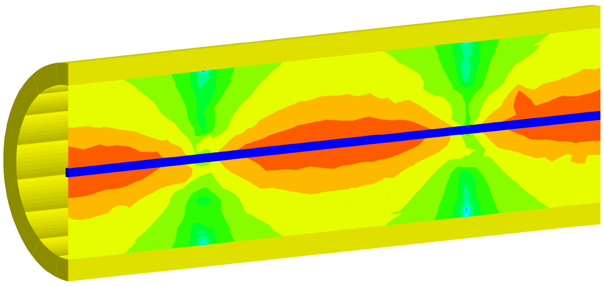

Figure 3.19: Geometry used in the HFSS simulation and density plot of the magnitude of the electric field on the symmetry plane. The pipe (yellow) radius is 4 cm while the wire radius is 2 mm (blue line). The magnitude of the electric field has two maxima over the longitudinal extension, since the structure is long λ. The assigned power flowing into the coaxial transmission line is 1 Watt and it flows from one end of the structure to the other. Only one mode is included in the simulations.

To mimic as much as possible the situation studied in the previous sections, the pipe is made of nine pieces of different conductivities, chosen according to Fig. 3.20 (left plot) and going from the usual copper conductivity at $\phi = 0$ to the stainless steel one at $\phi = \pi$ (only half of the structure is simulated).

In order to simulate half of the structure, HFSS allows the use of symmetry planes which can be "electric" (perfect E symmetry condition) or "magnetic" (perfect H symmetry condition). The former are used whenever the electric field is normal to the symmetry plane and the latter if the magnetic field is normal. In our solution the symmetry plane cuts the slices corresponding to the minimum and the maximum conductivity. It can be shown (directly from the uniqueness of the solution of Maxwell's equations) that if the conductivity is constant in a finite angular region, e.g. for $\phi \in [-\theta, \theta]$, then H_r and H_z is null in the middle of such region (namely for $\phi = 0$). Therefore the use of a perfect H symmetry plane cutting the geometry at $\phi = 0$ (and $\phi = \pi$) is justified. When using a symmetry plane the magnitude of the sources has to be scaled accordingly and HFSS foresees an impedance multiplier that is the ratio between the simulated angle and 2π, in the case of a perfect H symmetry (for electric planes the impedance multiplier is the inverse).

To refine the calculation, we have used the manual meshing option, including 60000 tetrahedrons; more than one half of them are concentrated in a cylindrical corona 5 mm wide (from the metal surface), since we are interested mainly in the field next to the boundary. The RMS value of the longer sides of these tetrahedrons is about 10 mm in the meshing eventually used in the solution. Including a larger number (about one third more) of mesh points is time consuming and does not improve the RMS values of the longer tetrahedrons sides (while it reduces the difference between the minimum and the maximum side length).

The resulting H_ϕ on the boundary (it is calculated on a line of $r = 39.8$ mm instead of 40 mm) is given in Fig. 3.20 (right plot). The power flowing in the coaxial-line is 1 W (default value) and the power assigned to the port is scaled by the impedance multiplier. To

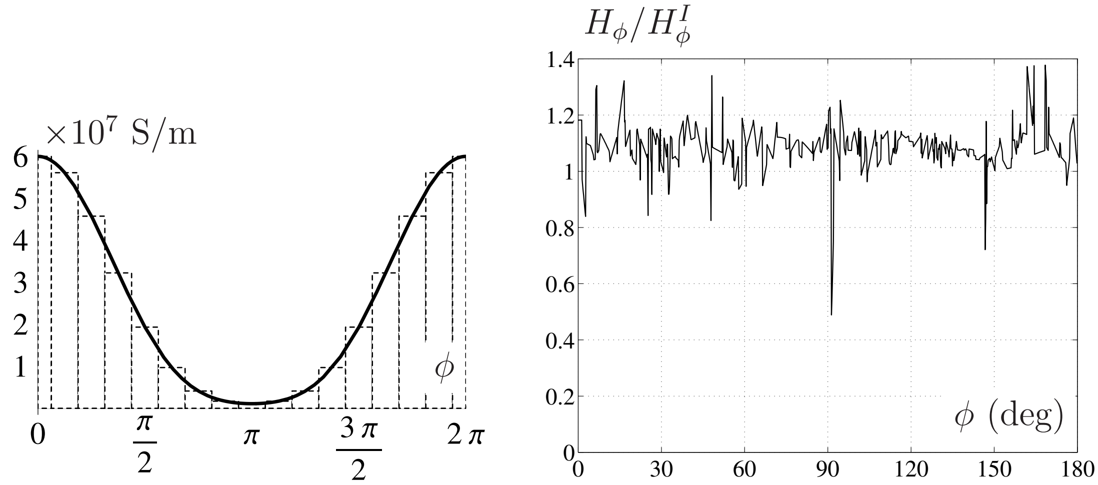

Figure 3.20: Behaviour of the conductivity used in the simulation (left plot) and resulting H_ϕ (real part) normalised by the field in a coaxial line feeded with the same amount of power (right plot).

relate the power flowing in the coaxial line to the current I, we remind that for the TEM mode (the only propagating one) the power P is easily obtained from the Poynting vector as

$$P = \frac{1}{2} \int E_r H_\phi dV = I^2 \frac{Z_0}{4\pi} \ln \left(\frac{r_{max}}{r_{min}} \right) \quad \text{since} \quad E_r = Z_0 H_\phi = Z_0 \frac{I}{2\pi r}; \tag{3.58}$$

r_{max} is the outer radius (40 mm) while r_{min} is the wire radius (2 mm). The previous relation allows us to calculate the current I from the knowledge of the power P that is flowing. The magnetic field (real part) in Fig. 3.20 is normalised to H_ϕ^I, the field generated at the radius r by the current I. The field is constant along the azimuth as predicted from the theory. The result is a bit noisy and increasing the number of tetrahedrons by about one third, it doesn't improve; the reason may be that the geometry is anyway very big and in order to have more precise simulations we have to take smaller slices (which is not possible if we want to simulate the conductivity in Fig. 3.20). The value of the normalised field should be unity; the small difference observed can be explained by the uncertainty on the value of the radius of the wire (used in Eq. (3.58)), which is so small that it is comparable with the size of the meshes close to it. For numerical convergence reasons also HFSS assumes (by default) the SIBCs of Eq. (3.9) in order not to solve for the field inside the conductors; in fact calculating the field in the conductor would need a mesh dimension smaller that the skin depth (that is microns) and thus a number of mesh points too big for any practical use.

To achieve more accurate results, we can simulate smaller angular slices of a pipe made, for example, of two different materials. Taking a 90 degree slice of a pipe made of stainless steel and a perfect conductor (using copper the result doesn't change), we get for the magnetic field on the boundary the pattern shown in Fig. 3.21 (left plot), where it is clear that it is purely azimuthal. The frequency is the same, but the model is twice longer. The azimuthal magnetic field versus z-axis is also shown and compared to H_z, which is practically zero.

3.11 Measurements

The previous theory predicts a constant magnetic field over the azimuth when the beam pipe is made of different metals. Numerical simulations confirm this result and to eventually asses its validity, an experimental study has been performed. A cylindrical pipe made of 12 different bars which can be mounted and dismounted within a reasonable mechanical precision, has been designed and built (see Fig. 3.22). Each bar is "identical" to the others in shape, so that they can be interchanged; they are kept in place by the external ring (light blue big ring in Fig. 3.22) and by the screws. The violet (cylindrical) separators were meant to fix the position every second bar with respect to the external reference ring. A mechanically

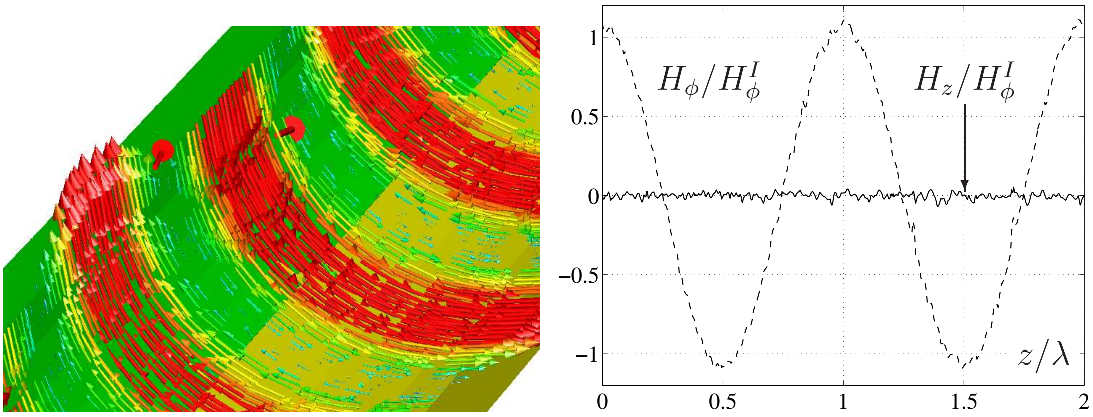

Figure 3.21: Magnetic field on the boundary (left plot) and H_ϕ (dashed line) and H_z (solid line) along the z-axis and normalised to the field in a perfect coaxial line fed with the same power (right plot). The green part is a perfect conductor while the yellow one is stainless steel (50000 tetrahedrons are used).

precise realisation of this separators was not practical and the distance between two opposite bars is fixed (to 5 cm) by using external metallic pieces as reference (not shown). There are four of such rings, since the entire structure is 70 cm long (see Fig. 3.23); for practical reasons it is mounted on the (heavy) support shown in Fig. 3.23. The bars are available in two sets, one set of 12 steel bars (bad conductor) and one set of 12 brass bars (good conductor). The prototype is versatile and can be mounted in all possible combinations, from all brass bars to all steel bars. For instance in Fig. 3.22, the pipe is mounted using 6 brass bars (yellow ones) and 6 steel bars (grey ones) alternatively.

To make precise, reliable and meaningful bench measurements, the pipe has been transformed into a TEM resonator by inserting a cylindrical tube (silver-plated stainless steel) along the axis of the structure; the inner cylinder is kept in the right position by proper Teflon supports (see Fig. 3.23, lower right photo). The diameter of the silver-plated tube is 1 cm and its length is 50 cm; it is chosen of stainless steel to ensure mechanical stability and it is silver plated to reduce ohmic losses. The coupling circuit is shown in Fig. 3.23 (lower left); the little disk on the edge of the electrode increases the coupling capacity, giving stability to the resonance frequency with respect to the positioning of the coupling circuit.

The Q-factor measured with a network analyser (an HP8753D in our case) depends on the coupling network and on the real Q-factor of the TEM resonator, which eventually we

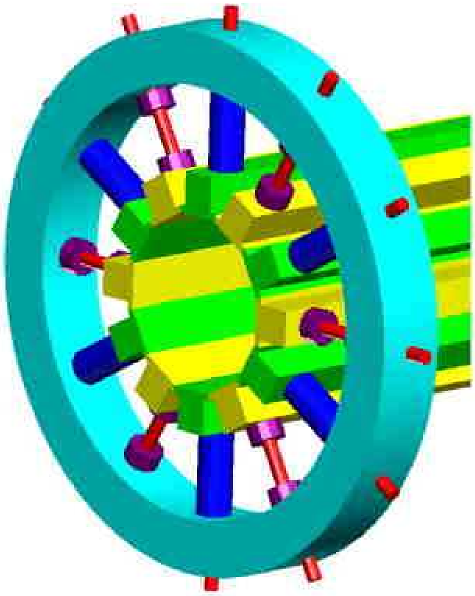

Figure 3.22: Prototype used in the measurements. The left figure represents the project, while the right photo is the realised prototype. The cylindrical pipe is made of 12 bars of two different materials (brass and steel). The bars are "identical" and they can be mounted in different configurations, to simulate different azimuthal behaviours of the conductivity.

want to measure (Q_{unload}). It can be shown [56] that in transmission type measurements, for symmetrical coupling

$$Q_{unload} = \frac{Q_{load}}{1 - S_{12}(f_0)}, \tag{3.59}$$

where Q_{load} is the Q-factor read directly from the network analyser display (when set in "automatic Q measure" configuration). The $S_{12}(f_0)$ is the transmission coefficient S_{12} at the resonance frequency f_0; usually the magnitude of $S_{12}(f_0)$ is expressed in decibels and called "insertion loss" α_L (that is the "Loss" reading of the network analyser display). Because $S_{12}(f_0)$ is always smaller than unity, α_L is a negative number[2]. To compute $S_{12}(f_0)$, we simply need to convert α_L from decibels, that is

$$S_{12}(f_0) = 10^{\alpha_L/20}. \tag{3.60}$$

It is worth mentioning that the measured α_L depends also on the cable losses and a (transmission) calibration is needed. One could either calibrate directly the instrument or simply

[2]In some literature the insertion loss is defined with the opposite sign, so that a positive value represents losses while a negative value means "gain"; with this convention a minus sign should appear in the exponent of Eq. (3.60). On the contrary in our case, losses are taken into account by a negative α_L, according to the reading on the network analyser display.

Figure 3.23: Q-factor measurements set-up. The upper image shows the pipe connected to a network analyser to measure (in transmission) the Q-factor of the TEM resonator obtained inserting a silver-plated steel tube along the axis of the pipe (lower right photo). The bar is kept in the centre by proper (white) Teflon supports which are perforated to perturb as little as possible. The left lower photo represents (next to a matches box) one of the two identical coupling electrodes.

measure the amount of losses due to the used cables and then subtract them off-line from the read "Loss" (and we use the second way). The accuracy of Eq. (3.59) is seriously reduced when the ratio of the power dissipated on the coupling circuit to the power dissipated in the resonator is small with respect to unity. This happens because $S_{12}(f_0)$ approaches unity ($\alpha_L \rightarrow 0$ db) when the coupling is strong and the denominator of Eq. (3.59) becomes a difference of two almost equal numbers, so that even small errors in $S_{12}(f_0)$ will cause a large error in Q_{unload}.

The validity of Eq. (3.59) requires also that the couplings at the two ports be symmetrical. This can be "electrically" checked by measuring the reflection parameters S_{11} and S_{22}. The distance between the disk and the brass cylindrical plugs is fixed and equal for the two couplers. Moving back (forward) the couplers, the corresponding reflection S-parameter will decrease (increase). The symmetrical coupling is ensured when, in a given frequency span around the resonance frequency, the S_{11} and S_{22} curves are identical, as shown in Fig. 3.24 for the two frequencies at which we will perform the measurements. The left plot refers

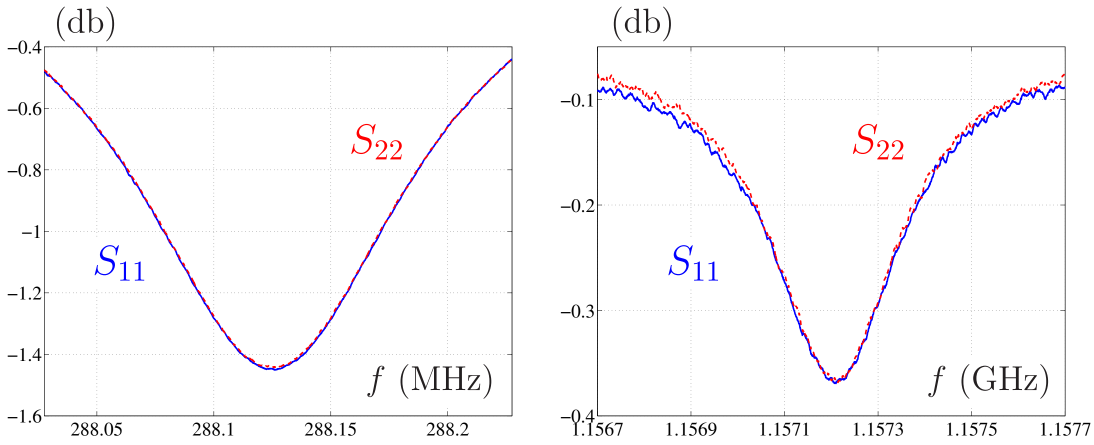

Figure 3.24: S_{11} (blue solid line) and S_{22} (red dashed line) for a typical Q-factor measurement. The left plot refers to the resonance at 288 MHz while the right plot refers to the resonance at 1.1157 GHz. The couplers are positioned such that $S_{11} = S_{22}$ in a frequency range of 200 kHz and 1 MHz respectively. The difference between the reference values in the network analyser data is neglected (it is anyway small because of the calibration). For the lower frequency measurement an Intermediate Frequency (IF) of 100 Hz is used, while for the higher frequency the IF value is 30 Hz. In those plots only the frequency span relevant to check $S_{11} = S_{22}$ is shown.

to the resonance at 288 MHz and the frequency span in which we seek the identity of S_{11} and S_{22} is 200 kHz; the right plot refers to the resonance at 1.16 GHz and the frequency span is of 1 MHz. To carefully verify the identity of S_{11} and S_{22}, the two channels of the network analyser are calibrated [3] for reflection measurements on the two ports (one port on each instrument channel). A narrow frequency calibration is only needed and for the lower frequency is used a calibration in a range of 2 MHz around 288 MHz, while for the higher frequency the calibrated range is of 10 MHz around 1.16 GHz. Therefore, a typical Q-factor measurement for a given configuration of the bars consists of the following steps:

i. Adjust the distance between the couplers and the inner conductor such that the maximum variation of S_{11} and S_{22} on a given frequency span (that is 200 kHz for the resonance at 288 MHz and 1 MHz for the resonance at 1.16 GHz) has a predefined value.

[3] The calibration is the so called "full one port calibration" (open circuit, short circuit and 50 Ohm load).

ii. Record the Q-factor value (that is Q_{load}), the "loss" value α_L and the resonance frequency f_0.

iii. Use Eq. (3.59) to compute off-line the Q_{unload}.

iv. Repeat this procedure for several of maximum variations of the reflection parameters (for instance 0.1 db, 0.3 db, 0.5 db, 0.7 db, 0.9 db and 1.1 db), as explained in the first point. The resulting Q_{unload} should be constant.

Such a procedure gives very precise results for the Q_{unload}, as shown in Table 3.1 where the Q values of the resonator with only brass bars are reported for different couplings and for two different frequencies. It is worth remarking that Eq. (3.59) can be safely used since α_L is far from 0 db.

	Lower frequency				Higher frequency			
(db)	f_0 (MHz)	Q_{load}	α_L (db)	Q_{unload}	f_0 (MHz)	Q_{load}	α_L (db)	Q_{unload}
0.1	288.376	2936	-37.795	2974	1157.200	5745	-38.719	5812
0.3	288.330	2857	-28.028	2975	1157.180	5620	-29.696	5810
0.5	288.285	2778	-23.529	2976	1157.160	5479	-24.956	5807
0.7	288.241	2705	-20.917	2972	1157.142	5360	-22.328	5804
0.9	288.195	2632	-18.761	2975	1157.125	5246	-20.347	5804
1.1	288.148	2561	-17.191	2972	1157.107	5104	-18.417	5800

Table 3.1: Measurements of the Q-factor (only brass bars) for different couplings. The first column is the maximum variation of the $S_{11} = S_{22}$ on a given frequency span around f_0 (200 kHz for the lower f_0 and 1 MHz for the higher one). The insertion loss α_L is $S_{12}(f_0)$ expressed in db and the coupling is not at all critical since $S_{12}(f_0)$ is $\ll$1.

The theory presented in the previous sections predicts a constant azimuthal magnetic field along the pipe circumference; thus changing a good conducting bar (i.e. a brass bar) with a steel bar (which is a worse conductor) will increase the losses in the resonator, since the current on the wall remains constant but it flows along a more resistive path. Eventually a decrease of the Q-factor (the unloaded one), should be observed.

A number of measurements has been performed replacing brass bars with steel ones. In the following, when referring to Q-factors we will always mean Q_{unload}; to distinguish between different set-ups we introduce a suffix indicating the number of steel bars mounted.

For instance Q_1 is the (unloaded) Q-factor measured with 1 bar of steel (surrounded by the remaining 11 bars of brass) and Q_N refers to the prototype when N steel bars and $(12 - N)$ brass bars are mounted. Thus, the previous Table 3.1 refers to measurements of Q_0 (all brass) while the situation with only steel bars would be Q_{12}. Typical measured values for Q_0, Q_1, Q_2, Q_3 are reported in Table 3.2. The Q-factors shown are unloaded ones, but they are still reported as a function of the coupling at which the corresponding Q_{load} has been measured.

In the following we assume as a measure of the Q_i, simply the average of the unloaded Q-factors obtained from data taken with different couplings. The deviation from the arithmetic mean $\overline{Q}$ is quite small (especially compared to other sources of errors) and in all the coming measurements we take only three samples of Q-data for each set-up (as shown for Q_3 in Table 3.2). According to [57], the uncertainty (of a measurement) is a parameter associated

	Lower frequency (288 MHz)				Higher frequency (1.16 GHz)			
	Q_0	Q_1	Q_2	Q_3	Q_0	Q_1	Q_2	Q_3
0.1 db	2974	2134	1866	1442	5812	4381	3860	3058
0.3 db	2975	2132	1862		5810	4373	3857	
0.5 db	2976	2131	1860	1440	5807	4372	3854	3056
0.7 db	2972	2132	1860		5804	4370	3854	
0.9 db	2975	2130	1861	1438	5804	4360	3856	3061
1.1 db	2972	2130	1859		5800	4361	3857	
$\overline{Q}$	2974	2131	1861	1440	5806	4370	3856	3058
$u(Q)$	0.72	0.61	1.02	1.15	1.88	3.31	0.83	1.45
$u(Q)/\overline{Q}$ (%)	0.02	0.03	0.05	0.08	0.03	0.08	0.02	0.05

Table 3.2: Measurements of the unloaded Q-factor Q_0, Q_1, Q_2, Q_3 for different couplings. The first column is the maximum variation of the $S_{11} = S_{22}$ on a given frequency span around f_0 (200 kHz for the lower f_0 and 1 MHz for the higher one): the unloaded Q should be independent from this. The average value, the uncertainty and the relative uncertainty are reported in the last three lines.

with the result of a measurement that characterises the dispersion of the values that could reasonably be attributed to the measurand. The variance of the arithmetic mean (or average of the observations), rather than the variance of the individual observations, is the proper measure of the uncertainty u of a measurement result [58]; such a variance can be estimated with the experimental standard deviation of the mean and thus

$$u(Q_i) = \sqrt{\frac{1}{L(L-1)} \sum_{j=1}^{L} \left(Q_{i,j} - \overline{Q}_i\right)^2}, \tag{3.61}$$

where $Q_{i,j}$ is one of the L realisations of the measurement of Q_i. The last three rows in Table 3.2 report the average, the uncertainty and the relative uncertainty for a typical measurement of Q_0, Q_1, Q_2, Q_3.

Intuitively, the data of Table 3.2 confirm the constant azimuthal magnetic field, since $Q_0 > Q_1 > Q_2 > Q_3$. The comparison between these Q values is meaningful only if the mechanical tolerances are so small that mounting different bars will not change substantially the geometry (within the accuracy of a Q-factor measurement). This is very difficult to achieve and the mounting/dismounting tolerances are the main source of measurement errors. Anyway it should be stressed that more "expensive" solutions, as for example comparing many identical pipes with different behaviour of the resistivity of the internal surfaces, would introduce other uncertainties on the properties of the internal layers and the real equivalence of the different prototypes may be questionable.

In order to estimate the effect of mounting/dismounting tolerances, one way is to measure in different configurations which should be "electrically" identical (for instance a single bar in different azimuthal positions). Each value of Q_i for a given set-up is the average over (at least) three samples, as shown in Table 3.2 and the presently acquired data are reported in Table 3.3, for two different frequencies. The measurements are presently done mounting up to three steel bars (while the others are brass bars); to distinguish among the three different steel bars they are labelled ("bar 1", "bar 2", "bar 3") and we refer to the Q-factor measured with all brass except the steel "bar j" ($j = 1, \dots, 3$) as Q_1^j. This sorting is necessary for the steel bars (and not for the brass bars) because they may differ both geometrically and in their surface properties, owing to thin layers of rust deposited. The first five columns of data in Table 3.3 represent respectively independent measurements of Q_0, Q_1^j ($j = 1, \dots, 3$), Q_2, Q_3 (the two bars together for Q_2 are "bar 1" and "bar 2"). The effect of the mechanical imperfections (i.e. the bars are not geometrically identical) is evident.

The previous reasonings allow to establish a "qualitative" agreement between the theoretical expectations and the measured data. A more precise (and "quantitative") comparison is

	Independent measurements					$\overline{Q}$	$u(Q)$	$u(Q)/\overline{Q}$ (%)
Q_0	2975	2970	2972	2974		**2973**	**1.24**	0.04
Q_1^1	2132	2189	2266	2198		**2196**	**27.52**	1.25
Q_1^2	2153	2237	2300			**2230**	**42.44**	1.90
Q_1^3	2229	2149	2209			**2196**	**24.04**	1.09
Q_2	1756	1773	1692	1787	1713	**1744**	**18.11**	1.04
Q_3	1440	1479	1459			**1459**	**11.35**	0.78

Q_0	5808	5808	5809	5820		**5811**	**2.99**	0.05
Q_1^1	4371	4477	4593	4485		**4482**	**45.35**	1.01
Q_1^2	4422	4547	4631			**4533**	**60.79**	1.34
Q_1^3	4527	4391	4474			**4464**	**39.58**	0.89
Q_2	3679	3722	3573	3720	3594	**3658**	**31.29**	0.86
Q_3	3059	3124	3104			**3096**	**19.08**	0.62

Table 3.3: Measurements of the unloaded Q-factor Q_0, Q_1, Q_2, Q_3 for different (but electrically analogous) situations at the two measured frequencies 288 MHz (upper table) and 1.16 GHz (lower table). Q_1^j ($j = 1, \ldots, 3$) is the Q-factor of the resonator when only the steel bar j is mounted (among brass bars) The measured data are shown in the first five columns, while the last three ones report the average value $\overline{Q}$, the uncertainty $u(Q)$ and the relative uncertainty $u(Q)/\overline{Q}$.

indeed possible. In fact, if the azimuthal magnetic field is constant along the circumference, the power loss inside our cavity will be simply the sum of the power dissipated in the inner conductor (P_{inner}) and the power dissipated in each of the 12 bars making up the pipe. Denoting P^{brass} the power dissipated on a generic brass bar and P_j^{steel} the power dissipated on the steel bar j,

$$P_0 = P_{inner} + 12P^{brass} \quad \text{and} \quad P_N = P_{inner} + (12 - N)P^{brass} + \sum_{j=1}^{N} P_j^{steel} \tag{3.62}$$

where P_0 and P_N are the power loss when the pipe is made of all brass bars (“0” steel bars) and when there are N steel bars respectively. Again, we are considering only differences among the steel bars (while the brass ones are treated as identical), for the reasons discussed above. The difference $P_0 - P_N$ is independent from the power dissipated in the inner conductor, i.e.

$$P_0 - P_N = \sum_{j=1}^{N} (P^{brass} - P_j^{steel}) = \sum_{j=1}^{N} (P_0 - P_1^j), \tag{3.63}$$

where P_j^{steel} is always fraction of the power loss on the steel bar j, while P_1^j is the power loss in all the cavity when there is one steel bar (namely the "bar j") and all the others are brass ones. Equation (3.63) is appealing because P_0, P_N, P_1^j can be measured easily. In fact the Q-factor of a cavity is

$$Q = 2\pi f_0 \frac{W}{P},$$

where f_0 is the resonance frequency, P the power loss and W the electromagnetic energy stored in the cavity. Assuming that f_0 and W remain "approximately" constant when changing one bar with another, then Eq. (3.63) becomes

$$\frac{Q_0 - Q_N}{Q_N} \approx \sum_{j=1}^{N} \frac{Q_0 - Q_1^j}{Q_1^j} \tag{3.64}$$

where the meaning of the symbols was given above (see Table 3.3). The resonance frequency remains more or less constant in any configuration as it can be verified during the measurements. The stored electromagnetic energy can also be considered constant (in a first approximation) provided that we refer to the energy stored really inside the cavity, independently of the coupling circuit; thus Eq. (3.64) holds only if referred to the unloaded Q-factors (calculated before).

Therefore, to check the theoretical prediction of a constant magnetic field over the azimuth, we need to measure Q_0, Q_N and Q_1^j and verify if the equality in Eq. (3.64) is satisfied. Equation (3.64) is appealing because it is independent of the values of P_{inner} and even of the electrical properties of the single "bar j" (provided that we measure Q_1^j and Q_N)[4]. The drawback is that we have to make at least four measurements (Q_0, Q_2, Q_1^1, Q_1^2) and then compare them. The result is prone to be affected by the mechanical tolerances which enters whenever we dismount a bar to substitute it with another one; an estimation of these effect was discussed in Table 3.3.

In conclusion, mechanical tolerances are mainly responsible for our measurement uncertainty; to estimate it, a number of Q-factor measurements in different (but electrically analogous) situations has been performed. The effect of the measurement uncertainty on the

[4]This is very relevant for the steel bars because the steel has also magnetic properties ($\mu_r \neq 0$) which can not be easily estimated at the measurement frequency. In fact in our set-up, we used (for convenience) the kind of steel used in civil construction and its magnetic properties are not reported in the data–sheets.

identity of Eq. (3.64) can be taken into account by the "law of propagation of the uncertainty" (see [58], pag. 19), as follows. For convenience we label the LHS and RHS of Eq. (3.64) as f and g, respectively. The dispersion of the values that could reasonably be attributed to the measurands f and g is characterised by the "combined uncertainty" $u_c(f)$ and $u_c(g)$ respectively, which can be obtained by appropriately combining the uncertainties of the quantities involved in the definition of f and g. Therefore, Eq. (3.64) results in comparing $\overline{f}$ and $\overline{g}$ with the proper uncertainties, being

$$\overline{f} = \frac{\overline{Q}_0 - \overline{Q}_N}{\overline{Q}_N} \quad \text{with} \quad u_c(f) = \frac{\overline{Q}_0}{\overline{Q}_N}\sqrt{\left[\frac{u\left(Q_0\right)}{\overline{Q}_0}\right]^2 + \left[\frac{u\left(Q_N\right)}{\overline{Q}_N}\right]^2}, \tag{3.65a}$$

$$\overline{g} = \sum_{j=1}^{N} \frac{\overline{Q}_0 - \overline{Q}_1^j}{\overline{Q}_1^j} \quad \text{with} \quad u_c(g) = \sqrt{\left[\sum_{j=1}^{N} \frac{u\left(Q_0^j\right)}{\overline{Q}_1^j}\right]^2 + \sum_{j=1}^{N}\left(\frac{\overline{Q}_0}{\overline{Q}_1^j}\right)^2 \left[\frac{u\left(Q_1^j\right)}{\overline{Q}_1^j}\right]^2}, \tag{3.65b}$$

since Q_0, Q_N, Q_1^j $(j = 1, \ldots, N)$ are independent quantities.

Applying Eqs. (3.65) to the available measurements (Table 3.3), the results are in significant agreement with the theoretical expectations. The bold values in Table 3.4 representing the LHS and RHS of the identity (3.64) are very close and their relative uncertainty is smaller than 5%. In conclusion, the theoretical result of a constant magnetic field on the metallic pipe is confirmed within the measurement uncertainty.

	$\overline{f} = (\overline{Q}_0 - \overline{Q}_N)/\overline{Q}_N$	$u_c(f)$	$\overline{g} = \sum_{j=1}^{N}(\overline{Q}_0 - \overline{Q}_1^j)/\overline{Q}_1^j$	$u_c(g)$
2 steel bars @ 288 MHz	**0.704**	0.02	**0.687**	0.03
2 steel bars @ 1.16 GHz	**0.589**	0.01	**0.579**	0.02
3 steel bars @ 288 MHz	**1.037**	0.02	**1.041**	0.03
3 steel bars @ 1.16 GHz	**0.877**	0.01	**0.880**	0.02

Table 3.4: Analysis of the measured data. To confirm the theoretical predictions, numerical values in the first and in the third columns should be identical (bold values). The combined uncertainty is also reported (plain text).

3.12 Power lost in the LHC beam screen

Previous results have shown that the surface current in a cylindrical (azimuthally inhomogeneous) metallic beam pipe is distributed uniformly with the azimuth, at least in the parameters range most important for the LHC. The H_τ (tangential magnetic field) on the boundary is, in fact, very close to the one of a charge in a perfectly conducting beam pipe (see Figs. 3.5, 3.16). The final field distribution in the "interesting" frequency range is thus pretty close to the first order term of a perturbative solution. This result is strictly valid provided that the skin depth is smaller than the screen thickness (which we have assumed infinite).

In the following section, we will apply those conclusions to the estimate of the power per unit length dissipated in the beam screen because of the resistive wall effect. Obviously the bigger part comes from the dissipation in the copper which covers the 59/60 of the beam screen surface. We will show anyway that the contribution of the small welding strip (1/60 of the surface) is non-negligible, especially at cryogenic temperatures.

There are two main differences between the model studied above, i.e. cylindrical metallic beam pipe with a smoothly varying conductivity $\sigma(\phi)$ as in Eq. (3.20) and the real LHC beam screen. First of all the beam screen has a "step-like" change in the conductivity going from the copper one to the conductivity of the welding (which we will assume close to the stainless steel one). Moreover the cross section of the screen is not exactly circular but it is flattened at two opposite sides (see Fig. 0.1).

If the image currents are constant for a pipe with a smoothly varying conductivity, it is reasonable to assume it constant also in the real LHC case. The effect of the change in geometry (from the cylindrical one to the real one) can then be estimated using the static field solution [2]. After having reminded the expression for the power dissipated in the resistive walls of a cylindrical beam pipe, we will give estimations for the correcting factors to account for the real geometry and we discuss the power loss values.

3.12.1 Parasitic heating power for the LHC beam screen and form factors F and G

For reader's convenience, Table 3.5 recalls the LHC parameter concerning the following discussion. The average current I_{av} refers to the nominal conditions (protons at 7 TeV) and it is the product of the bunch charge (Q), the revolution frequency (f_0) and the number of bunches in the beam (M).

Caption	**Symbol**	**Numerical Value**
Vacuum screen width		44 mm
Vacuum screen height		36 mm
Welding surface (fraction)	r_W	1/60
Average current	$I_{av} = MQf_0$	536 mA
Machine length	L	27 km
Bunch length r.m.s.	σ_z	7.5 cm

Table 3.5: LHC parameters for the power lost calculation. The average current I_{av} is the nominal current (at 7 TeV), Q is the bunch charge, f_0 the revolution frequency and M the number of bunches in the machine.

The parasitic heating power P generated in the resistive wall can be derived by the total energy lost by all the bunches W:

$$P = WMf_0. \tag{3.66}$$

The energy lost can be estimated [15] with

$$\begin{aligned} W &= \int_{-\infty}^{\infty} dt \int_{wall} dV \boldsymbol{j}(r,\phi,z;t)\cdot\boldsymbol{e}(r,\phi,z;t) = \\ &= \frac{1}{2\pi}\int_{-\infty}^{\infty} d\omega \int_{wall} dV \boldsymbol{J}(r,\phi,z;\omega)\cdot\boldsymbol{E}(r,\phi,z;\omega) = \\ &= \frac{1}{2\pi}\int_{-\infty}^{\infty} d\omega \int_{wall} dV \sigma \left|E_z(r,\phi,z;\omega)\right|^2, \end{aligned} \tag{3.67}$$

where $j(t)$ ($e(t)$) is the current density (electric field) in the time domain and $J(\omega)$ ($E(\omega)$) its Fourier transform. The Parseval theorem has been used in the first equality; the current density J is directed along the z-direction and $J_z = \sigma E_z$. Equation (3.67) is an energy lost by the beam and it is sometimes reported in literature [15, 33] with a minus sign; we assume a different notation, that is positive energy (power) stands for energy (power) lost by the charges.

As demonstrated above, the field on the boundary is pretty similar to the perturbative approach solution in a wide range of frequencies and thus from Eqs. (3.9, 3.18, 3.19) we get

$$\left|E_z(r,\phi,z;\omega)\right|^2 \simeq 2\left(\frac{1}{\sigma\delta}\right)^2 \left|H_\tau^{ch.}\right|^2 \exp\left(-2\frac{r-b}{\delta}\right), \tag{3.68}$$

where H_τ^{ch} is the tangential component of the source field on the boundary. Such a field is equal to $H_\phi^{S.C.}$ in Eq. (3.38) only for a circular cross section. The geometrical part of the integral in Eq. (3.67) reads

$$\int_{wall} dV\sigma\left|E_z\right|^2 = 2\int_0^L dz\int_0^{2\pi} d\phi\frac{1}{\sigma\delta^2}\left|H_\tau^{ch.}\right|^2\int_{b(\phi)}^{\infty}\exp\left(2\frac{r-b(\phi)}{\delta}\right)rdr =$$
$$= L\int_0^{2\pi}\frac{b(\phi)}{\sigma(\phi)\delta(\phi)}\left|H_\tau^{ch.}(\phi)\right|^2 d\phi, \tag{3.69}$$

where L is the machine length. In the last line of the previous equation the (potential) ϕ-dependence of all the quantities has been underlined. In a circular cross section beam pipe, b and H_τ^{ch} are independent from the azimuth, but for the real LHC beam pipe (flattened cross section and azimuthally varying conductivity) it is not the case. In polar coordinates the actual cross section is described by a ϕ-dependent radius $b(\phi)$, as shown in Fig. 3.25 (solid line). The cross section can be inscribed in a circle of radius b = 22 mm according to Table 3.5 (dashed line in Fig. 3.25). In the following, we will discuss first power loss estimates for a circular cross section of radius b and then correct it to account for the real geometry. The correction factor will be obtained by comparing the solution of the Poisson equation (with a Dirac delta of charge in the centre) in the two geometries.

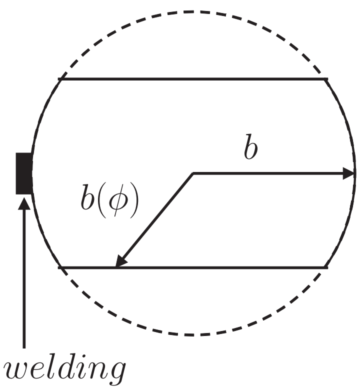

Figure 3.25: Real geometry (solid line) and its "circular" approximation (dashed line). The real geometry can be described by a radius $b(\phi)$ depending on the azimuth. The radius of the external circumference is b. On one side there is the welding strip which is wide about r_W =1/60 of the all cross section (in the picture it has been enlarged).

Let us consider first a circular screen of radius b uniformly covered by copper; in this case then, including Eqs. (3.67, 3.69) in Eq. (3.66), we get the for the parasitic heating power [59]

$$P_{copper}^{Circ} = \Gamma\left(\frac{3}{4}\right)\frac{L}{4\pi^2 b}\sqrt{\frac{\mu_0}{2\sigma_C}}\frac{I_{av}^2}{Mf_0}\left(\frac{c}{\sigma_z}\right)^{3/2}. \tag{3.70}$$

In fact the tangential magnetic field is equal to $H_\phi^{S.C.}$ in Eq. (3.38) where the charge depends on the frequency according to the bunch shape; for a gaussian bunch we have to use $Q\exp\left(-\omega^2\sigma_z^2/2c^2\right)$ with Q equal to the total bunch charge and σ_z the r.m.s. bunch length. The skin depth depends on the square root of the frequency and the integral over the all spectrum can be performed analytically using [16]:

$$\int_0^\infty \exp\left(-\mu x^2\right) x^{\nu-1} dx = \frac{1}{2}\mu^{-\nu/2}\Gamma\left(\frac{\nu}{2}\right). \tag{3.71}$$

The shape of the beam screen cross section affects the heating power. In particular the geometrical part of W, that is Eq. (3.69), accounts for this. Thus for the actual shape of the beam screen (solid line in Fig. 3.25) and for a screen made only of copper (i.e. not considering the weldings), the power is

$$P_{copper}^{Real} = G P_{copper}^{Circ} \qquad \text{with} \qquad G = \frac{\left[\int_0^{2\pi} b(\phi)\left|H_\tau(\phi)\right|^2 d\phi\right]_{Real}}{\left[\int_0^{2\pi} b\left|H_\tau\right|^2 d\phi\right]_{Circ}}, \tag{3.72}$$

since $\sigma(\phi) = \sigma_C$ and P_{copper}^{Circ} is the power dissipated in the circular circumscribed liner (dashed line in Fig. 3.25).

A fraction r_W of the cross section (i.e. the welding strip) is not made by copper, but by a more resistive material (stainless steel); as shown in Fig. 3.25 the welding is placed on the circular part of the cross section. Assuming the welding smaller than the whole circumference ($r_W \ll 2\pi$) and the tangential magnetic field constant on the welding, the heating power becomes

$$P_{C,SS}^{Real} = \left(1 + r_W\sqrt{\frac{\sigma_C}{\sigma_{Ss}}}\,\frac{F}{G}\right) P_{copper}^{Real} \qquad \text{with} \qquad F = \frac{\left|H_\tau\right|^2_{Real}}{\left|H_\tau\right|^2_{Circ}} \tag{3.73}$$

where σ_{Ss} is the conductivity of the stainless steel and $|H_\tau|$ is evaluated on the centre of the welding. The factor F accounts for the changing of the field in the welding position in the real cross section compared to the circular one; since the weldings are in the circular part of the cross section, we don't expect a major change (i.e. $F \approx 1$).

The heating power is calculated from the rigorous expression for a circular liner, i.e. P_{copper}^{Circ} in Eq. (3.70), with some correction factors F and G which have to be estimated. This approach has already been used in [2, 59] where it was applied to the previous LHC liner design (square cross section with weldings on the rounded corners); the field on the metal was estimated already with the perturbative approach. To evaluate the correction factors we compare the solution of the Poisson equation (with a Dirac delta of charge in the centre) for the two different geometries [2], assuming a perfectly conducting boundary. In the first order solution the tangential magnetic field is proportional to the radial electric field which, itself, is identical to the one in the static case (i.e. the solution of the Poisson equation). In [2] the ratio between the field on the inscribed circular liner and the field in the welding position was found to be approximately $1/2$ (which means $1/4$ in power) for the beam screen with square cross section. This factor of $1/4$ has to be compared with F/G in Eq. (3.73). Thus the factors F and G can be evaluated with

$$F \simeq \left(\frac{|E_r|_{Real}}{|E_r|_{Circ}}\right)^2 \qquad \text{and} \qquad G \simeq \frac{\left[\int_0^{2\pi} b(\phi)\,|E_r|^2\,d\phi\right]_{Real}}{\left[\int_0^{2\pi} b\,|E_r|^2\,d\phi\right]_{Circ}} \tag{3.74}$$

where the E_r is the radial electric field on the boundary generated by an unitary static line of charge in the centre of the beam screen.

3.12.2 Numerical solution of the Poisson equation and estimates for F and G

Many methods are available to solve numerically the Poisson equation (see for example [60]). To evaluate the quantities in Eq. (3.74) only a 2D Poisson solver is needed. The cross section has been divided in square cells (the meshes) in order to create a 91×91 grid, as shown in Fig. 3.26 for the circular (left picture) and the actual (right picture) beam screen.

From the numerical solution we get for each cell a value of the potential $V(x, y)$ and then, by its derivative, the electric field components. An initial condition and a source value for $V(x, y)$ is assigned to each cell. In each white cell of Fig. 3.26 the value of the potential is (re)computed at each step of the solution, while in the black cells it is fixed to zero (boundary condition for a perfect conductor). The source is a charge placed in the middle of the structure (little black dot). The algorithm used is the so called Jacobi's method: the potential on each cell is $1/4$th of the sum of the potential of the four closer cells along the two coordinate axes. This method is the simplest one, but also the less optimised. Other more refined numerical solutions would have been possible considering algorithms more performing

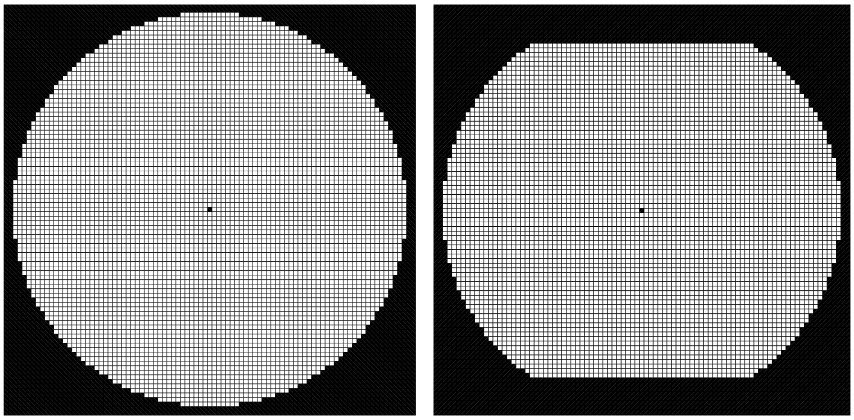

Figure 3.26: Geometry used in the solution of the 2D Poisson equation for the static electric potential. The left picture represents a circular approximation of the beam screen cross section that is the right picture. The equation is solved in a 91×91 grid; in the white cells the potential is updated at each step of the solution while in the black ones the value of the potential is fixed to zero, since they represent the perfectly conducting boundary. The little black points in the middle are the source (a Dirac delta of charge).

in terms of solution accuracy and convergence time [60] or even using a more appropriate meshing scheme (triangular meshes instead of rectangular ones).

The diameter of the circular beam screen is 44 mm and the number of cells available along the (horizontal or vertical) diameter are 87 (= 91-4 since two cells on each side are assigned to belong to the perfect conductor). The step of our meshing is then $44/87 \simeq 0.5$ mm which implies a quantisation uncertainty of roughly $0.5/44 \simeq 1$ % (at least on the horizontal or vertical axis).

For a circular beam pipe, the electric field can be calculated analytically and it scales with $1/r$, where r is the radius. The numerical solution is reported in Fig. 3.27 both for a circular beam pipe and for the real one. In the centre, where the point charge is, there is the expected discontinuity (the calculated field is zero because of symmetry). Actually, Fig. 3.27 is a density plot of the logarithm of the field going from higher field values in the centre (red colour) to lower field values close to the boundary (blue colour).

The reliability of the numerical solution strongly depends on the number of iterations. The electric field on a horizontal radius is shown in Fig. 3.28 for various numbers of iterations and for the circular beam pipe. Since the field scales as $1/r$, we expect a straight line in a double logarithmic scale; this is the case only of the magenta line (4000 iterations) and of the light blue line (12000 iterations). All the numerical results presented in this section are

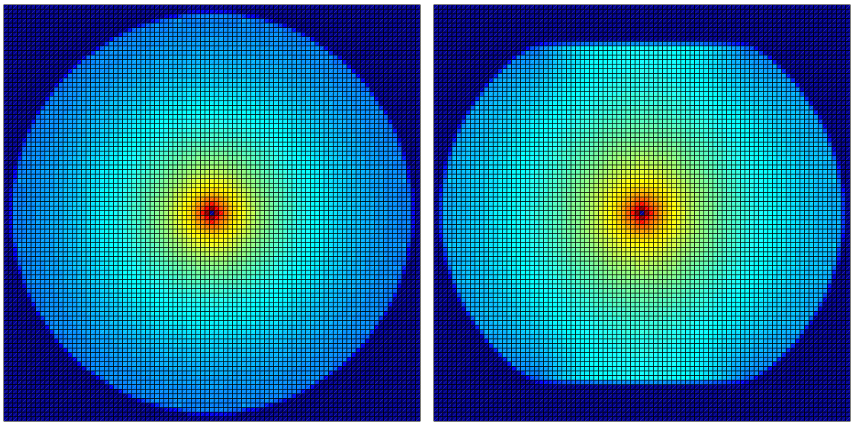

Figure 3.27: Static electric field from the solution of the Poisson equation in a circular beam screen (left picture) and in the actual one (right picture). The charge is in the centre. The field is plotted in logarithmic scale, going from the red (higher field values) to the blue (lower field values).

solutions after 12000 iterations. Increasing the number of them doesn't improve substantially the solution: the black crosses in Fig. 3.28 represent 24000 iterations, but the difference with the 12000 case is not remarkable.

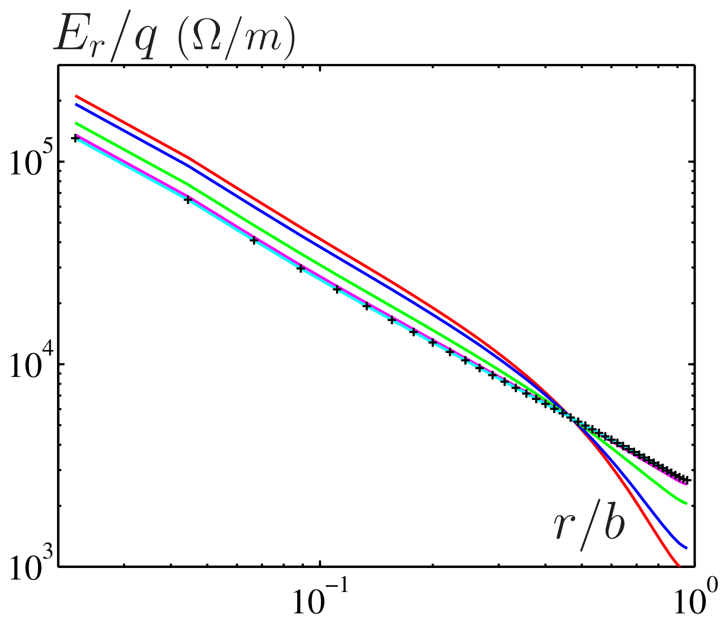

Figure 3.28: Radial electric field as a function of the radius for a circular beam screen. The theoretical electric field scales as $1/r$ and thus it is a straight line in a "double logarithmic" plot. The curves differ in the number of iterations performed in the solution of the equation: 900 (red curve), 1100 (blue curve), 2000 (green curve), 4000 (magenta curve), 12000 (light blue curve), 24000 (black crosses). The number of 12000 iterations is a good compromise between solution accuracy and computation time. ($b = 22$ mm)

The solution for the (radial) electric field on the horizontal radius is eventually shown in Fig. 3.29 as a function of the normalised radius. The field is discontinuous in the origin (where the source is); the green line represents the exact solution for the circular pipe, while the blue one is the actual numerical solution for a circular pipe. The field in the real flattened geometry is the red curve. A zoom of the region close to the boundary (where the welding is) is presented in the left picture of Fig. 3.29. The difference between the circular and the actual profile of the beam pipe is marginal and comparable to the difference between the exact solution and our solution for a circular pipe (such a difference can be assumed as a realistic measure of the inaccuracy of the final solution). The dots on each curve indicate the value actually computed by the Poisson solver, i.e. the cells of our grid. The value of the field in the first cell after the boundary is not correct (left picture in Fig. 3.29), because of the way the numerical derivative is performed (the potential and the electric field are discontinuous at the boundary).

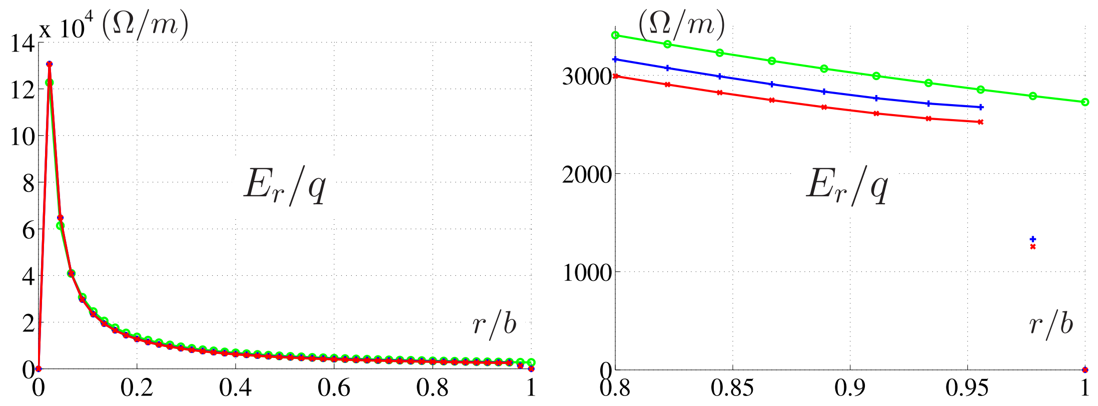

Figure 3.29: Electric field in the horizontal direction as a function of the normalised radius (r/b). The left picture is a zoom close to the structure boundary of the right one. The green curve represents the exact solution for the field of a line of charge in a perfectly conducting circular beam pipe. The blue curve is the field in a circular cross section while the red one is the field in the flattened cross section. Those curves are very close since the two geometries are identical along an horizontal radius. The dots indicate the points where the solution is actually numerically computed (i.e. the grid points).

The electric field along the vertical radius is shown in Fig. 3.30, where again the blue and green curves concern to the circular pipe and the red one is for the actual cross section. The red curve stops, obviously, at $r/b = 36/44 = 0.82$ since the cross section is flattened. The field on the boundary is $\sim$30 % greater than the field in the circular pipe at the corresponding position (and this effect is bigger than our uncertainty).

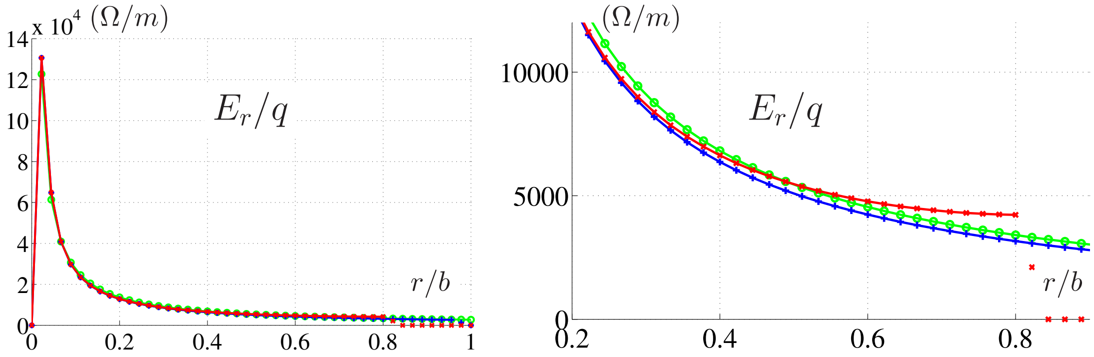

Figure 3.30: Electric field in the vertical direction as a function of the normalised radius (r/b). The left picture is a zoom close to the structure boundary of the right one. The green curve represents the exact solution for the field of a line of charge in a perfectly conducting circular beam pipe. The blue curve is the field in a circular cross section while the red one is the field in the flattened cross section. Obviously the red curve stops at $r/b = 36/44 = 0.82$, since the real cross section is smaller than the circular one in the vertical direction. The field on the boundary in this case is $\sim$30 % bigger than the field in the circular pipe at the corresponding position (blue curve). The dots indicate the points where the solution is actually numerically computed (i.e. the grid points).

From the knowledge of the field in every cell of our grid, we can then easily estimate the F and G factors as suggested in Eq. (3.74). In particular to evaluate G we have to perform integrals of the field on the boundary (or as close as possible to it). As shown before in Figs. 3.29–3.30, the field on the grid point closer to the boundary is not correct and thus the actual integration paths chosen are drawn in Fig. 3.31, for both the cross sections. Since

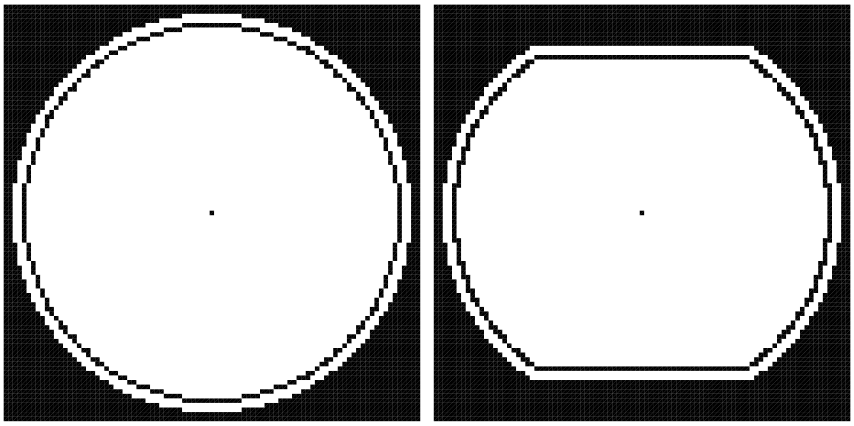

Figure 3.31: Path of the integral used to evaluate the factor G in Eq. (3.74) for the circular beam screen (left picture) and for the actual one (right picture).

the electric field is radial on the integration path, we can insert directly the electric field in

Eq. (3.74) and then F and G are

$$F \simeq 0.89 \qquad \text{and} \qquad G \simeq 1.03. \tag{3.75}$$

From Fig. 3.30, one might expect a much larger G (since the fields differ of 30 % on the vertical radius), but this is not the case because a relevant part of the integral is performed on the "circular" pieces of the path were the difference between the field in the real geometry and in the circular one is negligible (see Fig. 3.29).

The fraction of the power dissipated in the welding is weighted by the factor F/G accounting for the geometric effect. In previous design of the liner (square cross section with the welding at one of the rounded corners) such a factor was estimated around 1/4 [2]. In the present geometry it increases roughly to unity, the reason being that the corner "protected" somehow the welding from the bunch field (for a sharp corner the field is zero in the the corner).

3.12.3 The anomalous skin effect

In order to give reliable estimates for the power losses in the LHC case, we have to consider also the so called anomalous skin effect. The anomalous skin effect theory [61]–[62] attributes the anomalous increase of surface resistance of metals at high frequencies and low temperatures to the long mean free path λ of the conduction electrons. When the skin depth δ becomes much smaller than λ, only a fraction of the conduction electrons moving almost parallel to the metal surface is effective in carrying current and the classical theory breaks down. In copper, for instance, at low temperature the conductivity saturates to a maximum value (and δ reaches a minimum); the mean free path, on the contrary, increases with decreasing temperature and it might well be that at some frequency δ and λ are comparable. For LHC, this frequency is well inside the relevant bunch spectrum and this anomalous regime can play an important role. To asses this, measurements have been done on beam screen samples [55]–[63], but it is not an easy task to make reliable predictions. In fact the surface resistance at low temperature is the result of the surface properties (and thus of the manufacturing process) and it may vary in presence of strong magnetic fields. The relevance and the interconnections among all those effect is not yet fully understood.

Without entering in the details of the theory, we will give below some basic formulae to account the variation of surface resistivity when δ and λ are comparable, based on an interpolation formula for the so called diffusion model [61]–[62]. Measured values of relevant physical quantities concerning LHC beam screen samples to plug in those formulae are discussed in the next sub-section.

Follow the notation of [59], in the normal regime the surface resistance is

$$R_s^{Norm.} = \frac{1}{\sigma\delta} = \sqrt{\frac{\omega\mu_0}{2\sigma}}, \tag{3.76}$$

σ being the conductivity of the metal; on the contrary, the anomalous skin effect theory predicts the following surface resistance:

$$R_s^{Anom.} = R_\infty \left(1 + 1.157\alpha^{-0.276}\right) \quad \text{for} \quad \alpha \geq 3. \tag{3.77}$$

The dimensionless parameter α is a function of the ratio between the mean free path and the skin depth, that is

$$\alpha = \frac{3}{2}\left(\frac{\lambda}{\delta}\right)^2 = \frac{3}{2}\omega\mu_0\left(\frac{\lambda}{\sigma}\right)^2\sigma^3 \tag{3.78}$$

and R_∞ is a quantity independent of temperature and impurity, having a $\omega^{2/3}$ dependence on the frequency:

$$R_\infty = \left[\frac{\sqrt{3}}{16\pi}\frac{\lambda}{\sigma}\left(\omega\mu_0\right)^2\right]^{1/3}.$$

The ratio λ/σ is a characteristic of the metal and for copper one has

$$\frac{\lambda}{\sigma} = 6.6 \times 10^{-16}\ \Omega\text{m}^2,$$

which gives

$$R_\infty = 1.123 \times 10^{-3}\ \Omega \times \left(\frac{\omega}{2\pi\ \text{GHz}}\right)^{2/3}.$$

Assuming that the interpolation formula Eq. (3.77) applies over the whole bunch spectrum (which is not strictly true at low frequencies), the relative increase of heating power according to the theory is

$$A = \frac{P_{Anom.}}{P_{Norm.}} = \frac{\int_0^\infty \exp\left[-\left(\omega\sigma_z/c\right)^2\right] R_s^{Anom.}(\omega)\ d\omega}{\int_0^\infty \exp\left[-\left(\omega\sigma_z/c\right)^2\right] R_s^{Norm.}(\omega)\ d\omega}, \tag{3.79}$$

for a circular beam screen. The geometrical correction factors to account for the real beam screen cross section are unchanged since the they do not depend on frequency (and in fact they are calculated for the static case).

3.12.4 Numerical values

In the following, we are going to apply the previous formulae in order to get numerical values of the expected heating power in the LHC liner. First of all, one has to find out the correct values for the conductivity of the copper and of the welding and then apply the relations mentioned above.

Starting from the copper, its conductivity depends primarily on the manufacturing procedure and on the surface properties (e.g. smooth or ribbed surface). On top of that, at LHC operating conditions the beam screen will be in the 8 T dipole field and the magneto-resistance effect has to be included in any reasonable estimate. The final value for the conductivity turns out to be affected by many factors which are difficult to predict theoretically. To the best of our knowledge, the latest experimental data are reported in [64] where they quote a copper conductivity at room temperature of $4.6\ 10^7$ S/m and of $1.3\ 10^9$ S/m at LHC operating conditions (liquid He temperature and 8 T magnetic field). These values are deduced by warm/cold measurements without magnetic field; the extrapolation to high magnetic field scenarios is based on the results of [63]. The copper conductivity values refer to samples of the latest version of the beam screen, thus including the saw-tooth corrugation of the surface. The warm conductivity is affected by the surface corrugation, but the cold one does not seem to be sensitive to the saw-tooth structure. Table 3.6 compares those conductivity data with earlier estimates in [2], which refer to samples without corrugation (only the room temperature conductivity is remarkably different).

	Liquid He Temp. and High Field	**Room Temp.**
Copper conductivity [2]	$1.8\ 10^9$ S/m	$6.7\ 10^7$ S/m
Copper conductivity [64]	$1.3\ 10^9$ S/m	$4.6\ 10^7$ S/m
Welding conductivity	$2\ 10^6$ S/m	$2\ 10^6$ S/m

Table 3.6: State-of-the-art estimates of the conductivities of the metals present in the LHC beam screen. The values in the last two lines will be used in the estimations for the heating power per circulating beam.

On the contrary, the welding conductivity (roughly the stainless steel one) is not affected by the temperature and it will be assumed to be $2\ 10^6$ S/m. Due to the low value of the conductivity (even at liquid He temperature), the skin depth remains always bigger than the mean free path and the condition to enter the anomalous regime is never met.

For reader's convenience, we have summarised the conductivity data for copper and for the welding in Table 3.6, but in the following, we will use only the values in the last two lines.

To account for the anomalous skin effect in presence of a strong magnetic field, the value of the cold copper conductivity from Table 3.6 is used in the interpolation formula Eqs. (3.77). Then expressions for the power P^{Circ}_{copper}, P^{Real}_{copper} of Eqs. (3.70, 3.72) have simply to be multiplied by the factor $A = 1.07$ of Eq. (3.79). On the contrary, in the total power dissipated in actual screen (copper + welding) $P^{Real}_{C,SS}$, only the component due to the copper part is affected by the anomalous decrease of the conductivity, while the contribution of the welding $\left(P^{Weld}_{SS}\right)$ can be assumed independent from the temperature. The numerical values are reported in Table 3.7 where the ΔP^{Weld} is the contribution of the welding divided by the contribution of the copper part P^{Real}_{copper}.

	P^{Circ}_{copper}/L mW/m	P^{Real}_{copper}/L mW/m	$P^{Real}_{C,SS}/L$ mW/m	P^{Weld}_{SS}/L mW/m	ΔP^{Weld}
Room temperature	374	385	412	27	7 %
Liquid He temperature (classical regime)	71	73	100	27	37 %
Liquid He temperature (anomalous regime)	76	78	105	27	34 %

Table 3.7: Heating power per unit length. The first column concerns the case of a circular copper coated beam screen, while the second column is for the flattened (real) cross section, but again without welding strip. The power dissipated in the real situation (flattened screen with a welding strip) is given in the third column; the fourth and fifth ones report the fraction dissipated on the welding (absolute value and percentage).

Our final result for the heating power in the LHC beam screen at nominal operating conditions is 105 mW/m per circulating beam, having considered the ohmic losses in the copper and in the welding. The previous estimate of the heating power [64] was about 104 mW/m lost per each beam without including the effect of the welding strip but considering a smaller value of the beam screen radius (i.e. 17.4 mm instead of 22 mm) [65] and a larger average current (i.e. 560 mA instead of 536 mA). Moreover, from Table 3.7 we can conclude that the the small welding strip (1/60 of circumference) is negligible at room temperature, but increases the losses by about 34% at cryogenic temperature. The flattening of the cross section doesn't affect remarkably the power losses with respect to the circular profile.

3.13 Conclusions

We have shown (semi-)analytically that for a sinusoidal azimuthal variation of the conductivity, the magnetic field on the boundary is practically purely azimuthal ($H_\phi \gg H_z$) and it is constant over the azimuth down to very low frequency. Thus the same amount of current flows in the good conductor as in the bad one. Numerical simulations and bench measurements on a prototype substantially confirm this prediction.

The longitudinal electric field on the axis (proportional to the longitudinal coupling impedance per unit length) is the average over the azimuth of the electric field on the boundary. It differs from the constant conductivity case, as shown in Eq. (3.52), because of a term proportional to Y_n/Y_0 squared.

Moreover, the perturbative approach is confirmed in the relevant frequency range for the LHC. The comparison between the complete ("exact") solution and the perturbative one (assuming that H_ϕ is constant and equal to the source field) shows that the two solutions are very close in the GHz range, while they differ going towards low frequencies.

The small welding strip of the LHC beam pipe (about 1/60th of the pipe circumference), will therefore dissipate about 7% of the power dissipated in the copper coated part (at room temperature). At cryogenic temperatures, the effect is even more evident and the dissipated power in the small strip will be 34 % of that dissipated in the copper.

Conclusions

The aim of this work has been to study the interactions between the LHC beam and the surrounding pipe (for the actual design). Three main potential sources of beam energy loss have been addressed: the interaction with the pumping holes, the sawtooth surface corrugation and the effect of an azimuthally inhomogeneous metallic beam pipe. An analytical (or semi-analytical) approach has always been pursued, to better understand the relevant parameters to be optimised. Whenever possible, theoretical results are compared to numerical simulations and/or experimental data, sometimes found in literature and sometimes developed ad hoc. In the following we briefly review the main results for the three different subjects addressed and the most important consequences for the design of the LHC liner.

Pumping holes

In the framework of Bethe's modified theory, the energy lost by a relativistic particle beam travelling in a coaxial liner with many holes (small with respect to the wavelength λ) has been estimated. Interference among the holes is the main source of losses and it is affected by the ohmic attenuation in the coaxial only over sufficiently long distances.

The beam excites propagating waves in the coaxial region, namely forward and backward waves. Their contributions have been studied, showing that the backward propagating waves are responsible for sharp peaks in the coupling impedance; these are strongly dependent on the hole spacing and they are reduced by a partial randomisation of the positions of the holes. Nevertheless, for the actual LHC parameters, these peaks are outside the relevant frequency spectrum of the bunch; thus the loss factor (namely the energy loss) is not very much affected by the the backward wave and turns out to be independent from the randomisation. The loss factor (and the power lost per unit length which is proportional to it) is mainly connected, for the LHC, by the interaction between the beam and the forward propagating waves.

Over short distances, the interference between the holes is not affected by the ohmic losses in the coaxial region and the loss factor due to N equispaced holes scales with N^2; the resulting power loss per unit length is proportional to the length of the slotted section. Over longer distances, only a fraction of the holes interact constructively and the resulting power losses reach an upper saturation value. This behaviour is physically very reasonable. To define a separation between these two different behaviours, the attenuation length L_α has been introduced: for slotted sections shorter than L_α, the holes interfere constructively and the power lost per unit length grows linearly, while for sections longer than L_α only the holes within an attenuation length can interfere and the power lost per unit length saturates. L_α is inversely proportional to the attenuation and for LHC L_α is approximately 80 m; the saturation value of the power for the LHC rounded-end slots is about 1 mW/m (10 mW/m for circular holes) and it is negligible compared to the power deposited by the incoherent synchrotron radiation [2], which would be the case without the liner. On top of that the slotted liner will be interrupted at every dipole (which is 14 m long) and the attenuation will practically not play any role (at least in the present design).

The losses depend strongly on the slot width (with the fourth power) and on the wall thickness (exponentially). Possible scenarios with reduced wall thickness and wider holes have been investigated in [23]: the power lost per unit length increases up to 30 mW/m by doubling the width of the holes and decreasing of by half the wall thickness [24] and this may not be tolerable.

The results discussed are quite general and rigorous (as long as Bethe's theory holds): no assumptions are made on the shape of the apertures which is taken into account by means of the static polarizabilities. This theory has been successfully applied also to a long narrow slot (compared to λ) by applying Bethe's theory to infinitesimal slices of the slot [6].

Surface corrugation

To estimate the the effect of the sawtooth corrugation foreseen in the LHC liner, the problem of the wakefields generated by an ultrarelativistic particle travelling in a long beam tube with periodic rough surface has been revisited by means of a standard theory based on the hybrid modes excited in a periodically corrugated rectangular waveguide. Slow surface waves synchronous with the particle can be excited in the structure, producing wakefields whose frequency and amplitude depend on the depth of the corrugation. In the LHC, the roughness is in the order of tens of microns (much smaller than the relevant wavelengths and of the beam pipe dimensions).

Over an infinitely long structure, the beam can transfer energy only to synchronous waves whose frequencies are fixed. Such frequencies scales a $1/\sqrt{h}$, h being the depth of the corrugation, in the limit of small corrugations with respect to λ. The longitudinal wake field for a single charge due to the surface wave is (to first order) proportional to h and obviously vanishes in the limit of $h \to 0$. For the LHC, the first of these frequencies turns out to be about 80 GHz, that is much higher than the relevant frequencies of the spectrum of the long LHC bunch. Nevertheless such a sharp peak in frequency (ideally a Dirac δ for very long structures) may induce micro-bunching effects, resulting in a (non tolerable) bunch lengthening. The high Q of such a field may not correspond to reality because such a high frequency field (80 GHz) may have various Q-limitations (such as mode-mixing due to discontinuities). Such effects are non trivial to estimate and to be safer one could plan to interrupt the rough surface from time to time (but not periodically), thus reducing the interaction length between the beam and the synchronous wave.

For other machines, such as novel linear colliders, the natural surface roughness may induce analogous phenomena, but in this case such high frequencies are relevant since they are comparable to the bunch frequencies (the r.m.s. bunch lengthes are of the order of microns). A number of studies has been started very recently in order to quantify exactly the effect of the roughness. The natural roughness of a surface is obviously "statistically" distributed, but the geometry addressed in chapter 2 (equally spaced corrugations) has been successfully applied as a worst-case analysis [31].

Azimuthally inhomogeneous pipe

A welding in the copper coated LHC beam pipe can be assimilated to a small strip of a bad conductor (approximately stainless steel), covering about 1/60th of the entire pipe circumference.

We have shown (semi-)analytically that for a sinusoidal azimuthal variation of the pipe conductivity, the current is constant over the azimuth up to very low frequency. In principle this is not obvious, since it is known that at "low frequency" the current should "avoid" the bad conductor, according to Ohm's law (that is flowing in the best conductor).

In the limit of very low frequencies, the solution behaves "mathematically" according to Ohm's law, but it isn't strictly valid since the assumed boundary conditions don't hold anymore.

Since the same current does flow both in the copper and in the bad conductor in the LHC beam screen, the small welding strip will dissipate about 7% of the power dissipated in the copper coated part at room temperature. At cryogenic temperatures, the effect is even more evident (since the conductivity of the copper increases but the electric properties of the welding remain unchanged) and the small strip will dissipate about 34% of the power dissipated in the copper. The expected heating power is roughly 105 mW/m, considering the values of the conductivities of copper and stainless steel in presence of a strong magnetic field according to [64]. The effect of the geometry, since the beam screen is not circular, is considered and it has been estimated comparing the solution of the Poisson equation in the real cross section and in the circumscribed one [2]. The field on the welding position is practically identical to the field in the circular (circumscribed) geometry, since the welding is located far away from the flat part of the beam screen.

Numerical simulations (HFSS) confirm the constant magnetic field over the azimuth, when simulating a pipe made of strips of different conductors. The (numerical) field solution inside the metal is very time consuming, since the mesh sides have to be of the order of the skin depth; thus also the numerical codes use impedance boundary conditions.

Measurements on a prototype have also been performed to assess the validity of the result. A cylindrical pipe, made of 12 interchangeable bars, is used to simulate different conductivity profiles. The quality factor of a TEM resonator obtained by inserting a conductor in the centre depends strongly on the number of badly conducting bars. It is shown that the measured dependence is consistent with the predicted constant azimuthal magnetic field within the measurement uncertainty, which is mainly due to mounting/dismounting tolerances.

Appendix A

Appendix to Chapter 1

A.1 First order iterative solution

We now outline briefly the most important steps leading from Eq. (1.9) to Eq. (1.11); we take as an example the magnetic dipole moment M_φ, but also for P_r the procedure is essentially the same.

Substituting Eq. (1.10) in the RHS of Eqs. (1.9), we get the first order solution $M_\varphi^{(1)}$, discussed in Sec. 1.2.1:

$$M_\varphi^{(1)}(z_h) = \alpha_m \left[H_{0\varphi} e^{-jk_0 z_h} - j\frac{\omega}{2}\mu h_{0\varphi}^2 \sum_{k=1}^{N} \alpha_m H_{0\varphi} e^{-jk_0 z_k} e^{-jk_c|z_h - z_k|} + \right.$$
$$\left. + j\frac{\omega}{2} h_{0\varphi} e_{0r} \sum_{k=1}^{N} sgn(k-h)\varepsilon\alpha_e E_{0r} e^{-jk_0 z_k} e^{-jk_c|z_h - z_k|} \right]. \tag{A.1}$$

Since

$$E_{0r} = Z_0 H_{0\varphi} = Z_0 \frac{q}{2\pi b}, \qquad \mu h_{0\varphi}^2 H_{0\varphi} = \frac{\mu}{Z_0}\frac{H_{0\varphi}}{2\pi b^2 \ln(d/b)},$$
$$\varepsilon h_{0\varphi} e_{0r} E_{0r} = \varepsilon Z_0 \frac{H_{0\varphi}}{2\pi b^2 \ln(d/b)}, \qquad \frac{\mu}{Z_0} = \varepsilon Z_0 = \frac{1}{c},$$

it yields

$$M_\varphi^{(1)}(z_h) = \alpha_m H_{0\varphi} \left[e^{-jk_0 z_h} - j\frac{k_0}{4\pi b^2 \ln(d/b)} \alpha_m \sum_{k=1}^{N} e^{-jk_0 z_k - jk_c|z_h - z_k|} + \right.$$
$$\left. + j\frac{k_0}{4\pi b^2 \ln(d/b)} \alpha_e \sum_{k=1}^{N} sgn(k-h) e^{-jk_0 z_k - jk_c|z_h - z_k|} \right]. \tag{A.2}$$

After some algebraic manipulation, recalling that $k_c = k_0 - j\alpha$ and that $sgn(k-h) = 0$ if $k = h$ we find

$$M_\varphi^{(1)}(z_h) = \alpha_m H_{0\varphi} \left[e^{-jk_0 z_h} - \alpha_m T_1 - \alpha_m T_2 - \alpha_e T_3 + \alpha_e T_4 \right] \tag{A.3}$$

where

$$T_1 = j\frac{k_0}{4\pi b^2 \ln(d/b)} e^{-jk_0 z_h} \sum_{k=1}^{h} e^{\alpha(z_k - z_h)},$$

$$T_2 = T_4 = j\frac{k_0}{4\pi b^2 \ln(d/b)} \sum_{k=h+1}^{N} e^{-j2k_0 z_k} e^{-\alpha(z_k - z_h)} e^{jk_0 z_h} = j\frac{k_0}{4\pi b^2 \ln(d/b)} e^{-jk_0 z_h} \sum_{w=1}^{N-h} e^{-(j2k_0+\alpha)(z_{w+h} - z_h)},$$

$$T_3 = j\frac{k_0}{4\pi b^2 \ln(d/b)} e^{-jk_0 z_h} \sum_{k=1}^{h-1} e^{\alpha(z_k - z_h)} = T_1 - j\frac{k_0}{4\pi b^2 \ln(d/b)} e^{-jk_0 z_h}.$$

Thus simply ordering the terms, one gets

$$M_\varphi^{(1)}(z_h) = \alpha_m H_{0\varphi} e^{-jk_0 z_h} \left\{ 1 - j\frac{k_0}{4\pi b^2 \ln(d/b)} \left[\alpha_m + (\alpha_m + \alpha_e) F_h e^{-\alpha z_h} + (\alpha_m - \alpha_e) B_h \right] \right\},$$

where

$$F_k = \sum_{w=1}^{k-1} e^{\alpha z_w} \quad \text{and} \quad B_k = \sum_{w=1}^{N-k} e^{-(j2k_0+\alpha)(z_{w+k} - z_k)} = \sum_{w=1}^{N-k} e^{-j(2k_0+\alpha)\sum_{t=1}^{w} D_{k+t}},$$

with $D_k = z_k - z_{k-1}$ being the distance between two consecutive holes ($k = 1, \dots, N$). The identity

$$z_{w+h} - z_h = \sum_{w}^{t=1} D_{h+t}$$

is useful to take into account the case of randomly spaced holes, where $D_k = \bar{D} + \delta_k$ with δ_k a random variable.

A.2 Approximation of S for large number of holes

The relation (1.42) was first obtained numerically from (1.41), having chosen practical values for the dimensionless parameter $\alpha = D/\sigma$. Here we report an (more elegant) analytical study based on [21] to prove that

$$S = \sum_{h=1}^{N-1} (N-h) e^{-(hD/\sigma)^2} \left[2\left(\frac{D}{\sigma}h\right)^2 - 1 \right] = \frac{1}{2}\left[N - \left(\frac{\sigma}{D}\right)^2 \right].$$

We can rewrite (1.41) as

$$S = 2\alpha^2 N S_2 - N S_0 - 2\alpha^2 S_3 + S_1 \qquad \text{where} \qquad S_k = \sum_{h=1}^{N-1} h^k e^{-\alpha^2 h^2} \tag{A.4}$$

and we try to express S_k in terms of proper integrals of

$$f_k(x,\alpha) = x^k e^{-\alpha^2 x^2} \qquad k = 0, \ldots, 3. \tag{A.5}$$

First of all, let's notice that

$$\frac{\partial f_k}{\partial h}(h,\alpha) = k f_{k-1}(h,\alpha) - 2\alpha^2 f_{k+1}(h,\alpha). \tag{A.6}$$

The relation between the sum S_k and the integral of f_k is shown in Fig. A.1, for an arbitrary function. The dashed area represents the generic term of the sum, provided that $\Delta h = 1$; its difference with the integral is the area of the region ABC. In first approximation, we can consider that region as a triangle of base Δh and height

$$|f(h) - f(h-1)| = \left|\frac{\partial f}{\partial h}\right| \Delta h$$

and its area is shown in the figure. This has to be added or subtracted depending on which lower limit of the integral is chosen; in formulae:

$$\begin{aligned}\sum_{h=1}^{N-1} h^k e^{-\alpha^2 h^2} &= \int_0^{N-1} f_k(x,\alpha)dx + \frac{1}{2}\sum_{h=1}^{N-1}\frac{\partial f_k}{\partial h}(h,\alpha) \\ &= \int_1^{N-1} f_k(x,\alpha)dx - \frac{1}{2}\sum_{h=1}^{N-1}\frac{\partial f_k}{\partial h}(h,\alpha)\,.\end{aligned} \tag{A.7}$$

Performing the integration from 0, we have to compare the rectangle of height $f(h)$ and width Δh (dashed area) with the integral from $f(h-1)$ to $f(h)$; on the contrary, that rectangle will be compared with the integral from $f(h)$ to $f(h+1)$ if the integration itself starts from 1. Obviously, Fig. A.1 deals with the first case. Defining

$$I_k = \int_0^{N-1} f_k(x)dx = \int_0^{N-1} x^k e^{-\alpha^2 x^2} dx$$

and using Eq. (A.6) in the first one of Eqs. (A.7) yields

$$S_k = I_k + \frac{k}{2} S_{k-1} - \alpha^2 S_{k+1}. \tag{A.8}$$

The preference of the first one of Eqs. (A.7) is arbitrary; choosing the second one, we would obtain a relation similar to Eq. (A.8) with a different definition of I_k and opposite signs of the last two terms. The integrals I_k are easily solved in closed form:

$$\begin{aligned} I_0 &= \frac{\sqrt{\pi}}{2\alpha} Erf[(N-1)\alpha], \qquad I_1 = \frac{1 - e^{-(N-1)^2\alpha^2}}{2\alpha^2}, \\ I_2 &= \frac{\sqrt{\pi} Erf[(N-1)\alpha]}{2\alpha} - \frac{N-1}{2\alpha^2} e^{-(N-1)^2\alpha^2}, \quad I_3 = \frac{1}{2\alpha^4} - \frac{1 + (N-1)^2\alpha^2}{2\alpha^4} e^{-(N-1)^2\alpha^2} \end{aligned} \tag{A.9}$$

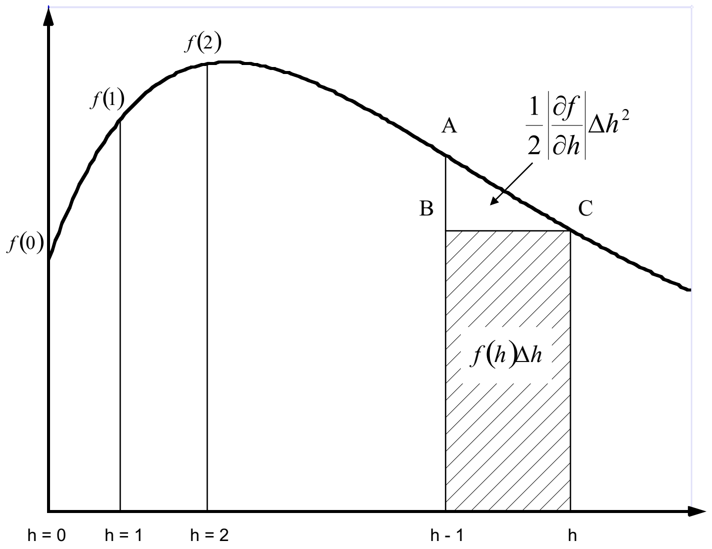

Figure A.1: Relation between the sum and the integral. The difference between the dashed area and the integral can be approximated by a triangle, for sufficiently smooth functions.

The recursive relation (A.8) can be used to compute exactly each S_k from the knowledge of I_k; the number of meaningful terms to be taken into account depends on the value of α.

Taking

$$S_0 \simeq I_0 - \alpha^2 I_1, \quad S_1 \simeq I_1, \quad S_2 \simeq I_2, \quad S_3 \simeq I_3 \tag{A.10}$$

and substituting in Eq. (A.4), eventually we get:

$$S = \frac{1}{2}\left(N - \frac{1}{\alpha^2}\right) + \left[\frac{1}{2\alpha^2} - \frac{3}{2}N + 1\right] e^{-(N-1)^2\alpha^2}; \tag{A.11}$$

in the limit of large N the last expression gives Eq. (1.42). The assumption behind Eq. (A.10) is somehow arbitrary and it is justified a posteriori comparing Eq. (1.42) with the exact value (Eq. (1.41)); however the rigorous derivation from Eq. (A.8) is not worthwhile since the number of terms to be taken into account depends on how much α is smaller than 1.

Appendix B

Appendix to Chapter 2

B.1 Magnetic Hertzian potential

The magnetic Hertz potential Π_x satisfies the wave equation, thus

$$\Pi_x = \left[A\cos\left(\xi_x x\right) + B\sin\left(\xi_x x\right)\right]\left[C\cos\left(\xi_y y\right) + D\sin\left(\xi_y y\right)\right]e^{-j\xi_z z}, \tag{B.1}$$

where A, B, ξ_x and ξ_y are constants. Since the tangential electric field vanishes on the boundary $x = \pm a/2$, the four possible expressions are

$$\begin{aligned}
\Pi_{x1} &= \sum_n A_n \cos\left(\frac{n\pi}{a}x\right)\cos\left(\xi_y y\right)e^{-j\xi_{zn}z} \qquad n = 1, 3, 5, \ldots && \text{(B.2)}\\
\Pi_{x2} &= \sum_n A_n \cos\left(\frac{n\pi}{a}x\right)\sin\left(\xi_y y\right)e^{-j\xi_{zn}z} \qquad n = 1, 3, 5, \ldots && \text{(B.3)}\\
\Pi_{x3} &= \sum_n A_n \sin\left(\frac{n\pi}{a}x\right)\cos\left(\xi_y y\right)e^{-j\xi_{zn}z} \qquad n = 0, 2, 4, \ldots && \text{(B.4)}\\
\Pi_{x4} &= \sum_n A_n \sin\left(\frac{n\pi}{a}x\right)\sin\left(\xi_y y\right)e^{-j\xi_{zn}z} \qquad n = 0, 2, 4, \ldots && \text{(B.5)}
\end{aligned}$$

where A_n depends on the source and ξ_y is related to the other boundary condition. For instance in a smooth guide, the electric field vanishes also on the boundary $y = \pm b/2$ leading to $\xi_y = k_y = m\pi/b$ with m an even (odd) integer number for Π_{x1} and Π_{x3} (Π_{x2} and Π_{x4}).

B.2 Longitudinal wave number in a corrugated waveguide

In this section, we derive Eq. (2.13), showing that ξ_z is the sum of the wave number of a smooth guide (k_z) plus a term depending on the corrugation depth h and vanishing for $h \to 0$.

Considering the roughness as a perturbation of a smooth waveguide, ξ_y can be written as:

$$\xi_y = k_y + \delta k_y \tag{B.6}$$

where δk_y is the difference from the unperturbed $k_y = m\pi/b$ and it vanishes for $h \to 0$. We may write Eq. (2.6) as

$$\begin{aligned} K_{yn} \tan\left(K_{yn} h\right) &= \left(k_y + \delta k_y\right) \frac{\cos(m\pi/2)\cos(\delta k_y b/2) - \sin(m\pi/2)\sin(\delta k_y b/2)}{\sin(m\pi/2)\cos(\delta k_y b/2) + \cos(m\pi/2)\sin(\delta k_y b/2)} \\ &= -\left(k_y + \delta k_y\right) \tan\left(\delta k_y b/2\right), \end{aligned} \tag{B.7}$$

having to consider only odd values for m since Eq. (2.6) is obtained from Π_{x2}. Therefore, using $\tan(x) \approx x$ and solving a second order algebraic equation, we get

$$\delta k_y = -\frac{k_y}{2} \pm \sqrt{\left(\frac{k_y}{2}\right)^2 - 2\frac{K_{yn}}{b}\tan\left(K_{yn} h\right)}, \tag{B.8}$$

where only the $+$ sign is physically meaningful. Therefore the wave number becomes

$$\xi_z^2 = k^2 - k_x^2 - \xi_y^2 \approx k^2 - k_x^2 - k_y^2 - 2k_y \delta k_y \tag{B.9}$$

and then

$$\xi_z^2 \approx k^2 - k_x^2 - k_y^2 \sqrt{1 - 8\frac{K_{yn}}{b k_y^2}\tan\left(K_{yn} h\right)} \approx k_z^2 + \frac{4K_{yn}}{b}\tan\left(K_{yn} h\right); \tag{B.10}$$

eventually taking the first order term of the square root, we get Eq. (2.13).

B.3 Point charge excitation

In this Appendix we derive Eqs. (2.14). The Lorentz reciprocity theorem [17] states that

$$\oint_S \left(\boldsymbol{E}_n^\pm \times \boldsymbol{H} - \boldsymbol{E} \times \boldsymbol{H}_n^\pm\right) \cdot \boldsymbol{n}\, dS \; = \; \int_V \boldsymbol{J} \cdot \boldsymbol{E}_n^\pm \, dV \tag{B.11}$$

where $\boldsymbol{E}$, $\boldsymbol{H}$ is the field radiated by the source of current density $\boldsymbol{J}$ in the volume V closed in the surface S with inward normal $\boldsymbol{n}$. $\boldsymbol{E}_n$, $\boldsymbol{H}_n$ are the normal modes of the structure, that is

$$\boldsymbol{E}_n^\pm = \boldsymbol{e}_n^\pm e^{\mp\Gamma_n z} = \left(\boldsymbol{e}_{tn} \pm \boldsymbol{e}_{zn}\right) e^{\mp\Gamma_n z} \quad \text{and} \quad \boldsymbol{H}_n^\pm = \boldsymbol{h}_n^\pm e^{\mp\Gamma_n z} = \left(\pm\boldsymbol{h}_{tn} + \boldsymbol{h}_{zn}\right) e^{\mp\Gamma_n z}; \tag{B.12}$$

the index $\pm$ stands for forward and backward propagating wave with respect to a fixed origin $z = 0$. The field radiated in the positive z-direction by the current filament $\boldsymbol{J}$ can be represented by

$$\boldsymbol{E}^{+} = \sum_n a_n \boldsymbol{E}_n^{+}, \qquad \boldsymbol{H}^{+} = \sum_n a_n \boldsymbol{H}_n^{+} \tag{B.13}$$

while the field propagating in the negative z-direction is

$$\boldsymbol{E}^{-} = \sum_n b_n \boldsymbol{E}_n^{-}, \qquad \boldsymbol{H}^{-} = \sum_n b_n \boldsymbol{H}_n^{-}. \tag{B.14}$$

For any perfectly conducting cylindrical waveguide, the integral over S reduces to one over the generic cross sections S_1 and S_2:

$$\oint_S \ldots \cdot \boldsymbol{n}\; dS = \int_{S_1} \ldots \cdot \boldsymbol{n}_1\; dS_1 + \int_{S_2} \ldots \cdot \boldsymbol{n}_2\; dS_2,$$

where $\boldsymbol{n}_1 = \hat{z}_o$ and $\boldsymbol{n}_2 = -\hat{z}_o$. Specifically Eq. (B.13) gives the radiated field on the cross section S_2, while Eq. (B.14) gives the field on S_2. Substituting Eqs. (B.13–B.14), Eq. (B.11) becomes

$$\begin{aligned}
&\int_{S_1} \left(\boldsymbol{E}_n^{+} \times \sum_m b_m \boldsymbol{H}_m^{-} \;-\; \sum_m b_m \boldsymbol{E}_m^{-} \times \boldsymbol{H}_n^{+} \right) \cdot \hat{z}_0\; dS_1 \;+ \\
-&\int_{S_2} \left(\boldsymbol{E}_n^{+} \times \sum_m a_m \boldsymbol{H}_m^{+} \;-\; \sum_m a_m \boldsymbol{E}_m^{+} \times \boldsymbol{H}_n^{+} \right) \cdot \hat{z}_0\; dS_2 \;= \\
=&\int_V \boldsymbol{J} \cdot \boldsymbol{E}_n^{+}\; dV;
\end{aligned} \tag{B.15}$$

thus, since

$$\begin{aligned}
\hat{z}_0 \cdot \boldsymbol{e}_i^{\pm} \times \boldsymbol{h}_j^{\mp} &= \mp \hat{z}_0 \cdot \boldsymbol{e}_{ti} \times \boldsymbol{h}_{tj} \\
\hat{z}_0 \cdot \boldsymbol{e}_i^{\pm} \times \boldsymbol{h}_j^{\pm} &= \pm \hat{z}_0 \cdot \boldsymbol{e}_{ti} \times \boldsymbol{h}_{tj},
\end{aligned} \tag{B.16}$$

we get eventually

$$\begin{aligned}
&-\sum_m b_m e^{-(\Gamma_n - \Gamma_m) z} \int_{S_1} \hat{z}_0 \cdot \left(\boldsymbol{e}_{tn} \times \boldsymbol{h}_{tm} + \boldsymbol{e}_{tm} \times \boldsymbol{h}_{tn} \right)\; dS_1 + \\
&+\sum_m a_m e^{-(\Gamma_n + \Gamma_m) z} \int_{S_2} \hat{z}_0 \cdot \left(\boldsymbol{e}_{tn} \times \boldsymbol{h}_{tm} - \boldsymbol{e}_{tm} \times \boldsymbol{h}_{tn} \right)\; dS_2 = \\
&= \int_V \boldsymbol{J} \cdot \boldsymbol{E}_n^{+}\; dV,
\end{aligned} \tag{B.17}$$

that is Eq. (2.14a) with Eq. (2.16) and $\Gamma = j\xi_z$. With same reasoning, Eq. (2.14b) can be derived from Eq. (B.11). The integrals defining A_{nm} and B_{nm} should be performed on the whole section of the rough waveguide; nevertheless in our working hypothesis, the transversal field inside the slots is null, thus giving no contribution.

For a smooth waveguide, where the modes are orthogonal, it holds

$$\int_S \boldsymbol{e}_{ti} \times \boldsymbol{h}_{tj} \cdot \hat{z}_0 \; dS = \delta_{ij}, \tag{B.18}$$

leading to Eq. (2.17).

B.3.1 Longitudinal electric field

In the following, we derive Eq. (2.21) for the electric field from Eq. (2.18). Being

$$\begin{aligned} A_{nn} =& 2\int_S \hat{z}_0 \cdot \boldsymbol{e}_{tn} \times \boldsymbol{h}_{tn} \; dS = \\ =& 2\int_S \hat{z}_0 \cdot \left[(\boldsymbol{e}_{xn} + \boldsymbol{e}_{yn}) \times (\boldsymbol{h}_{xn} + \boldsymbol{h}_{yn})\right] \; dS = \\ =& -2\int_S e_{yn} h_{xn} \; dS, \end{aligned} \tag{B.19}$$

from Eq. (2.3) with Π_{x2}, it holds

$$e_{yn} = -\omega\mu_0 \left|\xi_{zn}\right| \cos\left(k_{xn}x\right) \sin(\xi_y y), \tag{B.20}$$

$$h_{xn} = (k^2 - k_{xn}^2) \cos\left(k_{xn}x\right) \sin(\xi_y y), \tag{B.21}$$

and Eq. (2.19) comes directly. Also Eq. (2.20) is straightforward since

$$e_z = j\omega\mu_0 \xi_y \cos\left(k_{xn}x\right) \cos(\xi_y y) \tag{B.22}$$

and

$$\int_{-\infty}^{+\infty} e^{-j(\omega/\beta c \;\pm\; \xi_{zn})z} \; dz = 2\pi\delta\left(\omega/\beta c \;\pm\; \xi_{zn}\right). \tag{B.23}$$

The z-component of the electric field E_z, according to Eqs. (B.13–B.14) is

$$E_z = a_n e_{zn} e^{-j\xi_{zn}z} - b_n e_{zn} e^{j\xi_{zn}z}, \tag{B.24}$$

that is after simple algebraic manipulation Eq. (2.21).

Appendix C

Appendix to Chapter 3

C.1 Currents and Hertzian potentials

By means of an equivalence principle, the field inside a perfectly conducting waveguide can be found substituting the boundary with a sheet of current radiating in the free space (see sec 3.2). In our cylindrical geometry the boundary is simply $r = b$; following [38] we assume for a line of current flowing at $(b, \phi = 0)$ in the z-direction a spectral current density of

$$\boldsymbol{J}(r, \phi, z; \omega) = \hat{z}\frac{f(z)}{\pi}\frac{\delta(r-b)}{r}\delta(\phi), \tag{C.1}$$

where (r, ϕ, z) is the observation point in cylindrical coordinates, $\delta(x)$ is the Dirac-delta function and $f(z)$ is a generic function giving the z-dependence of the current, e.g. for a particle of charge $1/\pi$ moving at velocity βc, $f(z)$ is $\exp(j\omega z/\beta c)$. In the frequency domain the Hertzian potential is given by:

$$\boldsymbol{\Pi}(\boldsymbol{r}; \omega) = j\frac{Z_0}{4\pi k}\int_V \boldsymbol{J}(\boldsymbol{r}'; \omega) g\left(|\boldsymbol{r}-\boldsymbol{r}'|\right) d\boldsymbol{r}', \tag{C.2}$$

where $g\left(|\boldsymbol{r}-\boldsymbol{r}'|\right)$ is the Green's function in the frequency domain, i.e. the response to an impulsive source in $\boldsymbol{r}'$ satisfying the given boundary condition. Following [38], the Green's function for the Hertzian potential in the free space can be written as

$$\frac{e^{jk|\boldsymbol{r}-\boldsymbol{r}'|}}{|\boldsymbol{r}-\boldsymbol{r}'|} = \frac{j}{2}\sum_{m=0}^{\infty} e^{-jm(\phi-\phi')}\int_{-\infty}^{\infty}\left\{\begin{array}{c} J_m(\Omega r)\, H_m(\Omega r') \\ J_m(\Omega r')\, H_m(\Omega r)\end{array}\right\} e^{-j\alpha(z-z')}d\alpha \quad \begin{array}{c} r<b \\ r>b \end{array}, \tag{C.3}$$

where J_m and $H_m = H_m^{(1)}$ are the Bessel and Hankel (first kind) functions of order m, $\Omega^2 = k^2 - \alpha^2$ and $Im(\Omega) > 0$. Using this equation in the integral definition of the Hertzian potential (Eq. (C.2)), we may get the expression for the electric Hertzian potential in Eq. (3.5)a reminding that

$$\int_{-\pi}^{\pi} \delta(\phi')e^{jm\phi'}d\phi' = 1 \quad \text{and} \quad F(\alpha) = \frac{1}{2\pi}\int_{-\infty}^{\infty} f(z)e^{-j\alpha z}dz.$$

Similar reasonings justify the expression of the magnetic Hertzian potential.

Taking the Hertzian potentials from Eq. (3.5) for $r < b$ and considering $F_m(\alpha)$, $\widetilde{F}_m(\alpha)$ proportional to $\delta(\alpha - k_z)$ through F_m and $\widetilde{F}_m$, the potentials may be rewritten as:

$$\Pi_z = -j\frac{Z_0}{4\pi b}\sum_m F_m H_m(k_t b) J_m(k_t r)\cos(m\phi)e^{jk_z z} \tag{C.4a}$$

$$\widetilde{\Pi}_z = \frac{1}{4\pi b}\sum_m \frac{\widetilde{F}_m}{k_t} H'_m(k_t b) J_m(k_t r)\sin(m\phi)e^{jk_z z} \tag{C.4b}$$

since $\Omega^2 = k^2 - k_z^2 = k_t^2$. This is analogous to the usual formulation in TE and TM modes (see for example [50]) in a perfectly conducting waveguide. For example the longitudinal electric field (TM mode) of such a guide can be written [50],

$$E_z = \sum_m A_m J_m(k_t r)\cos(m\phi)e^{jk_{zm}z},$$

that is what we would get from Eqs. (C.4) provided that

$$A_m = Z_0\frac{k_t^2}{4\pi k}H_m(k_t b)F_m.$$

The coefficient A_m (F_m) is determined by the sources while k_t by the boundary conditions.

The fields synchronous with a single charge travelling at the phase velocity βc can be found using the Eqs. (3.7) in Eqs. (3.3), that is:

$$E_r = \frac{Z_0}{2\pi^2}\sum_{m=0}^{\infty}\left[\frac{k}{\beta^2\gamma}F_m\left\{\begin{array}{c} I'_m(r)K_m(b) \\ I_m(b)K'_m(r)\end{array}\right\} - m\frac{\beta\gamma}{kr}\widetilde{F}_m\left\{\begin{array}{c} I_m(r)K'_m(b) \\ I'_m(b)K_m(r)\end{array}\right\}\right]\cos(m\phi), \tag{C.5a}$$

$$E_\phi = -\frac{Z_0}{2\pi^2}\sum_{m=1}^{\infty}\left[\frac{m}{\beta}\frac{F_m}{r}\left\{\begin{array}{c} I_m(r)K_m(b) \\ I_m(b)K_m(r)\end{array}\right\} - \widetilde{F}_m\left\{\begin{array}{c} I'_m(r)K'_m(b) \\ I'_m(b)K'_m(r)\end{array}\right\}\right]\sin(m\phi), \tag{C.5b}$$

$$E_z = \frac{Z_0}{2\pi^2}\sum_{m=0}^{\infty}\frac{jk}{\beta^2\gamma^2}F_m\left\{\begin{array}{c} I_m(r)K_m(b) \\ I_m(b)K_m(r)\end{array}\right\}\cos(m\phi), \tag{C.5c}$$

$$H_r = \frac{1}{2\pi^2}\sum_{m=1}^{\infty}\left[m\frac{F_m}{r}\left\{\begin{array}{c} I_m(r)K_m(b) \\ I_m(b)K_m(r)\end{array}\right\} - \frac{\widetilde{F}_m}{\beta}\left\{\begin{array}{c} I'_m(r)K'_m(b) \\ I'_m(b)K'_m(r)\end{array}\right\}\right]\sin(m\phi), \tag{C.5d}$$

$$H_\phi = \frac{1}{2\pi^2}\sum_{m=0}^{\infty}\left[\frac{k}{\beta\gamma}F_m\left\{\begin{array}{c} I'_m(r)K_m(b) \\ I_m(b)K'_m(r)\end{array}\right\} - m\frac{\gamma}{kr}\widetilde{F}_m\left\{\begin{array}{c} I_m(r)K'_m(b) \\ I'_m(b)K_m(r)\end{array}\right\}\right]\cos(m\phi), \tag{C.5e}$$

$$H_z = -\frac{1}{2\pi^2}\sum_{m=1}^{\infty}\frac{j}{\beta\gamma}\widetilde{F}_m\left\{\begin{array}{c} I_m(r)K'_m(b) \\ I'_m(b)K_m(r)\end{array}\right\}\sin(m\phi), \tag{C.5f}$$

where the exponential factor $\exp(j\,z\,k/\beta)$ is dropped and the argument of the Bessel functions is $kr/\beta\gamma$ (or $kb/\beta\gamma$). The Bessel and Hankel functions J_m and H_m have been transformed in the modified Bessel functions I_m and K_m, according to:

$$J_m(jx) = j^m I_m(x) \quad \text{and} \quad H_m(jx) = \frac{2}{\pi j^{m+1}} K_m(x).$$

The field of a charge travelling in the free space can be derived as well from Eqs. (C.2–C.3), using the current density in Eq. (3.23) and recalling that:

$$\int_0^{\infty} \delta(r') J_m(\Omega r')\, dr' = \delta_{m0}, \qquad \int_{-\infty}^{\infty} e^{j\left(\alpha+\frac{k}{\beta}\right)} dz' = 2\pi\delta\left(\alpha + k/\beta\right) \quad \text{and} \quad k\sqrt{1-\frac{1}{\beta^2}} = j\frac{k}{\beta\gamma},$$

where $\delta(x)$ is always the Dirac-delta function while δ_{m0} is the Kronecker symbol. The resulting Hertzian potential of Eq. (3.24) does not depend on ϕ; the non-vanishing field components are

$$E_r = j\frac{k}{\beta}\frac{\partial \Pi_{0z}}{\partial r} = Z_0 \frac{Q}{2\pi\beta}\frac{k}{\beta\gamma} K_1\left(\frac{kr}{\beta\gamma}\right) e^{jzk/\beta} \longrightarrow Z_0 \frac{Q}{2\pi r} e^{jzk/\beta}, \tag{C.6a}$$

$$E_z = -\frac{k^2}{\beta^2\gamma^2}\Pi_{0z} = -jZ_0\frac{Q}{2\pi}\frac{k}{\beta^2\gamma^2} K_0\left(\frac{kr}{\beta\gamma}\right) e^{jzk/\beta} \longrightarrow 0, \tag{C.6b}$$

$$H_\phi = j\frac{k}{Z_0}\frac{\partial \Pi_{0z}}{\partial r} = \frac{Q}{2\pi}\frac{k}{\beta\gamma} K_1\left(\frac{kr}{\beta\gamma}\right) e^{jzk/\beta} \longrightarrow \frac{Q}{2\pi r} e^{jzk/\beta}, \tag{C.6c}$$

where the RHS represents the limit for $\beta \to 1$.

In a perfectly conducting pipe, the Hertzian potential can be written (Sec. 3.4) as the sum of the Hertzian potential in the free space (Π_{0z}) with a Π_{iz} given by Eq. (3.5a) for $m = 0$, which is related to image current "impressed" by the propagating mode on the surface. The longitudinal electric field, from Eq. (3.3a), is zero at the boundary $r = b$, thus

$$\frac{Z_0 Q}{2\pi b}\frac{kb}{\beta^2\gamma^2} K_0\left(\frac{kb}{\beta\gamma}\right) e^{jzk/\beta} = \frac{Z_0}{4\pi b}\int_{-\infty}^{\infty} F_0(\alpha)\left(k^2-\alpha^2\right) G_0(\alpha; r, b) e^{j\alpha z} d\alpha, \tag{C.7}$$

which is an equation for $F_0(\alpha)$. Multiplying each part of the previous equation for $\exp(-j\xi z)$ and by integrating along the z-axis, the solution for F_0 is

$$F_0(\xi) = \frac{Q\pi}{I_0(kb/\beta\gamma)}\delta\left(\xi - \frac{k}{\beta}\right). \tag{C.8}$$

It is trivial now to derive the Π_{iz} by using directly its definition, that is Eq. (3.5a):

$$\Pi_{iz} = -j\frac{Z_0 Q}{2\pi k} e^{jzk/\beta} \begin{cases} K_0\left(kb/\beta\gamma\right) I_0\left(kr/\beta\gamma\right)/I_0\left(kb/\beta\gamma\right) & r < b \\ K_0\left(kr/\beta\gamma\right) & r > b \end{cases} \tag{C.9}$$

which again is continuous in $r = b$. Π_{TOTz} is then the sum of the free space potential Π_{0z} with Π_{iz}, which is due to the presence of a boundary and directly related to the image currents on the perfect conductor; the final expression of Π_{TOTz} in a perfectly conducting pipe is Eq. (3.26).

If the charge is travelling in a pipe of constant conductivity σ the Hertzian potential can be written in the usual way of Eq. (3.25). Then the field components can be derived using Eq. (3.3), e.g.

$$E_z = -jZ_0 \frac{Q}{2\pi\beta}\frac{k}{\beta^2\gamma^2} K_0\left(\frac{kr}{\beta\gamma}\right) e^{jzk/\beta} + \frac{Z_0}{4\pi k}\int_{-\infty}^{\infty} F_0(\alpha)\left(k^2-\alpha^2\right) J_0(\Omega r) H_0(\Omega b) e^{j\alpha z} d\alpha,$$

$$H_\phi = \frac{Q}{2\pi}\frac{k}{\beta\gamma} K_1\left(\frac{kr}{\beta\gamma}\right) e^{jzk/\beta} + \frac{j}{4\pi}\int_{-\infty}^{\infty} \Omega F_0(\alpha) J_0'(\Omega r) H_0(\Omega b) e^{j\alpha z} d\alpha,$$

which are related by the SIBC $E_z = H_\phi/Y$. After some algebra and following the same procedure of Eq. (C.8),

$$F_0(\xi) = \frac{Q\pi}{K_0\left(kb/\beta\gamma\right)} \frac{K_0\left(kb/\beta\gamma\right) - j\frac{\beta\gamma}{Z_0 Y} K_1\left(kb/\beta\gamma\right)}{I_0\left(kb/\beta\gamma\right) + j\frac{\beta\gamma}{Z_0 Y} I_1\left(kb/\beta\gamma\right)} \delta\left(\xi - \frac{k}{\beta}\right). \tag{C.10}$$

which then inserted in Eq. (3.25) gives Eq. (3.28). In the limit of high γ then, the vector potential can be simplified as

$$\Pi_{TOTz} \approx -\left(\frac{\beta\gamma}{k}\right)^2 \frac{Q}{2\pi b} \frac{1/Y_0}{1 + jkb/\left(2Z_0 Y_0\right)} e^{jzk/\beta} \tag{C.11}$$

which implies the longitudinal electric field in Eq. (3.29).

C.2 Approximation of Bessel Functions

For small arguments, the Bessel functions I_m and K_m can be approximated with

$$I_m(x) \approx \frac{1}{m!}\left(\frac{x}{2}\right)^m + \frac{1}{(m+1)!}\left(\frac{x}{2}\right)^{m+2}, \tag{C.12a}$$

$$K_m(x) \approx \frac{(m-1)!}{2}\left(\frac{2}{x}\right)^m - \frac{(m-2)!}{2}\left(\frac{2}{x}\right)^{m-2}, \tag{C.12b}$$

for any generic $m \geq 2$ and $x \to 0$; the accuracy of the approximation depends on the order m. The arguments of the Bessel functions are always $kr/\beta\gamma$ or $kb/\beta\gamma$; in the limit of $\gamma \to \infty$

we can write:

$$I_m(r)K_m(b) \approx \frac{1}{2m}\left(\frac{r}{b}\right)^m - \left[\frac{1}{8m(m-1)}\left(\frac{r}{b}\right)^m - \frac{1}{8m(m+1)}\left(\frac{r}{b}\right)^{m+2}\right]\left(\frac{kb}{\beta\gamma}\right)^2 \quad \text{(C.13a)}$$

$$I_m(r)K'_m(b) \approx -\frac{\beta\gamma}{2kb}\left(\frac{r}{b}\right)^m + \left[\frac{m-2}{8m(m-1)}\left(\frac{r}{b}\right)^m - \frac{1}{8(m+1)}\left(\frac{r}{b}\right)^{m+2}\right]\left(\frac{kb}{\beta\gamma}\right), \quad \text{(C.13b)}$$

$$I'_m(r)K_m(b) \approx \frac{\beta\gamma}{2kb}\left(\frac{r}{b}\right)^{m-1} + \left[\frac{m+2}{8m(m+1)}\left(\frac{r}{b}\right)^{m+1} - \frac{1}{8(m-1)}\left(\frac{r}{b}\right)^{m-1}\right]\left(\frac{kb}{\beta\gamma}\right) \quad \text{(C.13c)}$$

$$I'_m(r)K'_m(b) \approx -\frac{m}{2}\left(\frac{kb}{\beta\gamma}\right)^2\left(\frac{r}{b}\right)^{m-1} - \left[\frac{m+2}{8(m+1)}\left(\frac{r}{b}\right)^{m+1} - \frac{m-2}{8(m-1)}\left(\frac{r}{b}\right)^{m-1}\right] \quad \text{(C.13d)}$$

The last expansion satisfies the usual relation

$$I_m\left(\frac{kb}{\beta\gamma}\right)K'_m\left(\frac{kb}{\beta\gamma}\right) - I'_m\left(\frac{kb}{\beta\gamma}\right)K_m\left(\frac{kb}{\beta\gamma}\right) = -\frac{\beta\gamma}{kb}.$$

At the orders $m = 0, 1$, I_m satisfies as well Eq. (C.12a); on the contrary a power series approximation is not straightforward for K_m at these orders since they behave logarithmically (see [49], pag. 379). On top of that, it turned out in Sec. 3.5 that, concerning the solution of the system, the fundamental quantity is I_m/I'_m; thus from Eq. (C.12a), expanding at the second order $1/I_m$ and multiplying for I'_m we get for $m \geq 1$

$$\frac{I'_m}{I_m}\left(\frac{kb}{\beta\gamma}\right) \approx m\frac{\beta\gamma}{kb} + \frac{1}{2(m+1)}\frac{kb}{\beta\gamma}. \quad \text{(C.14)}$$

C.3 To derive the system of equations in sec. 3.5

From Eq. (3.21) and Eq. (3.31) the quantity $-Y(\omega)E_\phi$ is (l is a generic positive integer):

$$\begin{aligned}
-Y(\omega)E^w_\phi =& \frac{Z_0Y_0}{2\pi^2}\left(E^n_\phi + \frac{Y_n}{2Y_0}E^{2n}_\phi\right)\sin(n\phi) + \\
& \frac{Z_0Y_0}{2\pi^2}\sum_{t=2}^{\infty}\left[E^{tn}_\phi + \frac{Y_n}{2Y_0}E^{(t-1)n}_\phi + \frac{Y_n}{2Y_0}E^{(t+1)n}_\phi\right]\sin(tn\phi) + \\
& \frac{Z_0Y_0}{2\pi^2}\sum_{\substack{m=2\\ m\neq ln}}^{\infty}\left[E^m_\phi + \frac{Y_n}{2Y_0}E^{(m-n)}_\phi + \frac{Y_n}{2Y_0}E^{(m+n)}_\phi\right]\sin(m\phi),
\end{aligned} \quad \text{(C.15)}$$

since the electric field of the charge has no component on the ϕ-direction. The longitudinal electric field, instead, will be the superposition of the charge field with the scattered one;

thus (l being a generic positive integer)

$$\begin{aligned}
Y(\omega)E_z = & \frac{Z_0Y_0}{2\pi^2}\left(jkbH_\phi^0 + \frac{2\pi^2}{Z_0}E_z^{S.C.} + \frac{Y_n}{2Y_0}jkbE_z^n\right) + \\
& \frac{Z_0Y_0}{2\pi^2}\left(jkbE_z^n + \frac{Y_n}{2Y_0}jkbE_z^{2n} + \frac{Y_n}{Y_0}\frac{2\pi^2}{Z_0}E_z^{S.C.} + \frac{Y_n}{Y_0}jkbH_\phi^0\right)\cos(n\phi) + \\
& \frac{Z_0Y_0}{2\pi^2}\sum_{t=2}^{\infty}\left[jkbE_z^{tn} + jkb\frac{Y_n}{2Y_0}E_z^{(t-1)n} + jkb\frac{Y_n}{2Y_0}E_z^{(t+1)n}\right]\cos(tn\phi) + \\
& \frac{Z_0Y_0}{2\pi^2}\sum_{\substack{m=2\\ m\neq ln}}^{\infty}\left[jkbE_z^{m} + jkb\frac{Y_n}{2Y_0}E_z^{(m-n)} + jkb\frac{Y_n}{2Y_0}E_z^{(m+n)}\right]\cos(m\phi).
\end{aligned} \tag{C.16}$$

Using Eqs. (C.15–C.16) in Eq. (3.30), applying the definitions Eqs. (3.31) in the ultrarelativistic limit and considering Eq. (3.35) results in a system of equations for H_ϕ^m and E_ϕ^m. In principle all the values of m are possible for the solution; if m is not an integer multiple of the order of the conductivity variation n, we get:

$$H_\phi^m = Z_0Y_0\left[jkbE_z^m + jkb\frac{Y_n}{2Y_0}E_z^{(m+n)}\right] \quad m < n, \tag{C.17a}$$

$$-jH_z^m = Z_0Y_0\left[E_\phi^m + \frac{Y_n}{2Y_0}E_\phi^{(m+n)}\right] \quad m < n, \tag{C.17b}$$

$$H_\phi^m = Z_0Y_0\left[jkbE_z^m + jkb\frac{Y_n}{2Y_0}E_z^{(m-n)} + jkb\frac{Y_n}{2Y_0}E_z^{(m+n)}\right] \quad m > n, \tag{C.17c}$$

$$-jH_z^m = Z_0Y_0\left[E_\phi^m + \frac{Y_n}{2Y_0}E_\phi^{(m-n)} + \frac{Y_n}{2Y_0}E_\phi^{(m+n)}\right] \quad m > n. \tag{C.17d}$$

Following the solution procedure suggested in Sec. 3.6, we can truncate the system at a generic, given order $L(> n)$: for $m > L$ the variables are assumed to be zero. The H_ϕ^m, E_ϕ^m of order $n < m < L$ may be written as functions of the variables at the order $(m - n)$ with suitable coefficients depending on the truncation order, analogously to Eq. (3.43). Therefore, substituting the coefficient of order $m + n$ in Eqs. (C.17a–C.17b) we get an homogeneous subsystem of two equations in two variables (H_ϕ^m, E_ϕ^m with $m < n$) with non singular matrix, that is $H_\phi^m = E_\phi^m = 0$. Repeating such a reasoning for $tn < m < (t + 1)n$, one can easily see that the only non-zero variables are of orders multiples of the periodicity of the pipe conductivity n.

C.4 Maxwell Equations for the approximated fields

The fields reported in Eqs. (C.5) satisfy obviously the Maxwell equations; infact they are built as a superposition of the solutions of the wave equation in cylindrical coordinates, obtained with the method of separation of variables. In the r coordinate the wave equation reads, in our case,

$$\frac{\beta\gamma}{kr}\frac{d}{dr}\left[rI_m'(r)\right] - \left[1 + m^2\left(\frac{\beta\gamma}{kr}\right)^2\right] I_m = 0, \tag{C.18}$$

that is the Bessel equation. Concerning the ultrarelativistic limit, we can approximate the Bessel functions with their expression for small arguments, as reported in Appendix C.2. Using Eqs. (C.13) (defined for $m > 1$), the approximated fields still satisfy the Maxwell equations; in checking that, the following relation may become useful:

$$\frac{1}{r}\frac{\partial}{\partial r}\left[r\left(\frac{r}{b}\right)^l\right] = \frac{l+1}{b}\left(\frac{r}{b}\right)^{l-1}. \tag{C.19}$$

Up to this moment the fields depends still on β, γ, F_m and $\widetilde{F}_m$; from Sec. 3.6 we have learnt that only the terms with $m = tn$ give contribution to the final solution and that F_{tn} and $\widetilde{F}_{tn}$ are proportional, i.e.:

$$\frac{F_{tn}}{b} = -tn\left(\frac{\beta\gamma}{kb}\right)^2 \widetilde{F}_{tn}. \tag{C.20}$$

In the approximated expression of the fields, the last statement implies that

$$\frac{1}{\beta}\frac{F_{tn}}{b} + tn\left(\frac{\beta\gamma}{kb}\right)^2 \widetilde{F}_{tn} = -\frac{\beta}{1+\beta}\frac{tn}{(kb)^2}\widetilde{F}_{tn}, \tag{C.21a}$$

$$\frac{F_{tn}}{b} + \frac{tn}{\beta}\left(\frac{\beta\gamma}{kb}\right)^2 \widetilde{F}_{tn} = \frac{\beta}{1+\beta}\frac{tn}{(kb)^2}\widetilde{F}_{tn}, \tag{C.21b}$$

and taking the limit for $\beta \to 1$ we get Eqs. (3.56), which again satisfy the Maxwell equations.

C.5 Ohm's Law

It is reasonable to expect that in the limit of low frequency, the wall current will behave according to Ohm's law. We will now try to understand what this means in our case.

Assuming a current I flowing in N resistors in parallel, the current I_j in the resistor j is simply

$$I_j = \frac{Y_j}{Y_{tot}} I \quad \text{where} \quad Y_j = \frac{\sigma_j S_j}{\ell};$$

Y_j is the admittance of the lumped resistor of conductivity σ_j, cross-section S_j (we assume that all the resistors have the same length ℓ). Obviously Y_{tot} is the sum of the admittances of all the N resistors.

In our case, taking a piece of conductor of length ℓ (along the z-axis), we may consider every infinitesimal volume ℓdS (see Fig. C.1) as a resistor of conductivity $\sigma(\phi)$ in which should flow (according to Ohm's law) a current equal to

$$dI = I\frac{dY}{Y_{tot}} = I\frac{\sigma(\phi)dS}{\ell Y_{tot}}.$$

Y_{tot} is constant and can be defined as the integral of dY in the metal enclosed in one skin

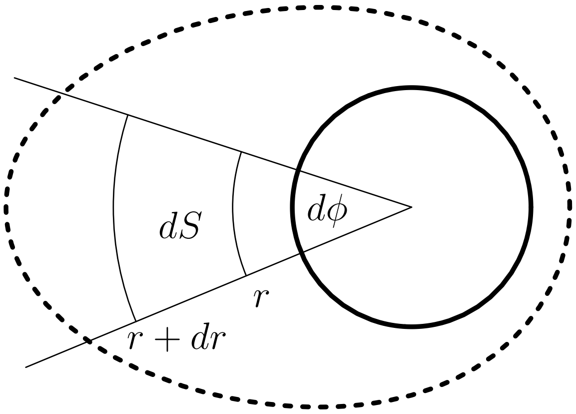

Figure C.1: Schematics used in derivation of Ohm's law. The solid line represents the section of pipe and the dotted line is $\delta(\phi)$ away from it. The infinitesimal surface element in the conductor is $dS = rdrd\phi$. Y_{tot} is the integral of dY in all the metal enclosed in one skin depth, that is the region enclosed by the solid and the dotted line.

depth $\delta(\phi)$, that is the region between the solid and the dotted line in Fig. C.1; thus

$$Y_{tot} = \int_0^{2\pi}\int_b^{\delta(\phi)+b}\frac{\sigma(\phi)}{\ell}rdrd\phi = \frac{2\pi}{\omega\mu\ell}\left[1 + b\sqrt{\frac{\omega\mu}{2}}\left(\sqrt{\sigma_{Cu}} + \sqrt{\sigma_{Ss}}\right)\right], \tag{C.22}$$

for $\sigma(\phi)$ as in Eq. (3.20) with $n \neq 0$. To summarise, Ohm's law states that the current density dI/dS is a function of ϕ proportional to $\sigma(\phi)$.

Bibliography

[1] The LHC Study Group, *The Large Hadron Collider, conceptual design*, CERN/AC/95-05 (LHC), 20 October 1995.

[2] F. Ruggiero, *Single-beam collective effects in the LHC*, CERN SL/95-09 (AP), LHC note 313 (1995) and Proc. Workshop on Collective Effects in Large Hadron Colliders, Montreux, 1994, eds. E. Keil and F. Ruggiero (Particle Accelerators, **50**, 1995), pp. 83–104.

[3] O. Brüning, F. Caspers, I.R. Collins et al., in *Proc. IEEE Particle Accelerator Conference, New York, USA, 1999*, Editors: A. Luccio, W. MacKay, pp. 2629–2631.

[4] S. De Santis, M. Migliorati, L. Palumbo and M. Zobov, *Coupling impedance of a hole in a coaxial beam pipe*, Phys. Rev. **E54**, 1996, pp. 800–805.

[5] S. De Santis, A. Mostacci and L. Palumbo, *Interference effects on the coupling impedance of many holes in a coaxial beam pipe*, Phys. Rev. **E56**, 1997, pp. 5990–5995.

[6] S. De Santis, A. Mostacci, L. Palumbo and B. Spataro, *Analytical expressions for the coupling impedance of a long narrow slot in a coaxial beam pipe*, Phys. Rev. **E56**, 1998, pp. 6565–6569.

[7] F. Caspers, E. Jensen and F. Ruggiero, *Impedance measurements for the pumping holes in the LHC liner*, CERN SL/92-15 (DI), PS/92-24 (RF/AR), LHC note 186 (1992) and Proc. EPAC Conference, Berlin, 1992, eds. H. Henke, H. Homeyer and Ch. Petit-Jean-Genaz (Editions Frontières, Singapore, 1992), pp. 889–891.

[8] H.A. Bethe, *Theory of diffraction by small holes* , Phys. Rev., **66**, 1944, pp. 163–182.

[9] S.S. Kurennoy, *Coupling impedance of pumping holes*, Particle Accelerators, **39**, 1992, pp. 1–13.

[10] G.V. Stupakov, *Coupling impedance of a long slot and an array of slots in a circular vacuum chamber*, Phys. Rev. **E51**, 1995, pp. 3515–3521.

[11] A.V. Fedotov and R.L. Gluckstern, *Analytic and numerical analysis of the longitudinal coupling impedance of a rectangular slot in a thin coaxial liner*, Phys. Rev. **E56**, 1997, pp. 3583–3601.

[12] A.V. Fedotov and R.L. Gluckstern, *Impedance and resonance issues for a long rectangular slot in a coaxial liner*, Phys. Rev. **E56**, 1997, pp. 7217–7222.

[13] S. Petracca, *Beam coupling impedance for perforated beam pipes with general shape from impedance boundary conditions*, Phys. Rev. **E60**, 1999, pp. 6030–6041.

[14] L. Palumbo, V.G. Vaccaro and M. Zobov, *Wake fields and impedance*, CAS Cern Accelerator School, Advanced school on accelerator physic, Rhodes 1994, LNF-94/041 (1994).

[15] B. W. Zotter and S. A. Kheifets, *Impedances and Wakes in High-Energy Particle Accelerators*, (World Scientific, Singapore, 1998).

[16] I.S. Gradshtein and I.M. Ryzhic, *Table of integrals, series and products. Corrected and enlarged edition*, (Accademic Press, New York, 1980), p. 1045.

[17] R.E. Collin, *Field theory of guided waves*, 2nd ed., (IEEE, New York, 1991).

[18] S.S. Kurennoy, *Impedance iussues for the LHC beam screen*, Proc. Workshop on Collective Effects in Large Hadron Colliders, Montreux, 1994, eds. E. Keil and F. Ruggiero (Particle Accelerators, **50**, 1995), pp. 167–104.

[19] R.K. Cooper, *High power RF trasmission*, CAS Cern Accelerator School, RF Engineering for Particle Accelerators, Oxford 1991, CERN 92-03 (1992), pp. 264–265.

[20] N.A. McDonald, *Electric and magnetic coupling through small apertures in shield walls of any thickness*, IEEE Trans. Microwave Theory Tech., **MTT-20**, no. 10, 1972, pp. 689–695.

[21] L. Palumbo, private communication, March 1998.

[22] R.S. Elliot, *An introduction to guided waves and microwave circuits*, (Prentice-Hall, Inc., New Jersey, 1993).

[23] A. Mostacci and F. Ruggiero, *Pumping slots and thickness on the LHC beam screen*, CERN LHC Project Note 195, August 1999.

[24] A. Mostacci, Mathematica 3.0 Notebook, August 1999, world-wide web address `wwwslap.cern.ch/collective/mostacci/slots/note/slots.nb`.

[25] S. Kurennoy, *Impedance of azimuthally symmetric irises and cavities with semielliptical profile in a beam pipe*, Phys. Rev. **E55**, 1997, 3533–3538.

[26] R.E. Thomson, R. Carr, S. Stupakov and D. Walz, *Effect of the beam-tube roughness on x-ray free electron laser performance*, Phys. Rev. ST Accel. Beams **2**, 1999, 060701, pp. 6.

[27] M. Timm, A. Novokhatski and T. Weinland, *The surface roughness wakefield effect*, in *Proc. International Computational Accelerator Physics Conference, Monterey, California, USA, 1998*.

[28] G. Di Massa, *Synchronous corrugated waveguide pick-ups*, SPS/ARF Note 85-8, CERN, 1985 (unpublished).

[29] The LCLS Design Study Group, SLAC Report No. SLAC-R-521, 1998, (unpublished).

[30] G. H. Bryant, *Propagation in corrugated waveguides*, Proc. IEE **116**, No. 2, 1969, pp. 203–212.

[31] M. Angelici, M. Migliorati, A. Mostacci, L. Palumbo, F. Ruggiero, S. Ugoli, *Wakefields due to surface waves in a beam pipe with a periodic rough surface*, to be published in Phys. Rev. ST-AB.

[32] D. Boussard, LABII/RF/Int./75-2, CERN, 1975 (unpublished).

[33] A. W. Chao, *Physics of Collective Beam Instabilities in High Energy Accelerators*, (Wiley-Interscience, New York, 1993).

[34] A. Chao, B. Chen and K. Oide, SLAC-PUB-6859 (1995) and in *Proc. of IEEE Particle Accelerator Conference, Dallas, USA, 1995*, pp. 3040-3042.

[35] F. Caspers, private communication, June 2000.

[36] K.L.F. Bane and A. Novokhatski, *The resonator impedance model of surface roughness applied to the LCLS parameters*, SLAC Report No. SLAC-AP-117, 1999 (unpublished).

[37] L. Palumbo, *Analytical calculation of the impedance of a discontinuity*, Particle Accelerators, Vol. 25, pp. 201–216, 1990.

[38] E. Gianfelice, L. Palumbo, *Dipole impedance of a conducting cylindrical pipe with a discontinuous cross section*, IEEE Trans, **NS**, Vol. 37, 1990.

[39] L. Palumbo, V.G. Vaccaro *Wake fields, impedance and Green's functions*, CAS Advanced School, Oxford 1985, CERN 87–03, 1987.

[40] L.A. Weinstein, *The theory of diffraction and the factorisation method*, Golem Press, Boulerd (USA), 1969.

[41] M.L. Levin, S.M. Rytov, V.D. Shafranov, *M.A. Leontovich's researches in electrodynamics*, Soviet Physics Uspekhi (USA), Vol. 26(4), pp. 353–355, 1983.

[42] M.A. Leontovich, *Investigations on Radiowave Propagation, Part II*, Printing House of the Academy of Sciences, Moscow, pp. 5–12, 1948 (in Russian).

[43] S.M. Rytov, *Calcul du skin-effet par la méthode des perturbations*, J. Phys. USSR, **2**, pp. 233–242, 1940.

[44] T.B.A. Senior, J.L. Volakis, *Approximate boundary conditions in electromagnetics*, (The Institute of Electrical Engineers, London, 1995).

[45] D.-S. Wang, *Limits of validity of the impedance boundary conditions on penetrable surfaces*, IEEE Trans. **AP**, Vol. 35, pp. 453–457, 1990.

[46] G. Stupakov, *Surface Impedance and Synchronous Modes*, SLAC-PUB-8208, 1999.

[47] J.J. Jowett, private communication, September 2000.

[48] S. Wolfram, *The Mathematica Book*, 3rd ed., (Wolfram Media/Cambridge University Press, 1996).

[49] M. Abramowitz, I. Stegun, *Handbook of mathematical functions with formulas, graphs, and mathematical tables*, (Dover Press, New York, 1964).

[50] R.E. Collin, *Foundations of microwave engineering*, 2nd edition, (McGraw Hill Publishing Company, 1992).

[51] A.B. Pippard, *The surface impedance of superconductors and normal metal at high frequencies. II. The anomalous skin effect innormal metals*, Proc. Roy Society (London), **A191**, 1947, pp. 385.

[52] See World Wide Web address, `www.ansoft.com`.

[53] M. Sands, J. Rees, *A bench measurement of the energy loss of a stored beam to a cavity*, SLAC-Report PEP-95, August 1974.

[54] V.G. Vaccaro, *Coupling impedance measurements: an improved wire method*, INFN/TC-94/023, 1994.

[55] J. Tan, *Technical and Practical Information on the Surface Resistance Measurement Bench Using the Shielded Pair Method: Application to the LHC Beam Screen* , CERN-SL-2000-002, January 2000.

[56] D. Kajfez, *Q-factor measurement techniques*, RFdesign, August 1999, world-wide web address `www.rfdesign.com`.

[57] International Organization for Standardization et al., *International Vocabulary of basic and general terms in metrology*, 2nd ed., (ISO, Geneva, 1993).

[58] International Organization for Standardization et al., *Guide to expression of uncertainty in measurement*, (ISO, Geneva, 1995), pp. 101.

[59] W. Chou and F. Ruggiero, *Anomalous skin effect and resistive wall heating*, CERN LHC Project Note 2, August 1995.

[60] R.C. Dehmel, *Solving the Discrete Poisson Equation using Jacobi, SOR, Conjugate Gradients and the FFT*, Lectures Notes of the course on "Applications of Parallel Computers", No. 15-16, March 1996. Web address: `www.cs.berkeley.edu/~demmel/cs267/lecture24/lecture24.html`

[61] A. B. Pippard, *The surface impedance of superconductors and normal metals at high frequencies. II. The anomalous skin effect in normal metals*, Proc. Royal Society (London), A191, 1947, pp. 385–399.

[62] R. G. Chambers, *The anomalous skin effect*, Proc. Royal Society (London), A215, 1952, pp. 481–499.

[63] F. Caspers, M. Morvillo, F. Ruggiero and J. Tan, *Surface resistance measurements and estimate of the beam induced resistive wall heating of the LHC dipole beam screen*, CERN LHC Project Report 307, August 1999.

[64] F. Caspers, M. Morvillo, F. Ruggiero, J. Tan and H. Tsutsui *Surface resistance measurements LHC dipole beam screen samples*, Proceedings European Particle Accelerator Conference (EPAC2000), Vienna, Austria, pp. 376–378, 26–30/6/00; also LHC Project Report 410, CERN, August 2000.

[65] J. Tan, private communication, May 2001.

Acknowledgements

First of all, I would like to express my deepest gratitude to the persons who gave me the unique opportunity to do this work: L. Palumbo and F. Ruggiero. I have been always impressed by their broad knowledge in physics (not only accelerator physics and electromagnetic field theory); they have been guiding me constantly for the past three years and without them, this thesis would not exist. They are for me bright examples for their scientific and human qualities: I am proud to be one of their students.

I am also indebted with my tutor F. Caspers who substantially helped me with the measurements: he patiently taught many practical things, transmitting to me his enthusiasm.

During part of the period of my thesis work, I profited of the hospitality of CERN and in particular of the Accelerator Physics group of the SL division (SL/AP). The "Collective Effects Team" always showed interest in my work, stimulating me and integrating me in its activities and initiatives. Moreover, most of the people of this group made concrete things to make me feel welcome and to support me, from every point of view: I will remember it.

Also H. Tsutsui deserves a special thank: among many things, he introduced me to HFSS and our discussions helped me to widen my (still small) knowledge in electromagnetics.

I profit of the collaboration of researchers and students from Università di Roma "La Sapienza" and LNF-INFN. I worked closely with S. De Santis, with whom I walked my first steps in the accelerator physics few years ago. M. Migliorati always supported me, giving many useful suggestions and I shared part of this thesis work with S. Ugoli. B. Spataro helped me as well, both professionally and paying a great attention to my whole life.

I would like also to mention Y. Papaphilippou and N. Catalan, with whom I shared the office for a long period; I always bored them with many small daily problems.

In the very last moments and for many practical details in finishing this thesis, I received the help of G. Rumolo, R. Tomas and S. Redaelli. I acknowledge again F. Ruggiero for carefully reading the manuscript and suggesting many necessary changes.

Eventually I express my deepest thankfulness to my family, who always supported my choices materially and psychologically.

Last but not least, my wife Daniela moved me forward with her being close to me in every (easy or difficult) moment of my life: her love and support has been more than fundamental.